

Mechanisms of nanofractal structure formation and post-growth evolution

Dissertation
zur Erlangung des Doktorgrades
der Naturwissenschaften

vorgelegt beim Fachbereich Physik
der Johann Wolfgang Goethe–Universität
in Frankfurt am Main

von
Veronika V. Dick
aus Székesfehérvár, Ungarn

Frankfurt am Main
2011

(D30)

vom Fachbereich Physik der
Johann Wolfgang Goethe–Universität, Frankfurt am Main, als
Dissertation angenommen.

Dekan: Prof. Dr. Michael Huth

Gutachter: Prof. Dr. Andrey V. Solov'yov

Gutachter: Prof. Dr. Stefan Schramm

Datum der Disputation:

for Notes

Kurzfassung

Die Nanotechnologie ist ein sich rasch entwickelndes Wissenschaftszweig, der sich auf die Untersuchung von Phänomenen auf der Nanometerskala fokussiert, insbesondere in Bezug auf die Möglichkeiten der Materiemanipulation im Nanobereich. Eines der wichtigsten Ziele der Nanotechnologie ist die Entwicklung der kontrollierten, reproduzierbaren und industriell transportierbaren Techniken zur Herstellung von nanostrukturierten Materialien.

Die konventionelle Dünnschichtwachstumstechnik durch die Deposition von Atomen [1, 2], kleinen atomaren Clustern [2, 3] und Molekülen [1, 4, 5] auf Oberflächen ist die allgemeine Methode, die oft in der Nanotechnologie für die Herstellung neuer Materialien verwendet wird. Jüngste Experimente zeigen, dass sich Muster mit unterschiedlicher Morphologie im Verlauf des Nanopartikeldepositionsprozesses auf einer Oberfläche gebildet werden können [2, 3, 6]. Die Voraussage der endgültigen Architektur der wachsenden Materialien ist in diesem Zusammenhang ein grundsätzliches Problem, das einer tieferen Studie wert ist.

Ein weiterer Faktor, der eine wichtige Rolle in der industriellen Anwendung neuer Materialien spielt, ist die Frage nach der Stabilität der resultierenden Strukturen nach dem Depositionswachstum. Das Verständnis der Postwachstumsrelaxationsprozesse würde eine Möglichkeit geben, die Lebensdauer der durch Deposition gewonnener Materialien, abhängig von den Herstellungsbedingungen, abzuschätzen. Steuerbare Postwachstumsmanipulationen der hinterlegten Strukturen eröffnen neue Wege für die Konstruktion von nanostrukturierten Materialien.

Die Aufgabe dieser Arbeit ist es, Mechanismen der Bildung und der Postwachstumsentwicklung von nanostrukturierten Materialien, die durch die Methode der Deposition atomarer Cluster auf einer Oberfläche hergestellt werden, zu verstehen. Um die Aufgabe dieser Arbeit zu bewältigen, werden folgende Hauptprobleme angesprochen:

1. Die Eigenschaften von isolierten Clustern können sich erheblich von denen

- ähnlicher Cluster, die aber auf einer festen Oberfläche auftreten, unterscheiden [2, 3, 7]. Der Unterschied erklärt sich durch die Interaktion zwischen dem Cluster und der Unterlage. Deshalb ist das Verständnis der strukturellen und dynamischen Eigenschaften eines atomaren Cluster auf einer Oberfläche ein Thema von großem Interesse, sowohl aus wissenschaftlicher, als auch aus technologischer Sicht [2, 8]. In dieser Arbeit sind Stabilität, Energie und Geometrie eines atomaren Clusters auf einer festen Oberfläche mit Hilfe eines Flüssigkeitsstropfenansatzes unter der Berücksichtigung der Cluster-Festkörper Wechselwirkungen untersucht worden. Die Geometrie der abgelagerten Cluster wurde mit der Geometrie der isolierten Cluster verglichen, die Unterschiede wurde diskutiert.
2. Die Szenarien der Strukturbildung auf einer Unterlage hängen im Laufe des Depositionsprozesses eines Clusters stark von der Dynamik der zur Deposition stehender Clustern. Deshalb ist das Studium der Dynamik einzelnes Clusters auf der Oberfläche, ein wichtiger Schritt auf dem Weg zur Vorhersage der Strukturmorphologie. Zur Untersuchung der Dynamik wurde in dieser Arbeit der Clusterdiffusionsprozess auf einer Oberfläche mit der klassischen Technik der Molekulardynamik für ein einzelnes Cluster modelliert. Die Diffusionskoeffizienten für Silber-Nanocluster wurden aus der Analyse der Clustertrajektorien erhalten. Es wurde bestimmt, wie die Diffusionskoeffizienten von der Systemtemperatur und der Wechselwirkung zwischen dem Cluster und der Unterlage abhängen. Die Ergebnisse der Simulation sind mit den verfügbaren experimentellen Ergebnissen für die Diffusionskoeffizienten von Silber-Clustern auf Graphit-Oberfläche verglichen.
 3. Die Methoden der klassischen Molekulardynamik können nicht für die Modellierung der Selbstorganisationsprozesse mehrerer atomarer Cluster auf einer Oberfläche verwendet werden, denn diese Prozesse ereignen sich auf einer Zeitskala im Minutenbereich, was eine immense Computerrechenleistung für die Simulation mehrerer Cluster erfordern würde. Um die Dynamik der Selbstorganisation mehrerer Cluster auf einer Oberfläche zu beschreiben, wurde ein probabilistischer Ansatz, der auf dem Monte-Carlo Prinzip basiert, entwickelt. Der Monte-Carlo Ansatz basiert auf den Ergebnissen von Molekulardynamiksimulationen für einen einzelnen Cluster auf einer Oberfläche. Diese Methode ist anwendbar für die freie Nanopartikeldiffusion auf einer Oberfläche, die Ag-

gregation der Nanopartikel zu Inseln und die Verdampfung der Nanopartikel von diesen Inseln. Die entwickelte Methode ist benutzbar für das Studium der Musterbildung von Strukturen bis zu Tausenden nm, sowie für das Studium der Stabilität dieser Strukturen. Die entwickelte Methode wurde implementiert im `MBN Explorer` Softwarepaket.

4. Der Prozess der Strukturbildung auf einer Unterlage wurde untersucht für verschiedene Szenarien. Basierend auf der Analyse der Simulationsergebnisse wurden einige Musterunterscheidungskriterien vorgeschlagen. Diese Kriterien verwendet man zum Unterscheiden zwischen verschiedenen Mustern auf der Oberfläche, zum Beispiel zum Unterscheiden zwischen Fraktalen oder kompakten Inseln. Diese Kriterien lassen sich zur Vorhersage der endgültigen Morphologie der wachsenden Struktur verwenden.
5. Die Postwachstumsevolution der Strukturen auf einer Oberfläche wurde ebenfalls untersucht. Besondere Aufmerksamkeit legt diese Arbeit auf eine systematische theoretische Analyse der Postwachstumsvorgänge der Nanofraktale auf einer Oberfläche. Die zeitliche Entwicklung der fraktalen Morphologie im Zuge der Postwachstumsrelaxation wurde analysiert. Die Ergebnisse dieser Berechnungen wurden mit den experimentellen Daten der Postwachstumsrelaxation von Silber-Clusterfraktalen auf einer Graphitunterlage verglichen.

Alle genannten Probleme sind im Detail in der Arbeit diskutiert.

Abstract

Nanotechnology is a rapidly developing branch of science, which is focused on the study of phenomena at the nanometer scale, in particular related to the possibilities of matter manipulation. One of the main goals of nanotechnology is the development of controlled, reproducible, and industrially transposable nanostructured materials.

The conventional technique of thin-film growth by deposition of atoms [1, 2], small atomic clusters [2, 3] and molecules [1, 4, 5] on surfaces is the general method, which is often used in nanotechnology for production of new materials. Recent experiments show, that patterns with different morphology can be formed in the course of nanoparticles deposition process on a surface [2, 3, 6]. In this context, predicting of the final architecture of the growing materials is a fundamental problem worth studying.

Another factor, which plays an important role in industrial applications of new materials, is the question of post-growth stability of deposited structures. The understanding of the post-growth relaxation processes would give a possibility to estimate the lifetime of the deposited material depending on the conditions at which the material was fabricated. Controllable post-growth manipulations with the architecture of deposited structures opens new path for engineering of nanostructured materials.

The task of this thesis is to advance understanding mechanisms of formation and post-growth evolution of nanostructured materials fabricated by atomic clusters deposition on a surface. In order to achieve this goal the following main problems were addressed:

1. The properties of isolated clusters can significantly differ from those of analogous clusters occurring on a solid surface [2, 3, 7]. The difference is caused by the interaction between the cluster and the solid. Therefore, the understanding of structural and dynamical properties of a an atomic cluster on a surface is a topic of intense interest from the scientific and technological point

- of view [2,8]. In the thesis, stability, energy, and geometry of an atomic cluster on a solid surface were studied using a liquid drop approach which takes into account the cluster-solid interaction. Geometries of the deposited clusters are compared with those of isolated clusters and the differences are discussed.
2. The formation scenarios of patterns on a surface in the course of the process of cluster deposition depends strongly on the dynamics of deposited clusters. Therefore, an important step towards predicting pattern morphology is to study dynamics of a single cluster on a surface. The process of cluster diffusion on a surface was modeled with the use of classical molecular dynamics technique, and the diffusion coefficients for the silver nanoclusters were obtained from the analysis of trajectories of the clusters. The dependence of the diffusion coefficient on the system's temperature and cluster-surface interaction was established. The results of the calculations are compared with the available experimental results for the diffusion coefficient of silver clusters on graphite surface.
 3. The methods of classical molecular dynamics can not be used for modeling the self-assembly processes of atomic clusters on a surface, because these processes occur on the minutes timescale, what would require an unachievable computer resource for the simulation. Based on the results of molecular dynamics simulations for a single cluster on a surface a Monte-Carlo based approach has been developed to describe the dynamics of the self-assembly of nanoparticles on a surface. This method accounts for the free particle diffusion on a surface, aggregation into islands and detachment from these islands. The developed method is allowed to study pattern formation of structures up to thousands nm, as well as the stability of these structures. Developed method was implemented in `MBN Explorer` computer package.
 4. The process of the pattern formation on a surface was modeled for several different scenarios. Based on the analysis of results of simulations was suggested a criterion, which can be used to distinguish between different patterns formed on a surface, for example: between fractals or compact islands. This criteria can be used to predict the final morphology of a growing structure.
 5. The post-growth evolution of patterns on a surface was also analyzed. In particular, attention in the thesis is payed to a systematical theoretical analysis

of the post-growth processes occurring in nanofractals on a surface. The time evolution of fractal morphology in the course of the post-growth relaxation was analyzed, the results of these calculations were compared with experimental data available for the post-growth relaxation of silver cluster fractals on graphite substrate.

All the aforementioned problems are discussed in details in the thesis.

Zusammenfassung

Die Herstellung neuer Nanomaterialien ist ein wichtiger Zweig auf dem Entwicklungsgebiet der Nanowissenschaften [2, 4, 8]. Die Größenreduzierung eröffnet den Zugang zur einer ganzen Reihe von neuen physikalischen und chemischen Eigenschaften und einer Fülle von möglichen Einsatzmöglichkeiten. Der Zugang zu diesen neuen Möglichkeiten erfordert die Entwicklung geeigneter Methoden für die Herstellung von Nanomaterialien. Die Bildung von nanostrukturierten Materialien wird vor allem durch Selbstorganisationsprozesse geregelt. Das Streben nach Verständnis der Selbstorganisationsmechanismen im Nanometerbereich ist eine der grundlegenden Motivationen in der Nanotechnologie.

Für den industriellen Einsatz von Nanomaterialien ist es sehr wichtig, eine Technologie mit der Möglichkeit der Kontrolle der resultierenden Architektur des Materials noch im Laufe des Wachstumsprozesses zu schaffen. Der andere wichtige Aspekt ist die Stabilität der neuen Materialien. Die Lebensdauer des neuen Materials spielt eine entscheidende Rolle für die potenzielle Nutzbarkeit dieses Materials. In diesem Zusammenhang ist es sehr wichtig, die Mechanismen der Bildung und der Postwachstumevolution von nanostrukturierten Materialien zu verstehen.

Es wurden verschiedene Techniken entwickelt, um die Nanomaterialien zu bauen [2, 4, 8]: Deposition der Atome und atomarer Cluster [2, 3, 6, 9, 10], mechanische Mahlung [8, 11], chemische Methoden [2, 12], Gas-Aggregationstechniken [4, 8] und so weiter.

Die Aufgabe dieser Arbeit ist es, die Mechanismen der Bildung und die Postwachstumsevolution von nanostrukturierten Materialien, die durch atomare Clusterdeposition auf einer Oberfläche hergestellt wurden, zu verstehen.

Atomare Clusterdeposition auf einer Oberfläche ist eine Methode, die in der Nanotechnologie für die Herstellung neuer Materialien oft verwendet wird. Jüngste Experimente zeigen, dass Muster mit unterschiedlicher Morphologie im Laufe der Clusterdeposition auf einer Oberfläche gebildet werden können [2, 3, 6]. Unter allen möglichen Formen wurden auch tropfenförmige Gebilde und fraktale Inseln in verschiedenen Systemen beobachtet [2, 3, 6]. Es konnte gezeigt werden, dass die In-

sel Morphologie von verschiedenen Faktoren, wie der Temperatur [2, 3, 9, 10, 13], der Nanopartikelgröße [14], der Partikeldepositionsrate [13, 15, 16], der Unterlagenrauigkeit [17, 18], der Konzentration der Verunreinigungen im System [2, 9, 19] und den interpartikulären Wechselwirkungsenergien [2, 13] abhängt. Obwohl es viele Beispiele für Selbstorganisation in den Nanosystemen gibt, werden doch oft die Mechanismen und die treibenden Kräfte dieser Verfahren nicht gut verstanden [2, 8, 20, 21]. Häufig führen kleine Änderungen in der Struktur oder an der Zusammensetzung der konstituierenden Nanopartikel oder des Substrats zu einer dramatischen Veränderung der Eigenschaften des gesamten Systems, das im Zuge der Selbstorganisationsprozesse erstellt wird.

In diesem Zusammenhang ist die Voraussage der endgültigen Architektur der wachsenden Materialien eines der grundlegenden Probleme. Sobald die Mechanismen des Wachstums und der Selbstorganisation vollständig verstanden sind, können die Wachstumsprozesse genau gesteuert werden, wodurch eine breite Palette von Nanostrukturen auf Oberflächen und neuartige Materialien mit maßgeschneiderten Eigenschaften erstellt werden können [20–23]. Diese Kenntnisse sollten eine enorme Bedeutung in den praktischen und industriellen Anwendungen haben. Die Kenntnisse sind letztlich maßgeblich für die effiziente Entwicklung und die kostengünstige Herstellung von den neuartigen funktionellen nanostrukturierten Oberflächen und Beschichtungen mit maßgeschneiderten chemischen, elektromagnetischen, optischen und mechanischen Eigenschaften. Diese neuartigen Nanomaterialien können als Komponenten (und/oder ganze Systeme) in kleinen elektronischen Geräten (Mikrochips, Informationsspeichergeräte, Laser) [2, 24, 25], fortschrittlichen chemischen (Katalysatoren, Sensoren), medizinischen (biokompatible Beschichtungen) [26, 27] und technischen (neue Beschichtungen und Materialien) [2, 12] Anwendungen verwendet werden.

Um ein Studium einer Menge von Clustern auf einer Unterlage betreiben zu können, wurde in vorliegender Arbeit ein Schritt-für-Schritt-Ansatz verwendet. Gestartet wird mit der theoretischen Analyse des Verhaltens eines einzelnen atomaren Cluster auf einer Unterlage. Eigenschaften eines atomaren Cluster auf einer Unterlage können wesentlich von den Eigenschaften eines isolierten Clusters abweichen [2, 3, 7]. Der Unterschied erklärt sich durch die Interaktion zwischen dem Cluster und der Unterlage. In dieser Arbeit wurden die Stabilität, die Energie und die Geometrie eines atomaren Clusters auf einer festen Oberfläche mit der auf dem Tropfenmodell basierenden Methode studiert. Das Tropfenmodell beachtet die In-

teraktion zwischen dem Cluster und der festen Unterlage und berücksichtigt die Korrekturen im Zusammenhang mit der Deformation des Clusters an der festen Unterlage. Die Berechnungsergebnisse, die mit dem Tropfenmodell erhalten wurden, zeigen, dass die Clusterdeformation, verursacht durch die Interaktion zwischen dem Cluster und der Unterlage, einen bestimmenden Faktor für die Form und Stabilität eines Clusters auf der Unterlage darstellt. Das Tropfenmodell kann als eine Vorhersagemethodik für die Beschreibung der Form und der Energetik eines Clusters auf einer Unterlage verwendet werden.

Die Mobilität eines einzelnen Nanopartikels spielt eine wichtige Rolle in der Dynamik einer Partikelansammlung auf einer Unterlage. In dieser Arbeit wurde die Clusterdiffusion auf einer Unterlage mit den Methoden der klassischen Molekulardynamik modelliert. Einfluss der verschiedenen wesentlichen Diffusionsparameter eines Clusters auf einer Unterlage wurden für ein konkretes System untersucht (Silbernanopartikel auf einer Graphitoberfläche). Insbesondere solche Parameter, wie die Clustergröße, die Bindungsenergie zwischen Silber- und Kohlenstoffatomen und die Temperatur wurden betrachtet.

Die Ergebnisse der molekulardynamischen Simulationen für Silbercluster auf einer Graphitoberfläche zeigen, dass die Cluster als Ganzes über die Unterlage mit einer hohen Diffusivität diffundieren. Dieses Simulationsergebnis steht in einer guten Übereinstimmung mit den experimentellen Beobachtungsergebnissen, die in der Gruppe von Prof. C. Bréchnac gewonnen wurden [9, 10, 17]. Basierend auf diesen Fakten und auf dem kinetischen Monte-Carlo-Ansatz wurde eine Methode zur Beschreibung des Verhaltens von Partikelgruppen auf einer Unterlage entwickelt. Diese Methode berücksichtigt die freie Partikeldiffusion auf einer Oberfläche, die Aggregation zu Inseln und die Partikelverdampfung von diesen Inseln.

Die Grundidee des Verfahrens ist nachfolgend beschrieben. Dafür betrachten wir ein molekulares System, gebildet aus einer gewissen Anzahl von Nanopartikeln. Zu jedem Partikel im System wird zunächst eine Anzahl der möglichen Diffusionsrichtungen vorgegeben. Dabei kann ein Partikel entweder frei oder entlang der Peripherie der bereits vorgeformten Struktur, wie in Fig. 1 abgebildet, diffundieren. Eine Diffusionsrichtung für ein Partikel wird nach dem Zufallsprinzip in einer solchen Weise gewählt, dass alle möglichen Diffusionsrichtungen gleichwahrscheinlich sind. Alle Diffusionsprozesse im System treten mit bestimmten kinetischen Raten (Wahrscheinlichkeiten) auf. Die Raten stellen die Modelleingaben dar. Die kinetischen Raten sind materialabhängige Parameter, die von der atomaren Komposition der

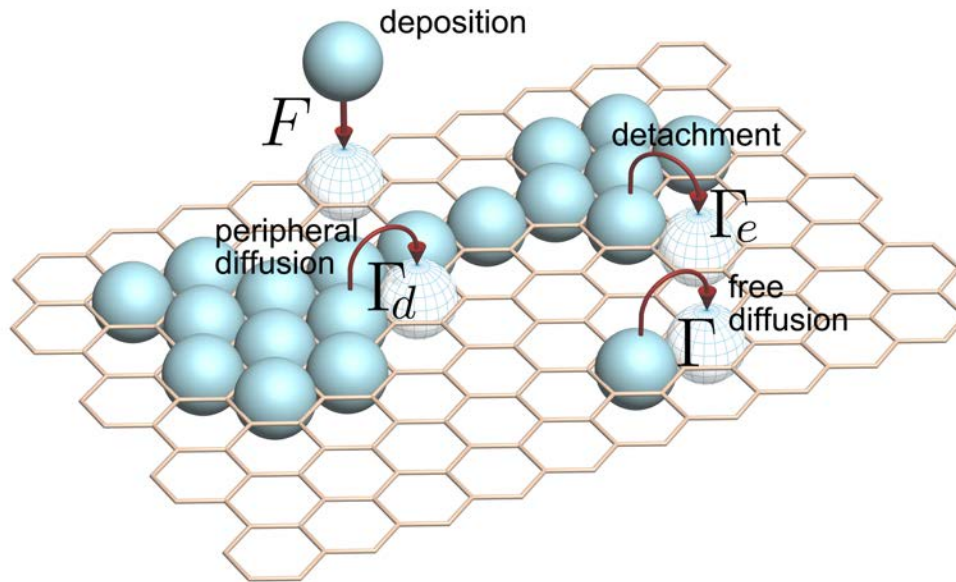


Figure 1: Anordnung der deponierten Nanopartikel auf einer Oberfläche. Die wichtigsten Prozesse, die Musterbildung auf einer Oberfläche bestimmen, sind durch Pfeile angedeutet: F ist die Partikeldepositionsrate, Γ ist die Diffusionsrate eines freien Nanopartikels, Γ_d ist die Diffusionsrate eines Nanopartikels entlang der Peripherie einer Insel, und Γ_e ist die Verdampfungsrates eines Nanopartikels von der Insel.

Nanopartikel, dem Substratmaterial und den interpartikulären Wechselwirkungen bestimmt werden. Die Modellparameter können theoretisch für jeden Einzelfall auf der Grundlage des atomistischen Ansatzes berechnet oder einem Experiment entnommen werden. Die Wahl der Parameterwerte ist in dieser Arbeit für ein konkretes System, Silbercluster auf einer Graphitoberfläche, diskutiert.

In dieser Arbeit ist nachgewiesen, dass unterschiedliche kinetische Prozesse im Laufe der Nanostrukturbildung und Postwachstumsfragmentierung die Form der Inseln auf einer Oberfläche bestimmen. Die Ergebnisse der Anwendung des kinetischen Modells, das zum Studium der Bildung und Fragmentierung von Fraktalen auf einer Oberfläche durch Partikeldisposition verwendet wurde, werden ausführlich in Kapitel 5 diskutiert.

Der Prozess der Musterbildung auf einer Oberfläche wurde für verschiedene Szenarien simuliert. Basierend auf der Ergebnisanalyse der Simulationen wurden Musterunterscheidungskriterien vorgeschlagen. Diese Kriterien werden verwendet, um zwischen verschiedenen Mustern auf einer Oberfläche unterscheiden zu können,

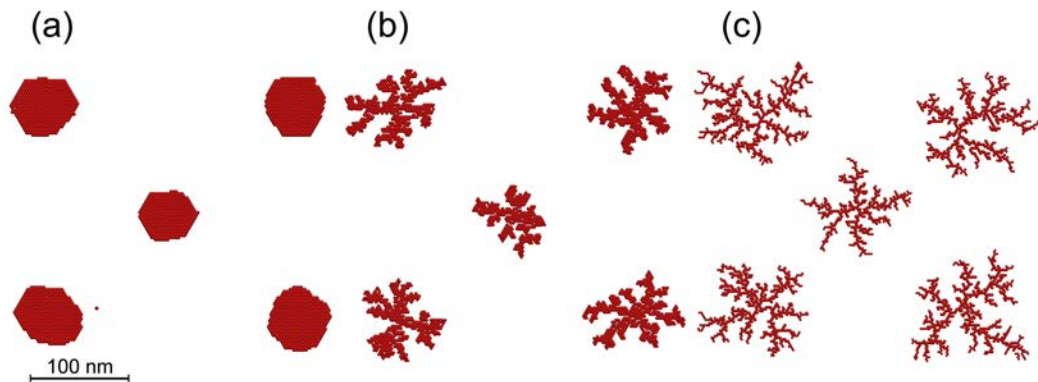


Figure 2: *Morphologie verschiedener Muster, beobachtet nach der Selbstorganisation der Nanopartikel auf einer Oberfläche (a) Kompakte Nanoinseln werden gebildet, wenn die Umlagerungszeit der Partikel kleiner ist als die Keimbildungszeit, (b) Nanofraktale mit dicken Ästen werden gebildet, wenn einige periphere Partikel genügend Zeit zur Neuordnung haben, es wird eine kompaktere Struktur gebildet, (c) Nanofraktale mit dünnen Ästen werden gebildet, wenn die innere Dynamik von Partikeln im Fraktal fast eingefroren ist.*

zum Beispiel zwischen Nanofraktalen oder kompakten Nanoinseln. In dieser Arbeit wird gezeigt, dass die Morphologie der Inseln auf einer Oberfläche hauptsächlich durch die Nukleations- und die Umlagerungszeit bestimmt wird. Die Nukleationszeit (Keimbildungszeit) ist die charakteristische Zeit bis ein neu ausgesetztes Partikel die Wachstumsregion erreicht. Die Umlagerungszeit ist die charakteristische Zeit bis ein neues Partikel eine optimale Position innerhalb einer Insel findet. In Fig. 2 sind als Beispiel unterschiedliche Strukturen, die durch die Variation der Beziehungen zwischen der Keimbildungs- und der Umlagerungszeiten gebildet werden können, dargestellt.

Diese Dissertation präsentiert eine systematische theoretische Analyse der Postwachstumsprozesse in Nanofraktalen auf einer Oberfläche. Die Simulationen haben gezeigt, dass die Form und die Anzahl der Inseln, die auf einer Oberfläche im Laufe der Postwachstumsrelaxation geschaffen werden, von der Partikeldiffusionsrate entlang der fraktalen Peripherie und einer Partikelverdampfungsrate abhängen. In dieser Arbeit werden die Analyse der fraktalen Dynamik auf einer Oberfläche und die wichtigsten Szenarien der Fragmentierung des Systems vorgestellt. Die Simulationen der fraktalen Dynamik wurden mit einer weiten Variation des Wertebereichs der Modellparameterwerte durchgeführt. Die Vorhersagen der entwickelten Methode wurden mit den experimentell beobachteten Ergebnissen der Fragmentierung

von Silbernanofraktalen auf einer Graphitoberfläche verglichen. Das vorgeschlagene Modell ist in der Lage die experimentelle Inselgrößenstreuungen, die für verschiedene Szenarien der fraktalen Fragmentierung berechnet wurden, zu reproduzieren. Die gute Übereinstimmung der Ergebnisse der Berechnungen, die unter der Verwendung des entwickelten Verfahrens durchgeführt wurden, mit den Ergebnissen von experimentellen Messungen zeigt, dass dieses Verfahren für die Modellierung und Analyse der Dynamik der nanostrukturierten Materialien auf einer Oberfläche eingesetzt werden kann.

Zusammenfassend stellt die vorliegende Arbeit den theoretischen Ansatz vor, mit dem man das Verhalten einer Partikelansammlung auf einer Oberfläche beschreiben kann. Der präsentierter Formalismus ist allgemein und bietet die Möglichkeit der zukünftigen Anwendung in einer Vielzahl von Systemen und Prozessen. Zum Beispiel kann dieses Verfahren für die Untersuchung der Eiskristallbildung im Weltraum eingesetzt werden. Die Vorhersage der Existenz einer spezifischen Objektform im Raum ist eine der grundlegenden Aufgaben der Physik.

Contents

1	Introduction	1
1.1	Nanomaterials: synthesis and application	1
1.2	Self-organization of nanostructured materials	2
1.3	Thesis overview	5
2	Theoretical Methods	7
2.1	Methods of molecular dynamics	8
2.1.1	Born-Oppenheimer approximation	8
2.1.2	Formalism of classical molecular dynamics	10
2.1.3	Energy and temperature control of a system in molecular dynamics simulation	12
2.2	Interatomic potentials: pairwise potentials	15
2.2.1	Lennard-Jones potential	15
2.2.2	Morse potential	16
2.3	Interatomic potentials: many-body potentials	17
2.3.1	Sutton-Chen potential	18
2.3.2	Brenner potential	19
2.4	Kinetic Monte - Carlo method	23
2.4.1	The motivation to use kMC	23
2.4.2	Formalism of kinetic Monte Carlo method	25
3	Cluster on a surface	29
3.1	Liquid drop model of a cluster on a surface	30
3.1.1	Droplet model of a free cluster	31
3.1.2	Droplet model of an atomic cluster on a solid surface	34
3.1.3	Liquid drop model for a silver cluster on a graphite surface	48
3.2	Cluster diffusion over a surface	53

3.2.1	Diffusion coefficient	53
3.2.2	Silver cluster diffusion over graphite surface: simulations versus experiment	56
4	Kinetic model for an assembly of nanoparticles on a surface	65
4.1	Basic principles and assumptions of the kinetic model	66
4.2	Algorithm for the implementation of the kinetic model	70
4.3	Parameters of the kinetic model	72
5	Formation and fragmentation of nanofractals by nanoparticles deposited on a surface	75
5.1	Formation of a nanofractal by nanoparticles deposited on a surface	76
5.1.1	Simulation of a nanofractal growth	77
5.1.2	Criteria for nanoscale surface pattern formation	78
5.2	Different paths of nanofractal fragmentation	82
5.3	Fragmentation of silver cluster nanofractals: theory predictions versus experimental observations	97
6	Summary and conclusions	101
A	Parameters of the interatomic interactions	105
A.1	Pairwise potentials	105
A.2	Many-body potentials	106
B	Implementation of the kinetic model in MBN Explorer	109
B.1	Modeling of nanoparticle diffusion processes on a cubic lattice	111
B.2	Modeling of nanoparticle diffusion processes on a hexagonal lattice	114
B.3	Modeling of nanoparticle diffusion processes on a surface	117
B.4	Computation tests for the nanoparticle diffusion processes	120
	Bibliography	131
	Biography (Lebenslauf)	141

Chapter 1

Introduction

Construction of new nanomaterials is an important branch in the developing field of nanoscience [2, 4, 8]. Size reduction opens to a whole range of new physical and chemical properties and an abundance of potential applications. Access to these new possibilities requires the developing of suitable methods for the fabrication of nanomaterials. Formation of nanostructured materials is often governed by self-organization processes. Therefore, the quest to understand mechanisms of self-organization is one of the fundamental motivations in the nanotechnology.

For the industrial application of nanomaterials is very important to create a technology, which will give a possibility to control the architecture of the material in the course of the growing process. The other important aspect is the stability of new materials. The life-time of a nanomaterial is the decisive factor, which is specified its practicability. In this context, it is very important to understand mechanisms of formation and post-growth evolution of nanostructured materials.

1.1 Nanomaterials: synthesis and application

Fabrication of new nanomaterials with the predefined unique properties is most active research direction of the nanotechnology [2, 4, 8]. Different techniques were developed to build up the nanomaterials [2, 4, 8]: atoms, molecules and atomic clusters deposition [2, 3, 6, 9, 10], mechanical milling [8, 11], chemical methods [2, 12], gas-aggregation techniques [4, 8] and so on.

In the thesis, there was done a step towards the understanding of the mechanisms of formation and post-growth evolution of nanostructured materials fabricated by atomic clusters deposition on a surface.

Atomic clusters deposition on a surface is the method, which is often used in nanotechnology for production of new materials. This method allows to construct materials with predefined properties [1, 2, 4, 12]. Recent experiments show that patterns with different morphology can be formed in the course of clusters deposition process on a surface [2, 3, 6]. Among other possible shapes, droplet-like and fractal islands have been observed in various systems [2, 3, 6]. It was shown that the island morphology depends on various factors, such as the temperature [2, 3, 9, 10, 13], particle size [14], particle deposition rate [13, 15, 16], substrate roughness [17, 18], concentration of impurities in the system [2, 9, 19] and interparticle interaction energies [2, 13]. It was also demonstrated that the patterns on a surface strongly depend on the type of the substrate (see Fig. 1.1a-b). For example, experimental studies of silver clusters deposited on silicon at room temperature showed that droplet-like islands are formed [28], while in [9, 10, 19] it was demonstrated that dendritic shapes emerge on graphite. Although, there are many examples of self-organization in nanoscale systems, often the mechanisms and driving forces of these processes are not well understood [2, 8, 20, 21]. Frequently a small change in the structure or composition of constituent nanoparticles or in the substrate results in a dramatic change in the properties of the entire system created in the course of the self-organization processes. In this context, predicting of the final architecture of the growing materials is one of the fundamental problems.

Once the mechanisms of growth and self-organization are fully understood, the growth processes can be precisely controlled, allowing to create a wide range of surface nanostructures and novel materials with tailored properties [20–23]. Such knowledge should have tremendous practical and industrial applications. It is ultimately required for the efficient development and low-cost production of novel functional nanostructured surfaces and coatings with tailored chemical, electromagnetic, optical and mechanical properties which can be utilized as components (and/or entire systems) in small electronic devices (microchips, information storage devices, lasers) [2, 24, 25], advanced chemical (catalysts, sensors), medical (biocompatible coatings) [26, 27] and engineering (new coatings and materials) [2, 12] applications.

1.2 Self-organization of nanostructured materials

Self-organization processes are common processes in nature, many systems in nature show organization e.g. galaxies, planets, compounds, cells, organisms, societies,

particles on a surfaces and so on. The essence of self-organization is that system structure (at least in part) appears without explicit pressure or constraints from outside the system. The organization can evolve either in time or space, can maintain a stable form or can show transient phenomena.

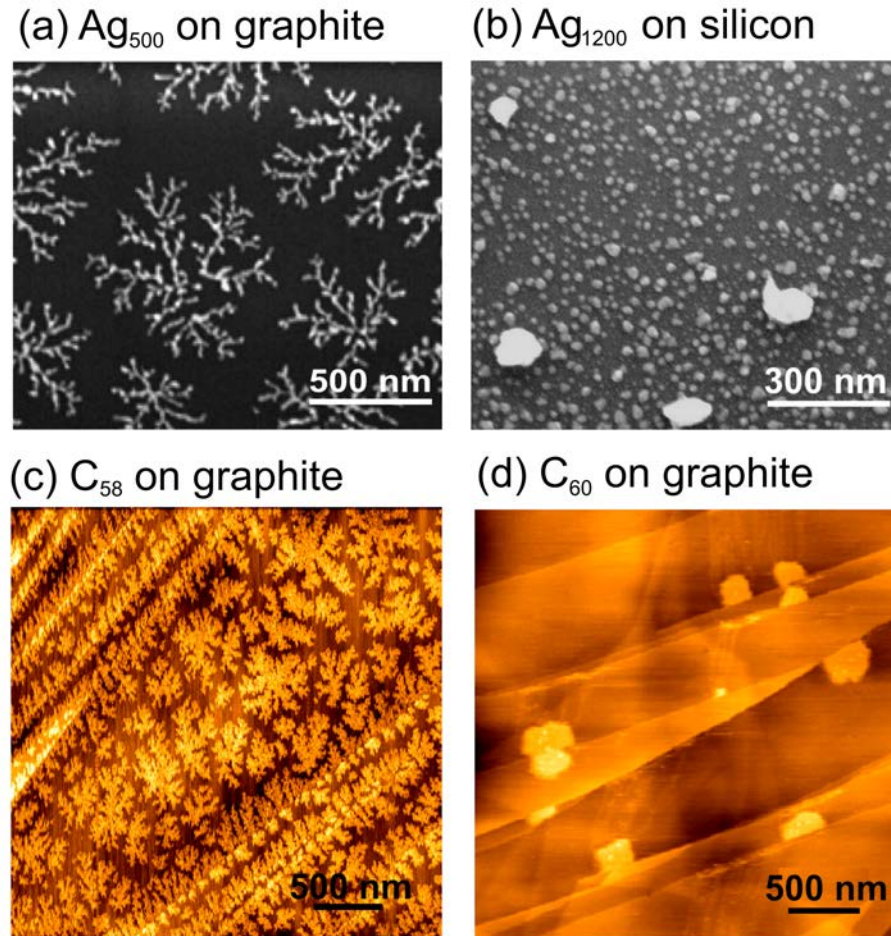


Figure 1.1: Examples of self-organization in nanoscale systems. Scanning electron microscopy (SEM) images show the morphologies of silver thin films growing by silver cluster deposition on a surface: (a) fractals formed on a graphite surface [9] (b) compact islands formed on a silicon substrate [28]; Atomic force microscopy (AFM) images show the morphologies of (c) C₅₈ – and (d) C₆₀ – films on a highly ordered pyrolytic graphite surface [29].

Many examples of self-organization in nanoscale systems are observed, some of these are shown in Fig. 1.1. Formation of the dendritic structures (fractals) in course of thin films growth is one common example of self-organization in nanoscale (see Fig. 1.1).

The investigation of the dendritic structures (fractals) has attracted considerable attention [6, 9, 10, 19, 30–34]. The formation of such systems provides a natural framework for studying disordered structures on a surface because fractals are generally observed in far-from-equilibrium growth regime. During the last years fractal shape have been observed for a variety of systems. For example, fractals consisting of Ag (see Fig. 1.1a) [9, 10, 19], Au [35], Fe-N [33] clusters and C_{58} , C_{60} molecules (see Fig. 1.1c-d) [29, 36, 37] have been fabricated on different surfaces with the use of the cluster deposition technique [1, 4].

The processes of self-organization dramatically influence on the scenarios of the post-growth relaxation of a nanopattern on a surface. The post-growth transformation of silver cluster fractals to compact droplets on graphite surface was experimentally studied in [9, 10, 19]. It was demonstrated that depending on the experimental conditions the shape and the size of the stable silver droplets changes significantly [19]. In [9, 10, 19] it was shown that oxidizing of silver clusters results in rapid fragmentation of a fractal, leading to the formation of several compact droplets. An important characteristic, which determines fractal formation and post-growth relaxation dynamics, is the mobility of a cluster on the substrate, which in turn is temperature dependent. Fractals of gold clusters, grown at room temperature on ruthenium substrate undergo a transformation into compact droplets after annealing at 650 K [38]. Thermal relaxation of silver cluster fractals was experimentally studied in [9, 19].

The understanding of the post-growth relaxation processes would allow to control the self-organization processes of particles on a surface for the purpose of obtaining patterns with predictable properties. An illustrative example of post-growth pattern manipulation was given in [39]. In that work, morphologies of preformed C_{60} thin films were changed by adding metal impurity into the system. Thin films with triangular and dendritic single-crystal grains were detected by changing the thickness of the pristine fullerene film and the concentration of Ag impurities.

The self-organization of nanoparticles plays an important role in the processes of the formation and post-growth evolution of the nanostructures on a surface [2, 7, 13]. The understanding of the mechanisms of self-organization on the nanoscale is very important because this may provide essential tool for the control and manipulation of nanoparticle's dynamics on a surface which will allow efficient obtaining of the desirable patterns of deposited material.

1.3 Thesis overview

The thesis is organized as follows.

In Chapter 2, the computational methodology used for modeling of a single cluster structure and dynamics on a surface is described. Specifically, the molecular dynamics methods, and the empirical potentials used in modeling of interparticle's interactions are discussed. The methods of classical molecular dynamics can not be used for modeling the self-assembly processes of atomic clusters on a surface, because these processes occur on the minutes timescale, what would require an unachievable computer resource for the simulation. Kinetic Monte Carlo attempts to overcome this limitation of molecular dynamics approach by exploiting the fact that the long-time dynamics of this kind of system typically consist of diffusive jumps from state to state. In section 2.4 the basic idea of kinetic Monte Carlo method is discussed.

In Chapter 3, the results of modeling of structure and dynamics of a single nanoparticle on a surface are discussed. In section 3.1, stability, energy, and geometry of an atomic cluster on a solid surface are studied using a liquid drop approach which takes into account the cluster-solid interaction. In section 3.2, the process of cluster diffusion on a surface is modeled with the use of classical molecular dynamics technique, and the diffusion coefficients for the silver nanoclusters are obtained from the analysis of trajectories of the clusters. The results of the calculations are compared with the available experimental results for the diffusion coefficient of silver clusters on graphite surface.

In Chapter 4, the model, which was developed to describe the dynamics of an assembly of particles on a surface, is discussed. This method describes the dynamics of particles deposited on a surface, which accounts for the particle diffusion on a surface, agglomeration into islands and detachment from these islands. One of the possible implementations of the developed model, which is based on the modified version of the conventional kinetic Monte Carlo method, is shown in subsection 4.2.

In Chapter 5, the results of modeling of the pattern formation and post-growth relaxation on a surface are presented. Process of the pattern formation on a surface are studied for several different scenarios. Based on the analysis of the simulation results is suggested a criterion, which can be used to distinguish between different patterns on a surface in course of the pattern formation (see section 5.1). The systematical theoretical analysis of the post-growth processes occurring in nanofractals on a surface is presented in sec. 5.2. The time evolution of fractal morphology in the

course of the post-growth relaxation is analyzed, the results of these calculations are compared with experimental data available for the post-growth relaxation of silver cluster fractals on graphite substrate.

The thesis is summarized in chapter 6.

The present thesis is based on the original results, published in international journals (see a list of publication) and presented on international conferences (see list of conference proceedings).

Chapter 2

Theoretical Methods

The task of this thesis is to understand mechanisms of formation and post-growth evolution of nanostructured materials fabricated by atomic clusters deposition on a surface. Specifics in the behavior of a single cluster on a surface can strongly influence pattern morphology, which is formed in course of clusters deposition. Therefore, the studying of structural and dynamical properties of an atomic cluster on a surface is the first important step to the achievement the main goal of the work. In this work, the method of classical molecular dynamics (MD) has been used for studying the structures and dynamics of an atomic clusters on a surface.

The method of classical molecular dynamics calculates the time dependent behavior of a molecular system. In section 2.1, the foundations of molecular dynamics are presented. This is followed by a discussion of the empirical potentials used in this work, namely the pair potentials, in section 2.2; and many - body potentials, in section 2.3.

The efficiency of the molecular dynamics depends on large number of factors, such as a computer performance, effective implementation of optimal algorithms and so on. The molecular dynamics simulation is computationally expensive when considering problems where there are a large number of atoms, or when one requires long simulations. The methods of classical molecular dynamics can not be used for modeling the self-assembly process of atomic clusters on a surface, because these processes occur on the minutes timescale, what would require an unachievable computer resource for the simulation. Kinetic Monte Carlo attempts to overcome this limitation of molecular dynamics approach by exploiting the fact that the long-time dynamics of this kind of system typically consist of diffusive jumps from state to state. In section 2.4 the motivation to use and basic idea of the kinetic Monte Carlo

method are discussed.

2.1 Methods of molecular dynamics

Molecular dynamics (MD) is the simultaneous motion of a number of atomic nuclei and electrons forming a molecular system. Complete description of such a system requires solving the full time-dependent Schrödinger equation including both electronic and nuclear degrees of freedom [40]. However, is a formidable computational task which is in fact altogether unfeasible for systems consisting of more than three atoms and more than one electronic state. In order to study the dynamics of the molecular systems several approximations have been imposed.

Firstly, it is assumed in MD that the motions of slow and fast degrees of freedom are separable (adiabatic or Born-Oppenheimer approximation). In the molecular context this means that the electron cloud adjusts instantly to changes in the nuclear configuration. As a consequence, nuclear motion evolves on a single potential energy surface (PES), associated with a single electronic quantum state, which is obtained by solving the time-independent Schrödinger equation for a series of fixed nuclear geometries. In practice, most MD simulations are performed on a ground state PES.

Moreover, in addition to making the Born-Oppenheimer approximation, MD treats the atomic nuclei as classical particles whose trajectories are computed by integrating Newtons equations of motion.

MD has been applied with great success to study a wide range of systems from biomolecules to condensed phases. Its underlying approximations, on the other hand break down in many important physical situations and extensions of the method are needed for those scenarios. An accurate description of hydrogen motion, for instance, requires quantum mechanical treatment. Processes such as charge-transfer reactions and photochemistry are inherently nonadiabatic, i.e., they involve (avoided) crossings of different electronic states rendering the Born-Oppenheimer approximation invalid.

2.1.1 Born-Oppenheimer approximation

For exact description of the electronic and ionic structure of a multi atomic system one has to solve the Schrödinger equation for all particles in the system.

The Schrödinger equation describes the wavefunction of the system (see e.g. [40]):

$$\hat{H}\Psi(\vec{r}_{el}, \vec{r}, t) = i\frac{\partial\Psi(\vec{r}_{el}, \vec{r}, t)}{\partial t}, \quad (2.1)$$

where \hat{H} is the Hamilton operator, $\Psi(\vec{r}_{el}, \vec{r}, t)$ is the wavefunction of the system, which depends on the coordinates of the electrons \vec{r}_{el} and the nuclei \vec{r} within the system, and time t . In this section the atomic system of units is used, $\hbar = m_e = |e| = 1$ unless other units are not indicated.

The Hamiltonian is a sum of kinetic, \hat{T} , and potential, \hat{V} , energy terms:

$$\hat{H} = \hat{T} + \hat{V}. \quad (2.2)$$

If \hat{V} is not a function of time, the Schrödinger equation can be simplified using the mathematical technique known as separation of variables. The wavefunction can be presented as the product of a spatial function and a time function

$$\Psi(\vec{r}_{el}, \vec{r}, t) = \psi(\vec{r}_{el}, \vec{r})\tau(t). \quad (2.3)$$

Substituting these new functions into equation (2.1), two equations is obtained, one of which depends on the position of the particle independent of time and the other of which is a function of time alone. The time-independent Schrödinger equation reads as

$$\hat{H}\Psi(\vec{r}_{el}, \vec{r}) = E\Psi(\vec{r}_{el}, \vec{r}), \quad (2.4)$$

where E is the energy of the system.

If the nuclei move slowly with respect to the electrons, then it is possible to simplify the general molecular problem by separating nuclear and electronic motions. This approximation is reasonable since the mass of a typical nucleus is thousands of times greater than that of an electron and the electrons react essentially instantaneously to changes in nuclear position. Thus, the electron distribution within a molecular system depends on the position of the nuclei, and not their velocities.

This approximation is called the Born-Oppenheimer approximation. The full Hamiltonian for the molecular system can be written as

$$\hat{H} = \hat{T}^{elec}(\vec{r}_{el}) + \hat{T}^{nucl}(\vec{r}) + \hat{V}^{nucl-elec}(\vec{r}, \vec{r}_{el}) + \hat{V}^{elec}(\vec{r}_{el}) + \hat{V}^{nucl}(\vec{r}), \quad (2.5)$$

where $\hat{T}^{elec}(\vec{r}_{el})$ is the electron kinetic energy, $\hat{T}^{nucl}(\vec{r})$ is the nucleon kinetic energy, $\hat{V}^{nucl-elect}(\vec{r}, \vec{r}_{el})$ is the nucleon-electron interaction, $\hat{V}^{elec}(\vec{r}_{el})$ describes the electron-electron interaction and $\hat{V}^{nucl}(\vec{e})$ is the nucleon-nucleon interaction. The Born-Oppenheimer approximation allows to separate the electronic and ionic subsystems, and constructs an electronic Hamiltonian which neglects the kinetic energy term for the nuclei (see e.g. [40]). This Hamiltonian describes the motion of electrons in the field of fixed nuclei

$$\hat{H}^{elec}\psi^{elec}(\vec{r}_{el}, \vec{r}) = E^{eff}(\vec{r})\psi^{elec}(\vec{r}_{el}, \vec{r}) \quad (2.6)$$

The solution of equation (2.6) for the electronic wavefunction produces the effective nuclear potential function E^{eff} . It depends on the nuclear coordinates and describes the potential energy surface for the system.

Accordingly, E^{eff} is also used as the effective potential for the nuclear Hamiltonian:

$$\hat{H}^{nucl} = \hat{T}^{nucl}(\vec{r}) + E^{eff}(\vec{r}) \quad (2.7)$$

This Hamiltonian is used in the Schrödinger equation for nuclear motion, describing the vibrational, rotational, and translational states of the ionic subsystem. In principle, Eq. 2.6 could be solved for $E_{eff}(\vec{r})$, and then Eq. 2.7 could be solved for the nuclear motion. But solution of Eq. 2.6 requires a large amount of computation, usually an empirical fit to $E^{eff}(\vec{r})$, which is called force field, is used. When the quantum mechanical effects are insignificant equation 2.7 can be replaced with the Newton's equation of motion

$$-\frac{dE_{eff}(\vec{r})}{d\vec{r}_i} = m_i \frac{d^2\vec{r}_i}{dt^2} \quad (2.8)$$

2.1.2 Formalism of classical molecular dynamics

The Newtonian equations describe the motion of atoms. In this case each atom has three degrees of freedom which are controlled through three equations of motion. In the following let us consider a molecular system, which consist of N atoms. The Newton's second law of motion can be written for each atom with three degrees of freedom. Consider an arbitrary atom with the index i . The equation of motion for this atom reads as:

$$m_i \vec{a}_i = m_i \frac{d^2 \vec{r}_i}{dt^2} = \vec{F}_i, \quad \text{for all } i = 1 \dots N. \quad (2.9)$$

Here m_i is the mass of an atom, \vec{a}_i is its acceleration and \vec{F}_i is the force that acts on the i -th atom in the system from the site of all other atoms in the system.

The forces \vec{F}_i are determined by the interatomic potentials. These forces may be pairwise, or many-body in nature. The interatomic potentials (and thereby the forces) used in this work are extensively discussed in sections 2.2 and 2.3. Equation (2.9) can be written for each particle and is the second-order differential equation. To solve it numerically one needs to provide the initial conditions, i.e. the information about the system at the beginning of the simulation. The necessary initial conditions are the positions of particles at $t = 0$ and their initial velocities.

Verlet integration

The Verlet integration was implemented in **MBN Explore** computer package, which was used for the simulations performed in the presented work. Verlet integration is a numerical method often used to integrate Newton equation of atom's motion. It is used to calculate trajectories of particles in molecular dynamics simulations. The Verlet integrator offers greater stability than the much simpler Euler method, as well as other properties that are important in physical systems such as time-reversibility and area preserving properties. The method was used by Carl Størmer to compute the trajectories of particles moving in a magnetic field (hence it is also called Størmer's method) and was popularized in molecular dynamics by French physicist Loup Verlet in 1967 [41, 42].

Let us consider the motion of an atom in the system and write out the steps of the numerical velocity Verlet algorithms. As described in the previous section, the motion of an atom with three degrees of freedom is described through Eq. (2.9). Let $\vec{r}_i(t)$, $\vec{v}_i(t)$, $\vec{a}_i(t)$ be the coordinates, velocity components and acceleration components of the i -th particle at time t . The standard implementation scheme of the velocity Verlet algorithm is:

1. Calculate velocities of atoms at the middle of the time step

$$\vec{v}_i \left(t + \frac{\Delta t}{2} \right) = \vec{v}_i(t) + \vec{a}_i(t) \frac{\Delta t}{2}. \quad (2.10)$$

2. Calculate new positions of the atoms

$$\begin{aligned}\vec{r}_i(t + \Delta t) &= \vec{r}_i(t) + \vec{v}_i\left(t + \frac{\Delta t}{2}\right) \Delta t = \\ &= \vec{r}_i(t) + \vec{v}_i(t) \Delta t + \vec{a}_i(t) \frac{\Delta t^2}{2}.\end{aligned}\quad (2.11)$$

3. Displace atoms in the system to their new positions.
4. For the system with displaced atoms calculate the new forces acting on the atoms, i.e. $\vec{F}_i(t + \Delta t)$ in Eq. (2.9).
5. Calculate new accelerations of atoms in the system

$$\vec{a}_i(t + \Delta t) = \vec{F}_i(t + \Delta t)/m_i.\quad (2.12)$$

6. Calculate new velocities of atoms in the system

$$\vec{v}_i(t + \Delta t) = \vec{v}_i\left(t + \frac{\Delta t}{2}\right) + \vec{a}_i(t + \Delta t) \frac{\Delta t}{2}.\quad (2.13)$$

Finally the calculated $\vec{r}_i(t + \Delta t)$, $\vec{v}_i(t + \Delta t)$, $\vec{a}_i(t + \Delta t)$ are used as initial coordinates, velocities and accelerations for the next step of the simulation. The procedure is continued for $N_{steps} = \tau/\Delta t$ steps, where τ is the desired simulation time.

Due to numerical errors, the total energy of the system in molecular dynamics simulation is never perfectly constant, and fluctuates. The degree of these fluctuations determine the precision of the calculation. The parameter, which governs the accuracy of the calculation is the time step of the simulation: decreasing its value results in more accurate calculation, but on the other hand leads to the increase of the simulation time.

2.1.3 Energy and temperature control of a system in molecular dynamics simulation

If a system is thermally and mechanically isolated, the total energy is constant in time according to the fundamental law about conservation of energy. However, in some simulations the energy or the temperature should be changed over the time, or should be kept as a constant. In physical experiments, the temperature is kept constant by letting the considered exchange heat with a significantly large system, the so-called heat bath or thermostat. The temperature of the heat bath is therefore

assumed to be constant, i.e., it is equal to a given value. In the course of time the smaller system adopts the temperature of the heat bath. To obtain the same effect in a simulation the system has to gain or lose energy in an appropriate way until the desired temperature is reached. The temperature control in molecular dynamics simulation is initiated by setting the thermostat.

Following the equipartition theorem [43], every degree of freedom in the system, f has the same kinetic energy, given by $\langle \mathcal{K} \rangle_f = \frac{1}{2}k_B T$. The effective temperature of the system is therefore given by the ensemble average of its kinetic energy.

$$T = \frac{2}{gk_B} \left\langle \sum_{f=1}^g \mathcal{K}_f \right\rangle = \frac{1}{3Nk_B} \left\langle \sum_{i=1}^N m_i \vec{v}_i^2 \right\rangle. \quad (2.14)$$

Here \mathcal{K}_f is the instantaneous kinetic energy of a degree of freedom f , g is the number of degrees of freedom, where N is the number of atoms having three degrees of freedom.

It is almost always desirable that a simulation is conducted so that the temperature is a supplied parameter rather than the kinetic energy. This requires some mechanism to fix the average kinetic energy at thermal equilibrium. The initial kinetic energy may be set approximately by choosing random velocities at the desired temperature, or specified through the velocities explicitly. But because the initial configuration is usually far from equilibrium it will have too much potential energy. As the simulation run progresses the potential energy will be converted into kinetic energy, raising the temperature above the desired value. It is therefore necessary to have some mechanism for removing excess kinetic energy in the course of the simulation.

Several mechanisms to control the temperature is known. In the present work two mechanisms to control system temperature are considered. The common technique of velocity scaling - Berendsen thermostat and the Nosé-Hoover method couples the system to a heat bath using a fictional dynamical variable.

Velocity scaling (Berendsen thermostat)

A popular velocity scaling thermostat is that of Berendsen [44]. At periodic intervals linear and angular velocities are multiplied by a factor of

$$\lambda = \sqrt{1 + \frac{\Delta t}{\tau_T} \left(\frac{T}{T_0} - 1 \right)}. \quad (2.15)$$

Here, T_0 is the setpoint temperature, Δt is the integration time step, and τ_T is a constant called the “rise time” of the thermostat. It describes the strength of the coupling of the system to a hypothetical heat bath. The larger τ_T , the weaker the coupling; in other words, the larger τ_T , the longer it takes to achieve a given T_0 after an instantaneous change from some previous T .

By repeatedly setting the “instantaneous” temperature to a given value during the simulation, the average kinetic energy is made to approach a constant value.

Nose-Hover thermostat

A coupling with to a heat bath can be achieved by an additional friction term in the equation of motion, then Newton’s equations has a form

$$m_i \vec{a}_i = \vec{F}_i - \xi m_i \vec{v}_i, \quad \text{for all } i = 1, \dots, N. \quad (2.16)$$

The additional force $-\xi m_i \vec{v}_i$ acting on atom i is proportional to the velocity of the particle. Here, the function $\xi = \xi(t)$ depends on time. It is positive if energy has to be removed from the system and negative if the energy has to be added to the system.

In the so-called Nosé-Hoover thermostat [45–47], the heat bath is considered as an integral part of the simulated system and directly enters the computations. The heat bath is represented by additional degree of freedom that also determines the degree of coupling of the molecular system to the heat bath. The evolution of the function ξ over time, which determines the strength of the function, is described in this approach by the ordinary differential equation

$$\frac{d\xi}{dt} = \left(\sum_{i=1}^N m_i \vec{v}_i^2 - 3Nk_B T^D \right) / M, \quad (2.17)$$

where T^D is the equilibrating temperature, M determines the coupling to the heat bath. A large value of M leads to a weak coupling. The value of this parameter must be set carefully, because if it is chosen to be too small the phase space of the system will not be canonical [47], and it is chosen to be too large the temperature control will not be efficient.

The friction term ξ one has to integrate in addition to the equation of motion (2.16).

2.2 Interatomic potentials: pairwise potentials

This section discusses the pairwise potentials which were used in calculations. In the case of the pairwise potentials, the total energy of the system consisting of N particles (atoms) can be calculated as:

$$U_{tot} = \sum_{i=1}^N \sum_{j<i}^N U(r_{ij}). \quad (2.18)$$

Here $U(r_{ij})$ is the pairwise interaction energy of atoms with indices i and j , and

$$r_{ij} = |\vec{r}_j - \vec{r}_i| = \sqrt{(r_{jx} - r_{ix})^2 + (r_{jy} - r_{iy})^2 + (r_{jz} - r_{iz})^2} \quad (2.19)$$

is the distance between atoms with indices i and j . According to the definition, Eq. (2.18), the force acting on the i -th particle is equal to the negative gradient of the potential taken in respect to the coordinate of the i -th atom:

$$\vec{F}_i = -\frac{\partial}{\partial \vec{r}_i} U_{tot} = -\frac{\partial}{\partial \vec{r}_i} \sum_{\substack{j=1 \\ j \neq i}}^N U(r_{ij}). \quad (2.20)$$

The parameters for pair-potentials which were used in calculations are listed in A.1.

2.2.1 Lennard-Jones potential

Form of the potential

At a simple level, two neutral atoms or molecules are subjected by two opposing forces: firstly, they are weakly attracted by van der Waals forces; secondly they are repelled by Pauli repulsion. The energy of interaction between two neutral atoms or molecules as a function of the distance between their centers can be approximated by a Lennard-Jones (LJ) potential. A form of the (LJ) potential was first proposed in 1924 by John Lennard-Jones [48]. The Lennard-Jones potential can be expressed in various forms. In the present work the following form is used

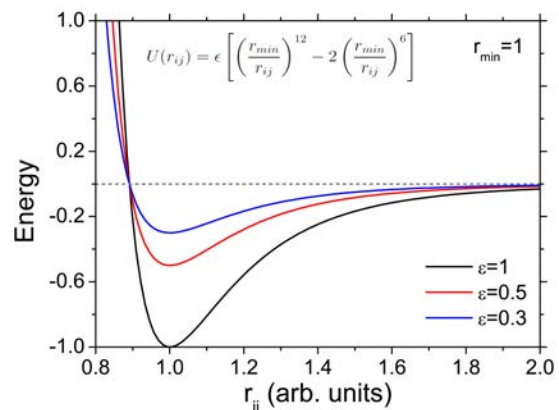


Figure 2.1: Lennard-Jones potential.

$$U(r_{ij}) = \epsilon \left[\left(\frac{r_{min}}{r_{ij}} \right)^{12} - 2 \left(\frac{r_{min}}{r_{ij}} \right)^6 \right]. \quad (2.21)$$

The force acting on the i -th atom in the system is then calculated according to Eq. 2.20 as

$$\vec{F}_i = -\frac{12\epsilon}{r_{min}^2} \sum_{\substack{j=1 \\ j \neq i}}^N \left[\left(\frac{r_{min}}{r_{ij}} \right)^{14} - \left(\frac{r_{min}}{r_{ij}} \right)^8 \right] \vec{r}_{ij}. \quad (2.22)$$

Parameters of the potential

Lennard-Jones potential specification requires two parameters: ϵ is measured in eV, and r_{min} is measured in Å. The parameter r_{min} is the distance at the minimum of the potential and ϵ is the depth of the potential energy well and thereby the strength of the repulsive and attractive force. Materials of different strength can be simulated with the Lennard-Jones potential. Increasing ϵ leads to stronger bonds and therefore harder materials. The parameters for Lennard-Jones potential, which were used in calculations are listed in A.1.

2.2.2 Morse potential

Form of the potential

The Morse potential is another pairwise potential which also used in the present work. The Morse potential, named after the physicist Philip M. Morse, is a convenient model for the potential energy of a diatomic molecule [49]. The Morse potential in its most general form

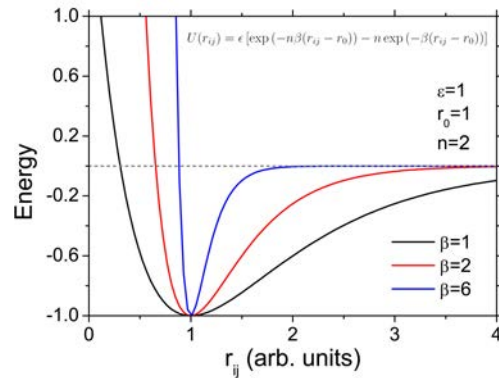


Figure 2.2: Morse potential.

$$U(r_{ij}) = \epsilon [\exp(-n\beta(r_{ij} - r_0)) - n \exp(-\beta(r_{ij} - r_0))]. \quad (2.23)$$

The force acting on the i -th atom in the system is then calculated, according to Eq. 2.20, as

$$\vec{F}_i = -\epsilon\beta n \sum_{\substack{j=1 \\ j \neq i}}^N [\exp(-n\beta(r_{ij} - r_0)) - \exp(-\beta(r_{ij} - r_0))] \frac{\vec{r}_{ij}}{r_{ij}}. \quad (2.24)$$

Parameters of the potential

The Morse potential specification requires four parameters ϵ is measured in eV, r_0 is measured in Å, β is measured in Å⁻¹, and n is dimensionless. The parameter r_0 is the distance which corresponds to the minimum of the potential and $\epsilon(n - 1)$ is the energy of the potential in its minimum. The parameters β and n define the steepness of the potential. The parameters for Morse potential, which were used in calculations are listed in A.1.

2.3 Interatomic potentials: many-body potentials

This section discusses the many-body potentials which were used in the present work.

In the case of a many-body potential, the total potential energy of the system consisting of N particles (atoms) is calculated as:

$$U_{tot} = \sum_{i=1}^N U_i(\{\vec{r}_i\}). \quad (2.25)$$

Here $U_i(\{\vec{r}_i\})$ is the energy term, describing the interaction of the i -th atom with all other particles in the system. In the most general case it depends on the position of all atoms in the system, i.e. $\{\vec{r}_i\}$.

According to the general definition the force acting on the α -th atom is equal to the negative gradient of the total potential energy taken in respect to the coordinate of this atom:

$$\vec{F}_\alpha = -\frac{\partial}{\partial \vec{r}_\alpha} U_{tot} = -\frac{\partial}{\partial \vec{r}_\alpha} \sum_{i=1}^N U_i(\{\vec{r}_i\}). \quad (2.26)$$

The parameters of all implemented many-body potentials which were used in calculations are listed in A.2.

2.3.1 Sutton-Chen potential

Form of the potential

The Sutton-Chen potential is often employed for the description of the interaction between metallic atoms, e.g. inside a metallic cluster or a nanoparticle [50]. The potential energy of N atoms calculated with the Sutton-Chen potential reads as

$$U_{tot} = \epsilon \left[\frac{1}{2} \sum_{\substack{j=1 \\ j \neq i}}^N v(r_{ij}) - c \sum_{i=1}^N \sqrt{\rho(r_i)} \right]. \quad (2.27)$$

Here ϵ and c are parameters of the potential, $v(r_{ij})$ is the pairwise part of the potential, defined as

$$v(r_{ij}) = \left(\frac{a}{r_{ij}} \right)^n, \quad (2.28)$$

with a and n being two further parameters of the potential. The second term in the brackets in Eq. (2.27) describes the nonlocal effects of the interatomic interaction. The function $\rho(r_i)$ is given by

$$\rho(r_i) = \sum_{\substack{j=1 \\ j \neq i}}^N \left(\frac{a}{r_{ij}} \right)^m, \quad (2.29)$$

with m being a parameter.

To calculate the forces acting on the particles in the system let us split the total energy U_{tot} in two parts

$$U_{tot} = U^{(R)} + U^{(A)}, \quad (2.30)$$

where

$$U^{(R)} = \frac{\epsilon}{2} \sum_{\substack{j=1 \\ j \neq i}}^N v(r_{ij}) \quad (2.31)$$

$$U^{(A)} = -c\epsilon \sum_{i=1}^N \sqrt{\rho(r_i)} \quad (2.32)$$

are the repulsive and the attractive energy terms of the potential respectively. According to Eq. (2.30) the force acting on the i -th atom in the system may be subdivided into attractive and repulsive terms. The repulsive force acting on the i -th atom reads as

$$\vec{F}_i^{(R)} = -\frac{\partial}{\partial \vec{r}_i} U^{(R)} = \sum_{\substack{j=1 \\ j \neq i}}^N \frac{n\epsilon}{2} \frac{a^n}{r_{ij}^{n+2}} \vec{r}_{ij} \quad (2.33)$$

The attractive force acting on the i -th atom in the system can be written as

$$\begin{aligned} \vec{F}_i^{(A)} &= -\frac{\partial}{\partial \vec{r}_i} U^{(A)} = \frac{c\epsilon}{2} \frac{1}{\sqrt{\rho(r_i)}} \left[\frac{\partial}{\partial \vec{r}_i} \sum_{\substack{j=1 \\ j \neq i}}^N \left(\frac{a}{r_{ij}} \right)^m \right] = \\ &= \frac{c\epsilon}{2} \frac{1}{\sqrt{\rho(r_i)}} \sum_{\substack{j=1 \\ j \neq i}}^N \frac{ma^m}{r_{ij}^{m+2}} \vec{r}_{ij}. \end{aligned} \quad (2.34)$$

The total force acting on the i -th atom in the system is a sum of repulsive (Eq. (2.33)) and attractive (Eq. (2.34)) force terms, than the total force can be written as:

$$\vec{F}_i = \frac{\epsilon}{2} \sum_{\substack{j=1 \\ j \neq i}}^N \left[\frac{na^n}{r_{ij}^{n+2}} + \frac{c}{\sqrt{\rho(r_i)}} \frac{ma^m}{r_{ij}^{m+2}} \right] \vec{r}_{ij}. \quad (2.35)$$

Parameters of the potential

The Sutton-Chen potential specification requires five parameters: ϵ is measured in eV, a is measured in Å; parameters c , n , m are dimensionless. The parameters of the Sutton-Chen potential have a complicated physical meaning. Thus, for example, ϵ does not correspond to the minimal energy value of the potential. The physical meaning of all parameters is discussed in the original paper [50], and in those papers where the Sutton-Chen potential was extensively used [51, 52]. The parameters for Sutton-Chen potentials which were used in calculations are listed in A.2.

2.3.2 Brenner potential

The bond-order Brenner [53] empirical potential was developed to model a covalent bonding in carbon-based materials. The Brenner potential for every atom in the system depends on the nearest neighbors for this atom. The total potential energy of the system, interacting via the Brenner potential is written as

$$U_{tot} = \frac{1}{2} \sum_{i=1}^N \sum_{\substack{j=1 \\ j \neq i}}^N U_{ij} = \frac{1}{2} \sum_i \sum_{i \neq j} f_{cut}(r_{ij}) [U^{(R)}(r_{ij}) - B_{ij} U^{(A)}(r_{ij})], \quad (2.36)$$

where $f_{cut}(r_{ij})$ is the cut-off function which limits the interaction of an atom to its nearest neighbors, defined as:

$$f_{cut}(r_{ij}) = \begin{cases} 1, & r_{ij} \leq R_1 \\ \frac{1}{2} \left[1 + \cos \left(\frac{r_{ij} - R_1}{R_2 - R_1} \pi \right) \right], & R_1 < r_{ij} \leq R_2, \\ 0, & r_{ij} > R_2 \end{cases} \quad (2.37)$$

with R_1 and R_2 being parameters which determine the range of the potential. The functions $U^{(R)}(r_{ij})$ and $U^{(A)}(r_{ij})$ in Eq. (2.36) are the repulsive and the attractive energy terms of the potential respectively. The Brenner potential implies the following parametrization for $U^{(R)}(r_{ij})$ and $U^{(A)}(r_{ij})$:

$$U^{(R)}(r_{ij}) = \frac{D_e}{S-1} \exp \left[-\sqrt{2S} \beta (r_{ij} - R_0) \right] \quad (2.38)$$

$$U^{(A)}(r_{ij}) = \frac{D_e S}{S-1} \exp \left[-\sqrt{\frac{2}{S}} \beta (r_{ij} - R_0) \right], \quad (2.39)$$

where D_e , S , β and R_0 are parameters. The factor B_{ij} in Eq. (2.36) is the so-called bond order term, which is defined as follows:

$$B_{ij} = \left[1 + \sum_{k \neq i, j} f_{cut}(r_{ik}) G(\theta_{ijk}) \right]^{-\delta} = [1 + \zeta_{ij}]^{-\delta}. \quad (2.40)$$

Here, $f_{cut}(r_{ik})$ is the cut-off function introduced in Eq. (2.37). The function $G(\theta_{ijk})$ is defined as:

$$G(\theta_{ijk}) = a_0 \left[1 + \frac{c_0^2}{d_0^2} - \frac{c_0^2}{d_0^2 + (1 + \cos \theta_{ijk})^2} \right], \quad (2.41)$$

where θ_{ijk} is the angle between bonds formed by pairs of atoms (i, j) and (i, k) , defined as

$$\cos(\theta_{ijk}) = \frac{\vec{r}_{ij} \cdot \vec{r}_{ik}}{r_{ij} r_{ik}}. \quad (2.42)$$

Let us consider an atom with index α and calculate the force which acts on it from the site of other atoms. According to the general definition given in Eq. (2.26)

$$\vec{F}_\alpha = -\frac{1}{2} \sum_{i, j}^N \frac{\partial}{\partial \vec{r}_\alpha} U_{ij}, \quad (2.43)$$

where $U_{ij} = f_{cut}(r_{ij}) [U^{(R)}(r_{ij}) - B_{ij}U^{(A)}(r_{ij})]$ is defined in Eq. (2.36). The calculation of the gradient in Eq. (2.43) is not that straightforward, as for the Sutton-Chen potentials. To calculate the forces acting between atoms we therefore first introduce several supplementary functions, which are used in further derivations. In particular,

$$f' = \frac{\partial}{\partial x} f(x) \quad (2.44)$$

$$\frac{\partial}{\partial \vec{r}_i} f(r_{ij}) = f' \frac{\partial}{\partial \vec{r}_i} r_{ij} \quad (2.45)$$

represent a derivative of a function f with respect to its argument x , and the gradient of this function taken with respect to \vec{r}_i . Performing elementary differentiation one obtains

$$\frac{\partial}{\partial \vec{r}_i} r_{ij} = -\frac{\vec{r}_{ij}}{r_{ij}} \quad (2.46)$$

$$\frac{\partial}{\partial \vec{r}_j} r_{ij} = \frac{\vec{r}_{ij}}{r_{ij}}. \quad (2.47)$$

Additionally

$$\frac{\partial}{\partial \vec{r}_\alpha} r_{ij} = \frac{\vec{r}_{ij}}{r_{ij}} (\delta_{\alpha j} - \delta_{\alpha i}), \quad (2.48)$$

where α is an arbitrary index of an atom and $\delta_{\alpha i}$ is the Kroniker delta function:

$$\delta_{ij} = \begin{cases} 0, & i \neq j \\ 1, & i = j \end{cases}. \quad (2.49)$$

Equations (2.38) and (2.39) can be unified as

$$U^{(x)} = A^{(x)} \exp[-B^{(x)}(r_{ij} - R_0)], \quad (2.50)$$

where the symbol $(x) = (A)$ or (R) , representing either the attractive or repulsive terms. The derivative of $U^{(x)}$ with respect to r_{ij} then reads as

$$(U^{(x)})'(r_{ij}) = -A^{(x)} B^{(x)} \exp[-B^{(x)}(r_{ij} - R_0)]. \quad (2.51)$$

Finally, the derivative of the cutoff function, Eq. (2.37), with respect to r_{ij} is given by

$$f'_{cut}(r_{ij}) = \begin{cases} 0, & r_{ij} \leq R_1 \\ -\frac{\pi}{2(R_2 - R_1)} \sin\left(\frac{r_{ij} - R_1}{R_2 - R_1} \pi\right), & R_1 < r_{ij} \leq R_2 \\ 0, & r_{ij} > R_2, \end{cases} \quad (2.52)$$

According to Eq. (2.43) the force acting on the atom with the index α reads as

$$\begin{aligned} \vec{F}_\alpha = & -\frac{1}{2} \sum_{i,j}^N \left[\left(\frac{\partial}{\partial \vec{r}_\alpha} f_{cut}(r_{ij}) \right) U^{(R)}(r_{ij}) + f_{cut}(r_{ij}) \left(\frac{\partial}{\partial \vec{r}_\alpha} U^{(R)}(r_{ij}) \right) - \right. \\ & \left. \left(\frac{\partial}{\partial \vec{r}_\alpha} f_{cut}(r_{ij}) \right) U^{(A)}(r_{ij}) B_{ij} - f_{cut}(r_{ij}) \left(\frac{\partial}{\partial \vec{r}_\alpha} U^{(A)}(r_{ij}) \right) B_{ij} - \right. \\ & \left. f_{cut}(r_{ij}) U^{(A)}(r_{ij}) \left(\frac{\partial}{\partial \vec{r}_\alpha} B_{ij} \right) \right] = -\frac{1}{2} \sum_{i,j}^N \left[\vec{F}_{ij}^{(1)} - \vec{F}_{ij}^{(2)} \right]. \quad (2.53) \end{aligned}$$

The term $\vec{F}_{ij}^{(1)}$ corresponds to the first four summands in the square brackets, i.e. this term does not include the gradient of B_{ij} . The term $\vec{F}_{ij}^{(2)}$ corresponds to the last summand in Eq. (2.53) and is governed by the gradient of B_{ij} . Thus, using the notations introduced in Eqs. (2.44)-(2.52) one obtains

$$\begin{aligned} \vec{F}_{ij}^{(1)} = & \frac{\partial}{\partial \vec{r}_\alpha} f_{cut}(r_{ij}) [U^{(R)}(r_{ij}) - B_{ij} U^{(A)}(r_{ij})] + \\ & f_{cut}(r_{ij}) \left[\frac{\partial}{\partial \vec{r}_i} U^{(R)}(r_{ij}) - B_{ij} \frac{\partial}{\partial \vec{r}_i} U^{(A)}(r_{ij}) \right] = \\ = & f'_{cut}(r_{ij}) [U^{(R)}(r_{ij}) - B_{ij} U^{(A)}(r_{ij})] \frac{\vec{r}_{ij}}{r_{ij}} (\delta_{\alpha j} - \delta_{\alpha i}) + \\ & f_{cut}(r_{ij}) [(U^{(R)})'(r_{ij}) - B_{ij} (U^{(A)})'(r_{ij})] \frac{\vec{r}_{ij}}{r_{ij}} (\delta_{\alpha j} - \delta_{\alpha i}). \quad (2.54) \end{aligned}$$

The next step is to calculate the gradient of B_{ij} in $\vec{F}_{ij}^{(2)}$ with respect to \vec{r}_α . Let us consider the gradient of B_{ij} independently before substituting it into $\vec{F}_{ij}^{(2)}$:

$$\frac{\partial}{\partial \vec{r}_\alpha} B_{ij} = \frac{\partial}{\partial \vec{r}_\alpha} [1 + \zeta_{ij}]^{-\delta} = -\frac{\delta}{[1 + \zeta_{ij}]^{\delta+1}} \left(\frac{\partial}{\partial \vec{r}_\alpha} \zeta_{ij} \right). \quad (2.55)$$

Substituting Eq. (2.40) into Eq. (2.55) one obtains

$$\frac{\partial}{\partial \vec{r}_\alpha} B_{ij} = -\frac{\delta}{[1 + \zeta_{ij}]^{\delta+1}} \sum_{k \neq i, j} \left[\left(\frac{\partial}{\partial \vec{r}_\alpha} f_{cut}(r_{ik}) \right) G(\cos(\theta_{ijk})) + f_{cut}(r_{ik}) G'(\cos(\theta_{ijk})) \left(\frac{\partial}{\partial \vec{r}_\alpha} \cos(\theta_{ijk}) \right) \right], \quad (2.56)$$

where

$$G'(\cos(\theta_{ijk})) = \frac{2ac_0^2(1 + \cos(\theta_{ijk}))}{[d_0^2 + (1 + \cos(\theta_{ijk}))^2]^2}. \quad (2.57)$$

Using Eq. (2.48), the gradients in Eq. (2.56) can be calculated as follows

$$\frac{\partial}{\partial \vec{r}_\alpha} f_{cut}(r_{ik}) = f'_{cut}(r_{ij}) \frac{\vec{r}_{ik}}{r_{ik}} (\delta_{\alpha k} - \delta_{\alpha i}) \quad (2.58)$$

and

$$\begin{aligned} \frac{\partial}{\partial \vec{r}_\alpha} \cos(\theta_{ijk}) &= \frac{\vec{r}_{ik}(\delta_{\alpha j} - \delta_{\alpha i}) + \vec{r}_{ij}(\delta_{\alpha k} - \delta_{\alpha i})}{r_{ij}r_{ik}} - \\ &- \cos(\theta_{ijk}) \left[\frac{\vec{r}_{ij}}{r_{ij}^2} (\delta_{\alpha j} - \delta_{\alpha i}) + \frac{\vec{r}_{ik}}{r_{ik}^2} (\delta_{\alpha k} - \delta_{\alpha i}) \right]. \end{aligned} \quad (2.59)$$

Substituting Eqs. (2.57)-(2.59) back into Eq. (2.56) one obtains the gradient of B_{ij} with respect to \vec{r}_α . Substituting then Eq. (2.56) into Eq. (2.53) one obtains the expression for $\vec{F}_{ij}^{(2)}$, which allows to calculate the force acting on the atom α , i.e. \vec{F}_α .

Parameters of the potential

The Brenner potential specification requires ten parameters: D_e is measured in eV; β is measured in \AA^{-1} ; S , δ , a_0 , c_0 , and d_0 are dimensionless; R_0 , R_1 , R_2 are measured in \AA . The parameters of the Brenner potential have a complicated physical meaning, which is discussed in original paper [53]. The parameters for Brenner potential which were used in calculations are listed in A.2.

2.4 Kinetic Monte - Carlo method

2.4.1 The motivation to use kMC

The time evolution of a system of interacting atoms in classical molecular dynamics simulation is determined by the integration of the Newtonian equations of atom's

motion. In numerical time integration, the solution of the considered equations is only computed at a number of discrete points in time. In other words, when we know the structure of atomic system at time moment t_1 , we can find the structure at the next time moment t_2 using the integration method of the equations of motion with time starting from moment t_1 . The process of integrating the equations of motion can be achieved by several kinds of algorithms. The commonly important concept in the various algorithms is the time step Δt . If a big time step is used, the motion of atoms becomes unstable due to the very big error occurring in the integration. Reversely, if a very small value of time step is used, it will not be efficient due to a very long calculation time. Therefore, the selection of the time step is very important. The time step should be chosen to be at least one order of magnitude smaller than the length of the time corresponding to the fastest motion in a system. Depending on the type of the system the time step can be between 0.5 fs – 10 fs (1 fs = 10^{-15} s) [54]. Thus, for the 1 s of the molecular dynamic simulation is needed to perform approximately 10^{15} time steps.

At each step of the MD simulation, the forces on the individual particles and their new positions and velocities are computed in an inner loop over all particles. There are N^2 interactions between particles in a system which consists of N particles. If self-interactions are excluded, this number is reduced by N . In total we obtain $(N^2 - N)/2$ actions between particles that have to be determined to compute the force between all particles. Therefore, this naive approach needs $O(N^2)$ operations for system of N particles in each time step. Thus, if the number of particles is doubled, the number of operations is quadruples. It is possible to reduce number of operations per time step at least of order of $O(N)$. To reach this reduction, it is very important to find an optimal algorithm and also implement them. The design of a suitable algorithm necessarily has to be adapted to the kind of interactions modeled and to other parameters. It is clear that algorithms, which are optimal for some forms of interaction potentials, may not be suitable for other forms of potentials. This can be demonstrated most easily by the difference between a potential that decay quickly and one that decay slowly. For a fast decaying potential, a particle act a significant force to another particle if the distance between two particles is small. The force calculation can then be implemented in $O(N)$ operations by introducing a distance cutoff, which gives a possibility to consider particles only in close vicinity of a particle contribute significantly to the force acting on it. The long-range forces such as Coloumb forces decays very slowly. Their effects can not be neglected for

particles are far apart.

In the present work, it was studied the formation and post-growth evolution of the nanofractals on a surface. The size of the nanofractals, which is grown by cluster deposition on a surface, depends on many factors, such as the deposition rate [15, 16], temperature [2], size and type of the deposited cluster [14], number of structure defects on a surface [55], and so on. In the present work, the silver fractal formation and fragmentation on graphite surface are discussed. The results of calculations are compared with the experimental observations of silver fractal formation and fragmentation, which are performed by C. Bréchnignac and co-workers [9, 10, 14, 17–19, 55]. The typical diameter of the silver fractal on graphite surface in experimental observation is around 500 – 1500 nm [9, 10, 19]. The typical silver fractal [9, 10, 19] of the diameter 500 nm is roughly consists on ~ 5000 silver clusters Ag_{500} . It means, that the MD simulation should be performed for 2.5×10^6 atoms. That corresponds to 2.5×10^6 operations per one MD step. The typical experimental time scale of silver fractals fragmentation by thermal annealing at the 1000 K in experiment is around 15 minutes. Approximately 10^{15} time steps are needed to perform for one second of the MD modeling of an evolution of one nanofractal, it is corresponded to 10^{22} operations. The real-time performance for the modern computer is 10^{-9} s pro basic operation [56]. In this naive approach the computational time of one second of a nanofractal fragmentation is equal to 3200 years. It shows, that the classical molecular dynamics method is hardly applicable for the modeling of silver fractal formation and fragmentation on a surface.

The kinetic Monte Carlo attempts to overcome these limitations of molecular dynamics approach by exploiting the fact that the long-time dynamics of a nanopattern on a surface typically consist of diffusive jumps of a single nanoparticle from state to state. In this type of modeling the long-time scale processes or effects, which are most important in the formation and post-growth evolution of a nanopattern on a surface, are considered.

2.4.2 Formalism of kinetic Monte Carlo method

The kinetic Monte - Carlo method (kMC) is based on the Monte - Carlo algorithm and is widely used for the study of time evolution of various processes occurring in different physical systems [57–59], such as surface diffusion of particles [60], vacancy diffusion in alloys [61], damage accumulation and amorphization [62] and many

others.

In the kinetic Monte Carlo method only most important processes or effects are considered. For example, in case of the nanostructure formation on a surface, deposition, diffusion and aggregation of nanoparticles on a surface are most important processes, which can be taken into account in kMC. The kinetic Monte Carlo coarse - grains the details of the behavior of a nanoparticle, but retains much of the microscopic morphological information. The principal drawback of the kMC is that mechanistic information must be added externally through the selection of suitable processes. The processes in kMC method always occur with certain predefined rates. Note that these rates are input in the kMC algorithm and the method itself cannot predict them. The calculation of the kinetic rates for different processes is usually a nontrivial problem. The kinetic rates are material-based parameters of the kMC method, which in the case of particle diffusion on surface are determined by the atomic composition of particles, substrate material and interparticle interactions. Therefore, by varying the values of the kinetic rates the kMC method can be used to study dynamical behavior of various molecular systems.

The idea of the kMC method is as follows. The time-evolution of a molecular system is modeled stepwise in time. With a certain probability, at each step of the simulation, the system undergoes a structural transformation. The new configuration of the system is then used as the starting point for the next simulation step. The transformation of the system is governed by the kinetic rates, input into the kMC method. Note, that at each simulation step the system can be transformed into one of several states. Thus, in the kMC method, the probability for the system to attain a certain configuration is proportional to the corresponding kinetic rate.

In the conventional kMC method at each simulation step, all possible events are grouped into different types according to their rates. Each rate can include multiple (different) events that possess with the same rate, thereby reducing the number of unique event types in the simulation. The list of all possible event is shown in Fig. 2.3. The sum P of all the rates of the events that are possible at any given time is defined as:

$$P = \sum_{i=1}^k n_i \Gamma_i, \quad (2.60)$$

where n_i is the number of events with the rate Γ_i , k is the number of unique event types. When the list of all possible events are created, first the event type randomly pick up from the list of the events. For it, a random number $\rho \in (0, 1]$ selects a

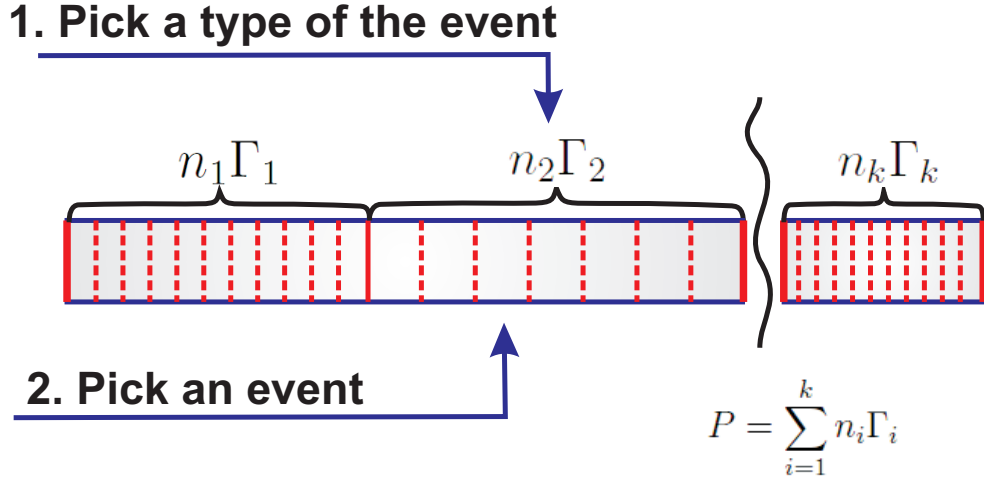


Figure 2.3: Schematic representation of the main procedure for picking the pathway to advance the system to the next state in the standard kinetic Monte-Carlo method.

event type as

$$\sum_{i=1}^{j-1} n_i \Gamma_i < \rho P \leq \sum_{i=1}^j n_i \Gamma_i. \quad (2.61)$$

Once the rate type is selected, a particular event of the selected type is randomly chosen. When the selected event is executed and the local configuration of the system is changed, the new list of the possible events is created. Update of the simulation type related to the rate of the event as

$$t = t + \Delta t, \quad \text{where } \Delta t = \frac{1}{P} \ln(\rho^{-1}), \quad (2.62)$$

where ρ is another uniform random value, $\rho \in (0, 1]$.

In the practical implementation of kMC algorithms, there are two main concerns that affect the computational efficiency. First, the selection of a suitable algorithm depends on the question how many process types are typically active at each moment in time. The second concern is to find an efficient scheme of representing and updating the data. A complete re-build of the list of possible events after each simulation step would be too time-consuming.

The kinetic Monte carlo method is ideal for studying system evolution, when the details of the individual kinetic processes of a system are not important, and can be described as jumps from one state to another.

Chapter 3

Cluster on a surface

Different morphologies of nanostructured pattern can be built by depositing preformed clusters on a surface: separated (and hopefully ordered) nanoislands, thin films or cluster-assembled structures. The main advantage of cluster deposition technique is that one can control initial properties of a cluster (for example the size of a cluster) and characterize the growth mechanisms and properties of thin films [2, 3, 6, 63].

Atomic clusters have been extensively studied in recent decades. Much attention has been devoted to the physical and chemical properties of free clusters (see, e.g. [64–67] and references therein). However, properties of an atomic cluster on a surface can be significantly different from the properties of an analogous free cluster [2, 3, 7]. The difference is caused by the interaction between the cluster and the solid. Therefore, the understanding of structural and dynamical properties of an atomic cluster on a surface is a topic of intense interest from the scientific and technological points of view [2, 8].

In this chapter, several aspects of a cluster behavior on a surface are discussed. In section 3.1 stability, energy, and geometry of an atomic cluster on a solid surface are studied. In the present study, the droplet model was used to describe the interaction of incompressible atomic cluster with a solid surface. For this purpose, the model equation was supplemented with a term describing the interaction between the cluster and the solid and took into account geometric corrections describing deformation of the cluster shape. As an example, the model was used to consider interaction between an argon cluster with $N = 1 - 150$ and a (001) surface of graphite. The proposed model describes with good accuracy the geometry, stability, and energy characteristics of inert gas clusters interacting with the solid surface. But the droplet model can be generalized to the case of cluster with various types

of chemical bonds between atoms. In particular, the structure of metal clusters can be described within the framework of droplet model [68, 69]. In presented thesis, it was used to describe structure deformation and energetic of a silver cluster on a solid graphite surface.

Diffusion is an important factor in the fabrication of thin films and self-organized structures by deposition of atomic clusters on a surface [18, 19, 70]. It has been demonstrated experimentally that many metallic clusters diffuse on graphite surface at room temperature with a high rate, the diffusion coefficient of a cluster is comparable to that of a single adatom [15, 19, 71]. In the present work, diffusion process of a cluster on a surface was studied theoretically. One of the main methods used for modeling the diffusion of a cluster over a surface is the numerical simulation based on the molecular dynamics approach. In section 3.2, the results of modeling silver cluster diffusion on a solid graphite with the MD technique are presented. The values of diffusion coefficients are obtained from the analysis of trajectories of the clusters. The influence of various essential parameters of the system on the diffusion of clusters was studied. In particular, the following parameters was considered: the cluster size, the binding energy between silver and carbon atoms in the system and the temperature. The results of the calculations are compared with the available experimental results for the diffusion coefficient of silver clusters on graphite surface.

3.1 Liquid drop model of a cluster on a surface

The aim of this study was to develop a simple method for the description of the geometry (shape), stability, and energy characteristics of an atomic cluster of arbitrary size on a solid surface. The proposed method is based on a droplet model, which was originally formulated by Rayleigh in 1879 for the description of a drop of incompressible liquid [72]. The first variant of a droplet model of the atomic nucleus was proposed in 1928 by Gamow [73]. Later, the droplet model was successfully applied by Bohr and Wheeler [74] to the description of stability and fission of atomic nuclei. This model was previously employed for the description of fission of atomic clusters (see, e.g., [75–78] and references therein) and successfully used it to explain the growth of the total binding energy of the free clusters of inert gases (*Ne*, *Ar*, *Kr*, *Xe*) with increasing size of the system [75].

In the present study, the droplet model is used to describe the interaction of an incompressible atomic cluster with a solid surface. For this purpose, the model

equation is supplemented with a term describing the interaction between the cluster and the solid and took into account geometric corrections describing deformation of the cluster shape. As an example, the proposed model is used to consider the interaction between an argon cluster with $N = 4 - 150$ and a (001) surface of graphite.

3.1.1 Droplet model of a free cluster

The structures and energy characteristics of most stable free clusters with the van der Waals type of interatomic bonds have been studied in much detail [75, 79, 80]. The problem of determining the structure of a cluster with the minimum total energy (i.e., of the most stable cluster) is closely related to searching for the global minimum of the function of potential energy in a multidimensional space. Various methods and algorithms of global optimization have been developed for solving such problems [81]. An effective method for calculating optimized structures of atomic clusters is offered by the dynamic search for the most stable isomers in the course of cluster growth, that is, by the (cluster fusion algorithm, CFA) [80, 82–84].

The interaction between atoms of inert gases (*Ne, Ar, Kr, Xe*) can be described using various pairwise potentials [65]. In this study, we use the Lennard-Jones (LJ) potential, which provides description of the structure, magic numbers, and energy characteristics of inert gas clusters with sufficiently high accuracy [79, 80]. More information about the LJ potential you can find in section 2.2.1. The values of LJ parameters for various types of interacting particles are given in monograph [85]. For a cluster of particles featuring pairwise interaction (2.21), the coordinates and total energy can be scaled so as to eliminate the need for repeated optimization of the cluster structure upon variation of the values. In particular, the optimized structures and binding energies of clusters for the LJ potential with $r_{min} = 1$ and $\epsilon = 1$ were calculated earlier in [80, 82]. For argon clusters, the optimum bond length and potential depth values are $r_{min} = 3.8 \text{ \AA}$ and $\epsilon = 0.0123 \text{ eV}$ respectively.

Fig. 3.1 (points) presents a plot of the binding energy E_b (normalized to the number N of particles) for free clusters of argon, defined as

$$\frac{E_b}{N} = -\frac{E_N}{N}, \quad (3.1)$$

where E_N is the total energy of a cluster consisting of N atoms. The plot of E_b/N was constructed by scaling the results of numerical calculations performed previously [75, 80] for the LJ potential with $r_0 = \epsilon = 1$. As can be seen from Fig. 3.1, the

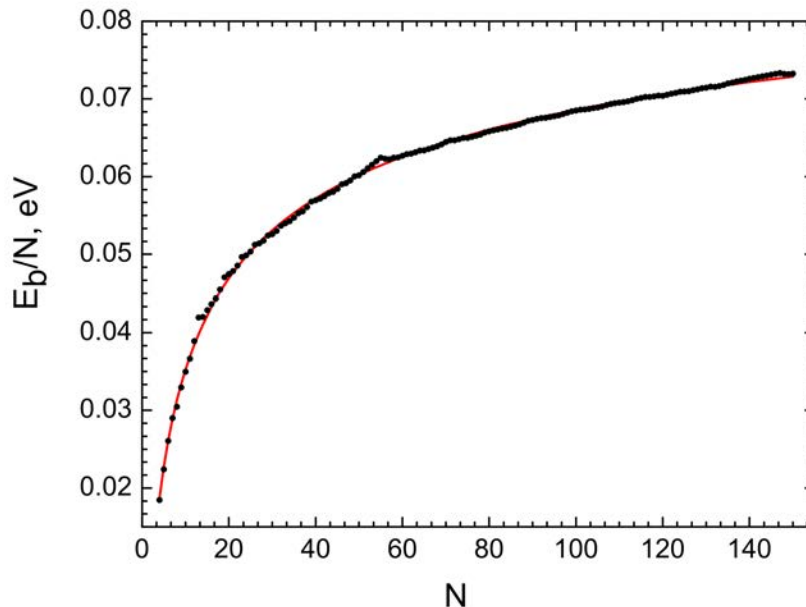


Figure 3.1: A plot of the binding energy E_b (normalized to the total number N of particles) versus N . Points present the results of numerical calculations employing the CFA; solid curve shows the results of calculations using the droplet model [75].

binding energy of a cluster almost monotonically increases with the number N of particles. Small deviations from the strictly monotonic behavior of the E_b/N versus N curve correspond to the most stable clusters (Ar_{13} , Ar_{55} , Ar_{135}), which have closed geometric shells and form regular icosahedrons [75]. It was shown [75, 80] that the binding energy of a free cluster of argon can be calculated within the framework of the droplet model with an accuracy on the order of 1%. According to this model, the cluster represents an incompressible drop of spherical shape. The radius R of a cluster consisting of N particles is defined as $R = r_s N^{1/3}$, where r_s is the Wigner-Seitz cell radius. For argon atoms, $r_s = 1.8 \text{ \AA}$ [85]. The total energy of a free cluster within the framework of the droplet model can be represented as the sum of contributions due to the volume energy (E_V), surface energy (E_S), and curvature energy (E_R):

$$E^{LDM} = E_V + E_S + E_R \equiv \lambda_V V + \lambda_S S + \lambda_R \int_S H dS, \quad (3.2)$$

where V is the cluster volume, S is the cluster surface area, H is the average curvature at a point on the cluster surface [86], and λ_V , λ_S , and λ_R are universal parameters of the model. It should be noted that the third term in Eq. (3.2) is a

correction to the energy of a cluster surface that takes into account its curvature. Indeed, an atom occurring on a convex surface effectively interacts with a smaller number of neighbors than does an atom on a concave surface. An analogous method of taking into account the surface curvature was proposed by Strutinsky [87] for determining the influence of deformation of a nucleus in the process of fission [87]. For a spherical cluster, the volume, surface, and integral curvature are given by the following formulas:

$$V = \frac{4}{3}\pi R^3 = \frac{4}{3}\pi r_s^3 N, \quad (3.3)$$

$$S = 4\pi R^2 = 4\pi r_s^2 N^{2/3}, \quad (3.4)$$

$$\int_S H dS = \int_S \frac{1}{R} dS = 4\pi r_s^2 N^{1/3}, \quad (3.5)$$

Using these expressions, the total energy of a free clusters of the spherical shape can be written as

$$E_{sphere}^{LDM} = \lambda'_V N + \lambda'_S N^{2/3} + \lambda'_R N^{1/3}, \quad (3.6)$$

where $\lambda'_V = 4/3\pi r_s^3 \lambda_V$, $\lambda'_S = 4\pi r_s^2 \lambda_S$, $\lambda'_R = 4\pi r_s \lambda_R$. The first and second terms in Eq. (3.6) correspond to the volume energy (E_V) and the surface energy (E_S), which are proportional to the number of particles in the bulk and on the surface, respectively. The third term in Eq. (3.6) is determined by the curvature of the cluster surface. The values of parameters λ'_V , λ'_S , and λ'_R can be refined by fitting to the total energy calculated with allowance for the exact positions of atoms in the system [75, 80]. Figure 3.1 (solid curve) shows the binding energy per particle, which was calculated as a function of their number N within the framework of the droplet model with the following coefficients: $\lambda'_V = -0.11$ eV, $\lambda'_S = +0.19$ eV, and $\lambda'_R = -0.08$ eV. Note that the contributions due the volume and surface energies have opposite signs. This implies that, at a fixed volume, it is energetically favorable for a free cluster to have a minimum surface area. The sign of λ'_R is determined by the deviation of a real cluster shape from spherical, and this parameter can take both positive and negative values. As can be seen from Fig. 3.1, the droplet model is capable of describing the binding energy of a free cluster of an inert gas with quite high accuracy.

3.1.2 Droplet model of an atomic cluster on a solid surface

Spherical clusters

For a spherical cluster on the surface of a solid, the total energy of the system is the sum of the energy of this solid (E_{bulk}), the energy of a free cluster (E_{sphere}^{LDM}), and the energy of interaction (E_{int}) between the cluster and the solid:

$$E = E_{bulk} + E_{sphere}^{LDM} + E_{int}, \quad (3.7)$$

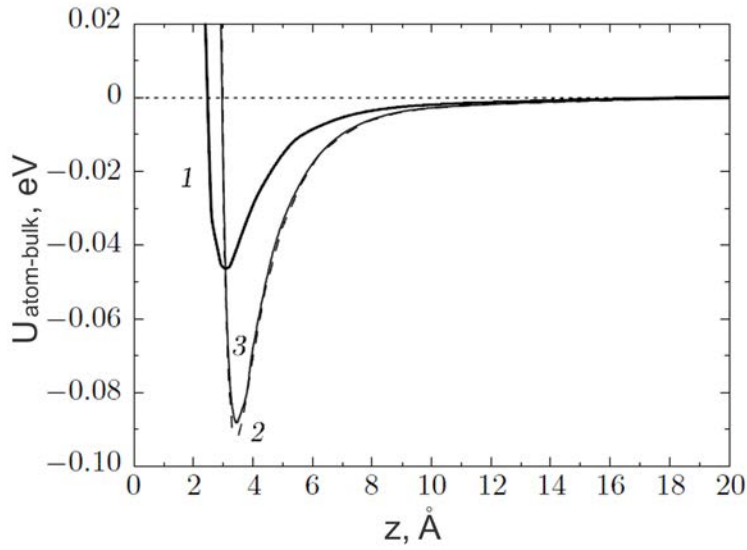


Figure 3.2: The potential of interaction between an atom and a solid surface as a function of the distance z : (1) for an Ar atom interacting with the surface of graphite as described by formula (3.9); (2) for an Ar atom interacting with a graphite fragment ($30 \times 30 \times 2$ unit cells) as described by formula (3.8); (3) for an Ar atom interacting with the surface of graphite, as calculated with allowance for the short-range-order effects in a cylindrical region with a radius of $R_{cyl} = 8 \text{ \AA}$ and a height of $H_{cyl} = 3.3 \text{ \AA}$.

In the present study, the effects related to deformation of the solid surface is ignored. This situation corresponds to the case of a cluster interacting with the surface of a hard solid. In particular, this approximation is valid for the interaction of an inert gas cluster with the surface of graphite. In such cases, the value of E_{bulk} remains unchanged when a cluster occurs on the surface and, hence, this term can be excluded from consideration. Let us consider the interaction of an argon cluster and a (001) graphite surface. The solid is modeled by a fragment of graphite structure with finite dimensions ($30 \times 30 \times 2$ unit cells). The characteristic size of this fragment is significantly greater than the size of Ar clusters under consideration,

thus eliminating the edge effects. The interaction between argon and carbon atoms is described by the LJ potential (2.21) with the parameters $r_0 = 3.84 \text{ \AA}$ and $\epsilon = 4.98 \times 10^{-3} \text{ eV}$ [88, 89].

The potential of interaction between an atom and a solid, $U_{atom-bulk}$, can be determined by summing expression 2.21 over all atoms of the solid:

$$U_{atom-bulk}(\vec{r}) = \sum_j^{bulk} U_{LJ}(r_j). \quad (3.8)$$

Here, \vec{r} is the radius vector determining the position of the given atom with respect to the solid surface and r_j is the distance from the given atom (occurring on the surface) to the j -th atom of the solid.

Assuming that the solid medium is amorphous and ignoring the short-range order of the interaction, we can replace the sum over atoms by the integral over the volume of the solid. In this case, the interaction potential depends only on the distance z from the given atom to the solid surface:

$$U'_{atom-bulk}(z) = \frac{1}{V_1^{bulk}} \epsilon r_0^6 \pi \left(\frac{r_0^6}{45z^9} - \frac{1}{3z^3} \right), \quad (3.9)$$

where r_0 and ϵ are parameters of the LJ potential (2.21) and V_1^{bulk} is the volume per particle of the solid.

Figure 3.2 shows the potential of interaction between an *Ar* atom and a graphite surface as a function of the distance z , where curve 1 represents the $U'_{atom-bulk}(z)$ potential calculated using Eq. (3.9) and curve 2 corresponds to the $U_{atom-bulk}(z)$ potential calculated via Eq. (3.8) by directly summing the pairwise potential over all atoms of the solid. The *Ar* atom occurred on an axis perpendicular to the solid surface and passing through the center of a hexagonal carbon ring situated on this surface.

As can be seen from Fig. 3.2, at small distances from the surface ($z < 8 \text{ \AA}$), the interaction potential 3.2 for an *Ar* atom on the graphite surface is overstated as compared to the potential of interaction of an *Ar* atom with a finite fragment of graphite. This difference is explained by the need for exactly taking into account the graphite structure at short distances. Indeed, the graphite structure comprises sequential layers, which are parallel to the base plane and are composed of carbon atoms bound in hexagonal rings. Therefore, the assumptions concerning the amorphous character of the solid and the absence of short-range-order effects, which were

made in deriving Eq. (3.9), are not valid for z values comparable with the crystal lattice parameters of the solid. At a sufficiently large distance from the surface, features of the crystal structure do not influence the interaction potential. As can be seen from Fig. 3.2, curves 1 and 2 asymptotically coincide for $z > 10$ Å. It should also be noted that, at distances from the surface equal to or greater than the equilibrium value $z_0 = 3.5$ Å, the interaction potential weakly depends on the x and y coordinates. This circumstance significantly simplifies subsequent calculations.

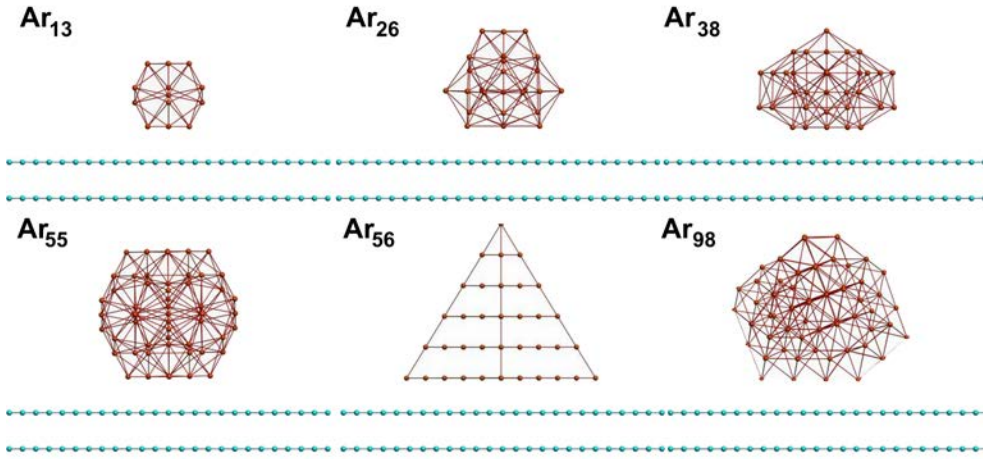


Figure 3.3: Undeformed Ar_{13} , Ar_{26} , Ar_{38} , Ar_{55} , Ar_{56} , and Ar_{98} clusters on the graphite surface (side view).

From computational standpoint, it is expedient to perform direct summation only for atoms of the solid occurring at small distances from the atom whose interaction potential is calculated. For greater distances, the interaction potential can be determined by integration over the volume of the solid except for a region where the short-range-order effects have to be taken into account. In Fig. 3.2, curve 3 shows the interaction potential calculated with allowance for the short-range-order effects in a cylindrical region with a radius of $R_{cyl} = 8$ Å and a height of $H_{cyl} = 3.3$ Å, while the contribution from the volume of solid outside this cylinder was determined by integration over this region. As can be seen from Fig. 3.2, curves 2 and 3 are very close to each other, which is evidence for the efficacy of the proposed method even for a small size of the region in which the short-range-order effects are taken into account. The energy of the interaction between a cluster and a solid can be determined by double summation of expression (1) over all atoms of the cluster and the

solid:

$$E_{int} = \sum_i^{clust} \sum_j^{bulk} U_{LJ}(r_{ij}), \quad (3.10)$$

where r_{ij} is the distance from the i th atom of the cluster to the j th atom of the solid.

Ignoring the dependence of the interaction potential on the x and y coordinates, we can replace the sum over atoms by the integral over the volume of the cluster (V_{cl}):

$$E'_{int} = \frac{1}{V_1^{clust}} \int_{V_{cl}} U_{atom-bulk}(z) dV, \quad (3.11)$$

where V_1 is the volume per particle in the cluster. This expression can be used to calculate the energy of interaction between a cluster and a solid. Note that, as the distance z from atoms in the cluster to the solid surface increases, the potential $U_{atom-bulk}$ decreases as $1/z^3$. For this reason, it is sufficient to restrict the integration in Eq. (3.11) to a region of the cluster in the immediate vicinity of the solid surface, at distances not exceeding a certain effective radius of interaction z_{eff} . This effective parameter determines the accuracy and efficacy of calculations of the energy of the cluster - solid interaction. For the interaction of Ar clusters with a graphite surface, it is sufficient to set $z_{eff} = 10 \text{ \AA}$ to ensure an accuracy of 1 – 3%.

Figure 3.3 shows the systems of Ar_{13} , Ar_{26} , Ar_{38} , Ar_{55} , Ar_{56} , and Ar_{98} clusters on the graphite surface, which are optimized with respect to the mutual orientation and the distance from a cluster to the solid surface. The geometry of clusters was fixed in the state corresponding to the optimum structure of free Ar clusters. Depending on the cluster shape and size, the optimum distance between the cluster and the graphite surface varies within small limits (3.45 – 3.50 \AA) and influences the energy of the cluster - solid interaction hardly at all. For this reason, we can assume that all clusters, irrespective of their shapes, are situated on the same distance ($z_0 = 3.5 \text{ \AA}$) from the surface of graphite. In this case, the energy of interaction of a spherical cluster with a solid surface is described by the following expression:

$$E_{int}^{sphere} = \frac{\pi}{V_1^{clust}} \int_{z_0}^{\min(z_{eff}, z_0 + 2R)} (R^2 - (R + z_0 + z)^2) U_{atom-bulk}(z) dz, \quad (3.12)$$

Figure 4a shows a schematic diagram of the undeformed spherical cluster on the solid surface.

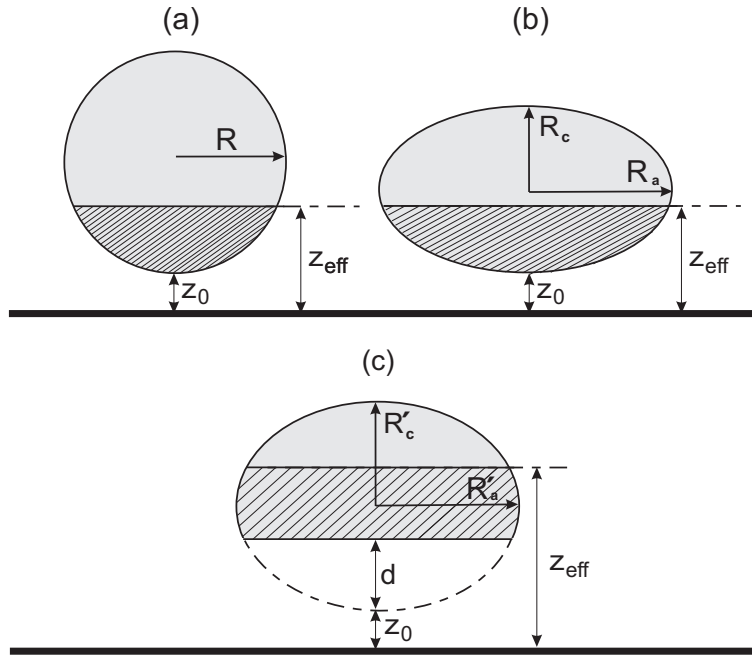


Figure 3.4: Schematic diagram of clusters on the solid surface: (a) undeformed spherical cluster; (b) cluster with allowance for deformation in the form of an oblate ellipsoid; (c) same for a truncated oblate ellipsoid.

Subdividing a cluster interacting with a solid surface into n elementary layers parallel to the surface, we can approximately represent the cluster - solid interaction energy by a finite sum

$$E_{int} \approx \sum_{i=1}^n \lambda_i V_i, \quad (3.13)$$

where V is the total cluster volume, V_i is the volume of the i th layer, $\sum_{i=1}^n V_i = V$, and λ_i are coefficients dependent on the distance from the i th layer to the solid surface. In cases where the form of the interaction potential between an atom and the solid is unknown, these coefficients can be determined by fitting to the energy of interaction of the undeformed cluster calculated using the CFA.

Let us consider the binding energy for Ar clusters interacting with the graphite surface. Figure 3.5 (points) shows the results of calculations of the binding energy per atom within the framework of the CFA (i.e., with allowance for the exact atomic structures of the cluster and solid) for Ar_4 , Ar_6 , Ar_{13} , Ar_{26} , Ar_{38} , Ar_{55} , Ar_{98} , Ar_{135} , and Ar_{147} clusters interacting with the graphite surface. The solid curve represents the results of calculations performed within the framework of the droplet model for the interaction of a spherical cluster with the same surface. As can be seen, the

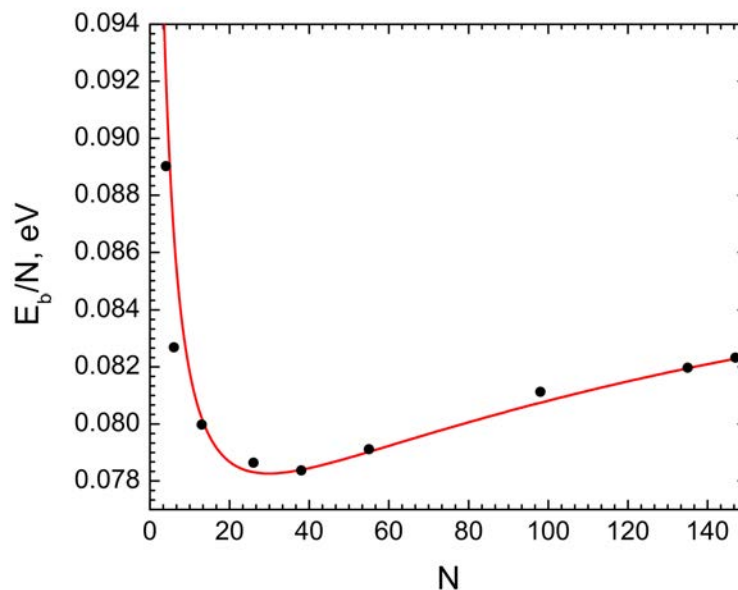


Figure 3.5: Binding energy E_b/N (normalized to the number of particles) as a function of the cluster size N calculated for undeformed Ar clusters on the graphite surface within the framework of the CFA (points) and the droplet model (solid curve).

binding energy first rapidly decreases with increasing number N of particles in the range from 1 to 30 and then slowly increases with the further growth in N . The minimum at $N = 30$ is determined by the competition between the contributions to the cluster binding energy due to the surface energy and the cluster - solid interaction energy.

Figure 3.6 shows variation of the contributions of various components (E_V/N , E_S/N , E_R/N , and E_{int}/N) to the binding energy. As can be seen, the relative contributions from the cluster surface and the cluster - solid interaction to the total binding energy E_b/N have opposite signs and both decrease in magnitude with increasing number of particles in the cluster. The behavior of the total binding energy with increasing N observed for undeformed Ar cluster shows evidence for the instability of clusters on the solid surface with respect to fission and/or deformation, since the total binding energy of the initial cluster is smaller than the sum of energies of the fragments (Fig. 3.5). Obviously, it is energetically favorable for such a system to decay into smaller fragments and/or to deform. Figure 3.7 shows the dependence of the normalized binding energy E_b/N on the cluster radius (up to $R = 11$ nm, which corresponds to an Ar cluster consisting of $N = 2 \sim 10^5$ atoms). As can

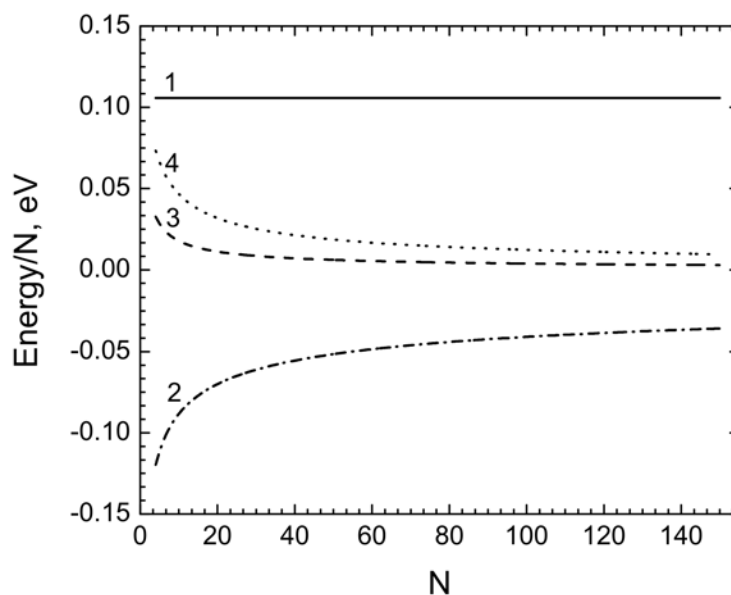


Figure 3.6: Contributions of various components to the binding energy (per atom) calculated within the framework of the CFA for undeformed Ar clusters on the graphite surface: (1) volume energy E_V/N ; (2) surface energy E_S/N ; (3) surface curvature energy E_R/N ; (4) cluster - solid interaction energy E_{int}/N .

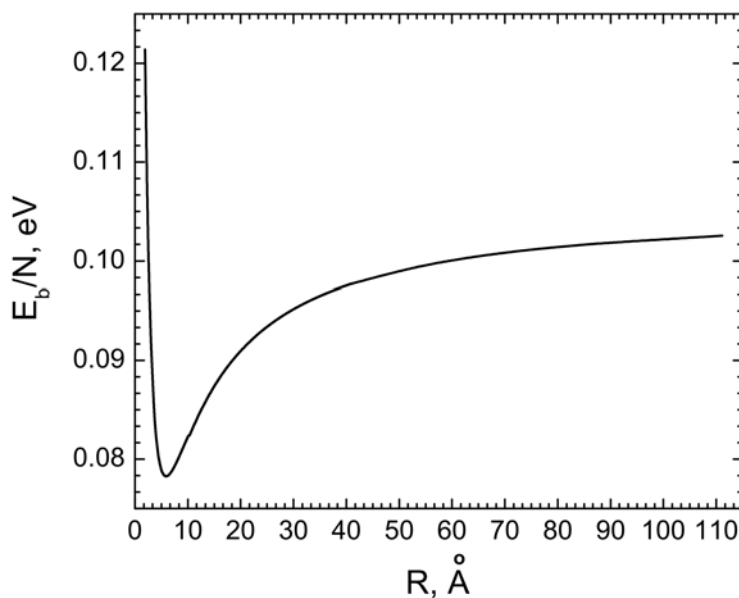


Figure 3.7: A plot of the normalized binding energy E_b/N versus radius of an undeformed Ar cluster on the graphite surface, calculated within the framework of the droplet model.

be seen, *Ar* clusters on the graphite surface are unstable with respect to fission and/or deformation, irrespective of size. It should be noted that the important role of deformation in determining the stability was also demonstrated for free clusters [3538, 47].

The various channels of fission for an atomic cluster on the surface of a solid are analyzed. First, consider the decay of the initial Ar_N cluster into two fragments, Ar_P and Ar_{N-P} , with the numbers of particles P and $N-P$, respectively. Figure 3.8

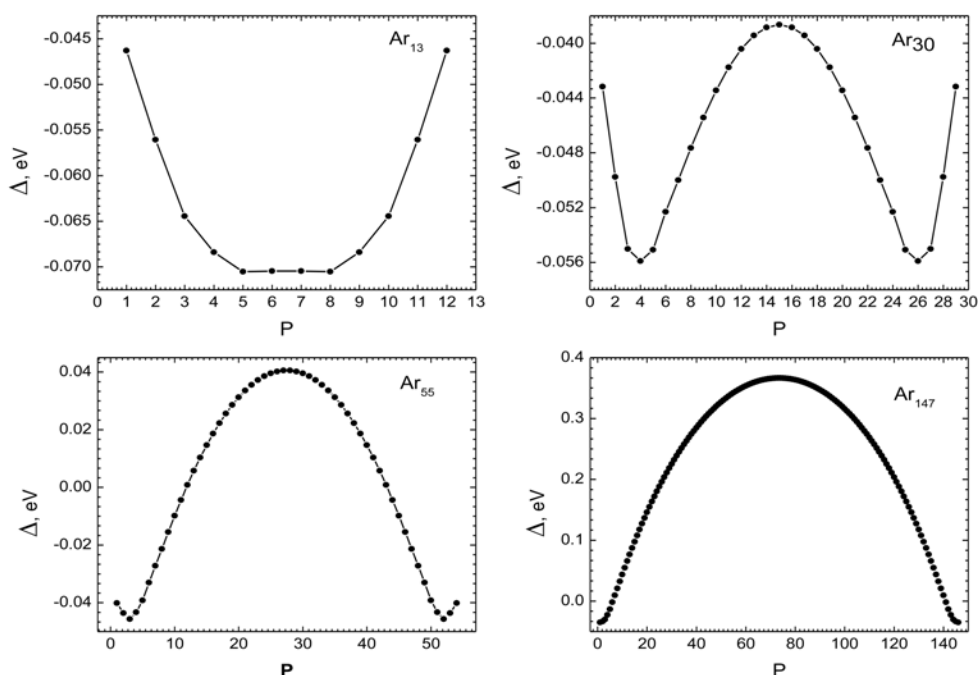


Figure 3.8: Plots of the energy balance Δ versus decay channel P for the fission of Ar_{13} , Ar_{30} , Ar_{55} , and Ar_{147} clusters into two fragments on the graphite surface.

shows the energy balance Δ as a function of P for the fission of Ar_{13} , Ar_{30} , Ar_{55} , and Ar_{147} clusters into two fragments. The Δ value is defined as the difference between the sum of energies of the fragments, E_P and E_{N-P} , and the energy of the initial cluster:

$$\Delta = (E_P + E_{N-P}) - E_N. \quad (3.14)$$

As can be seen from Fig. 3.8, relatively small clusters are unstable with respect to the two-particle decay for any P , since Δ always takes negative values. For the Ar_{13} cluster, more energetically favorable is a symmetric decay channel, whereby the initial cluster splits into two fragments of equal size. This type of decay is favorable

for the clusters containing 18 or fewer atoms. As the number of atoms (cluster size) increases, asymmetric decay channels begin to predominate. For $N = 34$ and above, Ar clusters become stable with respect to the symmetric decay (for which $\Delta > 0$), because this channel implies the consumption of energy. In the presence of the instability of clusters with respect to decay on the surface of a solid, it is necessary to take into account the possible deformation of clusters. The deformation leads to an increase in the volume of that part of the cluster which is involved in the interaction with the surface, which results in an increase in the binding energy of the system.

Deformed clusters

In order to take into account the deformation of a cluster interacting with the surface of a solid, let us consider parametrization of the shape of revolution (Fig. 3.4c). A particular case of such deformation is an untruncated ellipsoid of revolution (Fig. 3.4b), for which the values of semiaxes R_a and R_c are conveniently expressed as

$$R_a = \left(\frac{2 - \delta}{2 + \delta} \right)^{1/3} R, \quad R_c = \left(\frac{2 + \delta}{2 - \delta} \right)^{2/3} R, \quad (3.15)$$

where R is the radius of an undeformed (spherical) cluster and δ is the deformation parameter, which varies within $]2, 0]$ for an oblate ellipsoid of revolution and within $[0, 2[$ for an elongated ellipsoid of revolution. An important property of parametrization 3.15 is that it retains the cluster volume.

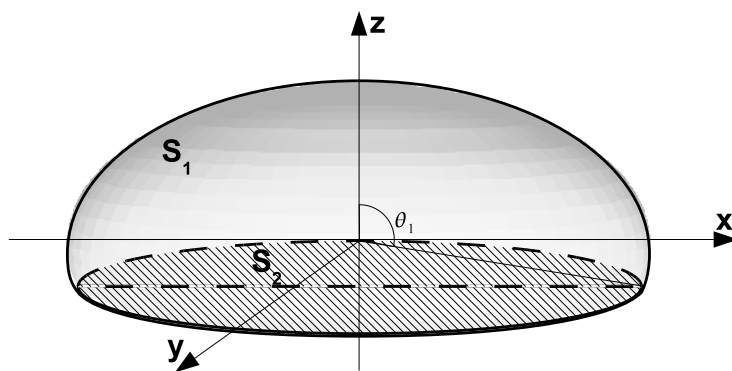


Figure 3.9: Schematic diagram of a truncated oblate ellipsoid of revolution.

For neutral clusters on a solid surface, the parametrization in terms of an oblate ellipsoid of revolution is always energetically more favorable as compared to the

elongated ellipsoid. Note, however, that the behavior of charged clusters can be significantly different because it will be necessary to take into account the repulsive Coulomb forces. In the case of a truncated oblate ellipsoid of revolution (Fig. 3.4c), the values of semiaxes depend on two parameters, the deformation δ and the height d of the truncated part:

$$R'_a = \left(\frac{2-\delta}{2+\delta}\right)^{1/3} R'(\delta, d), \quad R'_c = \left(\frac{2+\delta}{2-\delta}\right)^{2/3} R'(\delta, d). \quad (3.16)$$

Here, $R'(\delta, d)$ is the radius of a sphere with the volume $V' = (4/3)\pi R'^3(\delta, d)$ equal to the sum of the initial volume of undeformed cluster ($V = (4/3)\pi R^3$) and the volume V_d of the truncated part upon deformation:

$$V' = V + V_d, \quad (3.17)$$

$$V_d = \pi \frac{R'^2_a d^2}{R'_c} \left(1 - \frac{d}{3R'_c}\right). \quad (3.18)$$

Using these relations, it is possible to determine the radius $R'(\Delta, d)$ of a sphere entering into Eqs. 3.16 for the given parameters δ and d by solving the following cubic equation:

$$R'(\delta, d)^3 + pR'(\delta, d) + q = 0, \quad (3.19)$$

where

$$p = -\frac{3}{4} \left(\frac{2-\delta}{2+\delta}\right)^{4/3} d^2, \quad q = \frac{1}{4} \left(\frac{2-\delta}{2+\delta}\right)^2 d^3 - R^3. \quad (3.20)$$

In order to solve Eq. (3.19), it is convenient to use the Cardano formula [86], which yields

$$R'(\delta, d) = \sqrt[3]{-\frac{q}{2} - \sqrt{\left(\frac{p}{3}\right)^3 + \left(\frac{q}{2}\right)^2}} + \sqrt[3]{-\frac{q}{2} + \sqrt{\left(\frac{p}{3}\right)^3 + \left(\frac{q}{2}\right)^2}} \quad (3.21)$$

$$R'(\delta, d) = \left(\sqrt[3]{-\frac{q}{2} + \sqrt{\left(\frac{p}{3}\right)^3 + \left(\frac{q}{2}\right)^2}} - \sqrt[3]{-\frac{q}{2} - \sqrt{\left(\frac{p}{3}\right)^3 + \left(\frac{q}{2}\right)^2}} \right) \frac{(1 \pm i\sqrt{3})}{2} \quad (3.22)$$

Equation 3.19 always has at least one real positive root. The region of physically admissible d values is restricted by the condition $2R'_c - d \geq 2r_s$. The limiting case of $2R'_c - d = 2r_s$ corresponds to the maximum deformation at which atoms in the cluster form two dimensional structure on the solid surface. In the case of $\delta = 0$

and $d = 0$, the radius $R'(\delta, d)$ of a deformed cluster is equal to the radius R of the undeformed sphere.

Within the framework of the droplet model, the total energy of a deformed cluster on the surface of a solid is determined according to the following formula:

$$E = E^{LDM} + E_{int} = \lambda'_V V + \lambda'_S S' + \lambda'_R \int_{S'} H' dS' + \Sigma_i \lambda_{int_i} N_i, \quad (3.23)$$

where V and S' are the volume and the surface area of the deformed cluster, respectively, and H' is the average curvature at a point on the cluster surface [86,87]. For the parametrization of the cluster shape in terms of a truncated ellipsoid of revolution, the total energy of the cluster on the solid surface depends on two parameters, δ and d . Since the main condition of deformation is the constancy of the cluster volume (which must be the same before and after deformation), a term describing the volume energy contribution remains unchanged: $E_V = N = const$.

In order to determine the surface energy of a deformed cluster, it is necessary to calculate its surface area S' . This value can be determined as a sum of areas of the upper part (S_1) of the truncated ellipsoid of revolution and the contact interface (S_2) between the cluster and the solid surface (Fig. 3.9):

$$S' = S_1 + S_2. \quad (3.24)$$

In this case, the surface energy E_S also depends on the parameters δ and d . The area S_1 of the upper part of the truncated oblate ellipsoid of revolution can be expressed as follows [86]:

$$S_1 = \frac{2\pi R'_a}{\sqrt{2}} \int_0^{\theta_1} \sqrt{R_a'^2 + R_c'^2 + (R_a'^2 - R_c'^2) \cos 2\theta} \sin \theta d\theta, \quad (3.25)$$

where angle θ_1 depends on the height d of the truncated part as

$$\theta_1 = \arccos \frac{R'_c(d - R'_c)}{\sqrt{R_a'^2(2R'_c d - d^2) + R_c'^2(d - R'_c)^2}}. \quad (3.26)$$

The area S_2 of the contact interface between the cluster and the solid surface is given by the following formula:

$$S_2 = \pi \frac{R_a'^2}{R_c'^2} d(2R'_c - d). \quad (3.27)$$

Note that the energy densities (per unit surface area) on the cluster-vacuum and cluster-substrate interfaces must be different. This difference is precisely the manifestation of cluster - solid interaction. In Eqs. (3.7) and (3.23), this interaction

is represented as the separate term E_{int} , and the total energy of the system is defined as the total energy of noninteracting subsystems plus the interaction energy. Therefore, the second term in Eq. (3.23) represents the surface energy of the free cluster.

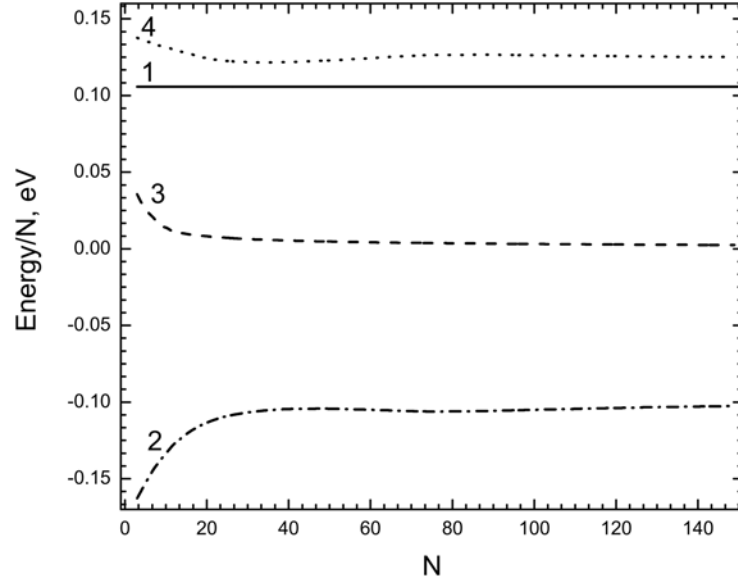


Figure 3.10: Contributions of various components to the binding energy (per atom) calculated for deformed Ar clusters of optimum shape on the graphite surface: (1) volume energy E_V/N ; (2) surface energy E_S/N ; (3) surface curvature energy E_R/N ; (4) cluster-solid interaction energy E_{int}/N .

A change in the cluster energy as a result of deformation is determined by a change in the geometric characteristics (surface area and curvature) and by the volume of the interacting part, while being independent of the choice of parameters ϵ_V , ϵ_S , and ϵ_R . Therefore, the surface energy contribution is as follows:

$$E_S(\delta, d) = \lambda_S \frac{(S_1 + S_2)}{4\pi r_s^2}. \quad (3.28)$$

In the limiting case of $\delta = 0$ and $d = 0$, we obtain $E_S(0, 0) = \lambda^{(l)} N^{2/3}$, which corresponds to the surface energy of an undeformed cluster.

The contribution to the cluster energy due to the surface curvature is determined by the average curvature H' of the surface of an ellipsoid of revolution [86]:

$$H' = \frac{R'_c [3R'_a{}^2 + R'_c{}^2 + (R'_a{}^2 - R'_c{}^2) \cos(2\theta)]}{\sqrt{2R'_a [R'_a{}^2 + R'_c{}^2 + (R'_a{}^2 - R'_c{}^2)]^{3/2}}}, \quad (3.29)$$

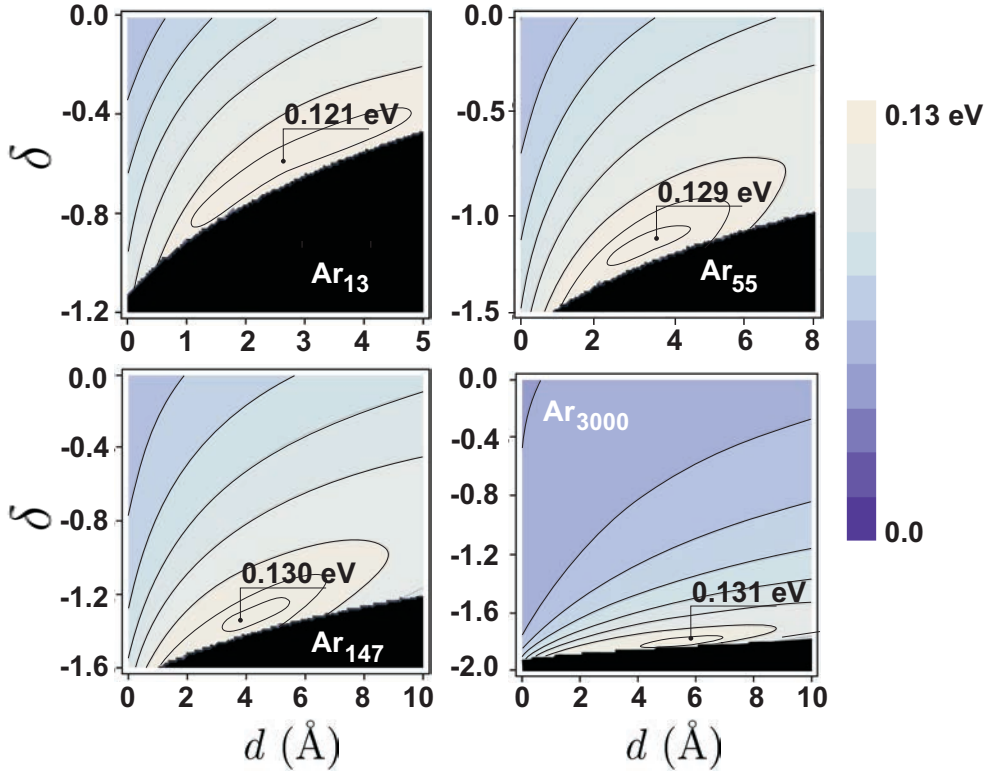


Figure 3.11: Maps of the binding energy E_b/N on the parameters δ and d for Ar_{13} , Ar_{55} , Ar_{147} , and Ar_{3000} clusters on a (001) graphite surface. Points indicate the positions of the maximum binding energy.

where angle θ can vary within $[0, \theta_1]$. The contribution due the curvature is calculated as

$$E_R(\delta, d) = \frac{\lambda_R}{4\pi r_s} \int_{S_1} H' dS_1. \quad (3.30)$$

In the limiting case of $\delta = 0$ and $d = 0$, we obtain $E_R(0, 0) = N^{1/3}$.

Figure 3.10 shows variation of the contributions of various components to the binding energy per atom as calculated as a function of the cluster size N within the framework of the droplet model for the deformed clusters of optimum shapes on the surface of a solid. As can be seen, the cluster - solid interaction energy E_{int}/N significantly contributes to the total energy of the system. In order to increase the interaction energy, it is energetically favorable for the cluster to deform so as to increase the volume of a part involved in the effective interaction with the solid. On the other hand, the deformation leads to an increase in the cluster surface area and, hence, in the contribution due to the surface energy, which leads to a decrease in the

binding energy. Therefore, the system exhibits a competition of two contributions related to the interaction energy and the surface energy. By varying the values of parameters δ and d , it is possible to find the optimum shape of a cluster on the solid surface.

Figure 3.11 illustrates the dependence of the normalized binding energy E_b/N on the parameters δ and d for Ar_{19} , Ar_{55} , Ar_{147} , and Ar_{3000} clusters on a (001) graphite surface. The black area in the bottom part of these maps corresponds to a region of physically inaccessible values of parameters δ and d , which do not obey the condition $2R' - d \geq 2r_s$. As can be seen from Fig. 3.11, the binding energy E_b/N as function of both parameters for all clusters has a single minimum, which corresponds to the most stable state of a cluster with the optimum shape. The optimum shape corresponds to the complete spreading of a cluster over the surface (perfect wetting).

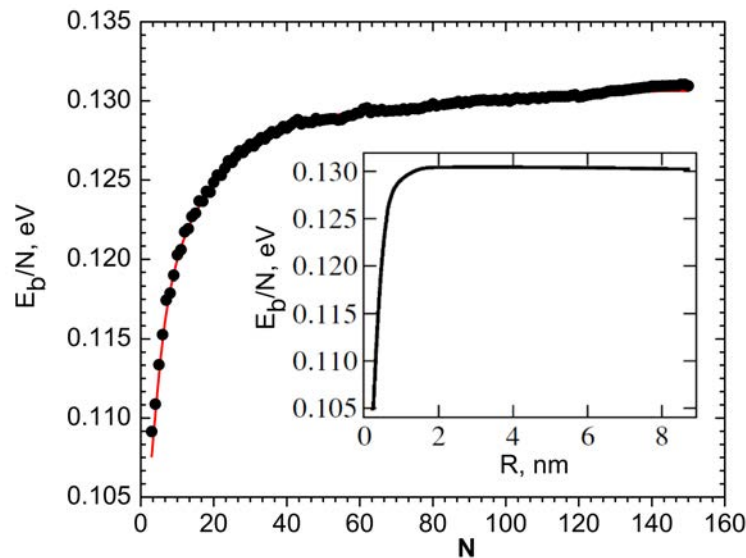


Figure 3.12: A plot of the normalized binding energy E_b/N for argon clusters on the graphite surface. Solid curve shows the results of calculations using the droplet model with allowance for the deformation of clusters; points present the results of numerical calculations employing the CFA. The inset shows a plot of the binding energy versus cluster radius calculated within the framework of the droplet model for deformed Ar clusters on the graphite surface.

The dependence of the normalized binding energy E_b/N on the number of particles N in a deformed cluster are shown in Fig. 3.12. As can be seen from Fig. 3.12, the E_b/N value monotonically increases with the cluster size N (solid curve). This

behavior shows evidence for the absence of instability with respect to fission for clusters on the solid surface and confirms the important role of deformation as a factor determining the cluster shape. Results obtained within the framework of the droplet model (solid curve) agree well with the results of numerical calculations employing the CFA, which takes into account the exact positions of atoms in the system (points). Within the framework of the CFA, the growth of clusters on the solid surface was modeled by sequentially adding particles to the system. The structures with maximum binding energy and some model and those obtained by CFA is evidence for the applicability of the proposed droplet model to descriptions of the optimum geometry and stability of clusters on the surface of solids. Small local maxima in the E_b/N versus N curve calculated by the CFA for Ar clusters on the graphite surface correspond to the most stable structures possessing closed geometric shells. The inset in Fig. 3.12 shows a plot of E_b/N versus cluster radius R (see formula 3.15) up to $R = 8$ nm for deformed Ar clusters on the graphite surface. The behavior of this curve confirms the absence of instability with respect to fission for deformed clusters on the solid surface.

3.1.3 Liquid drop model for a silver cluster on a graphite surface

In this section, the droplet model is used to describe structure deformation and energetics of a silver cluster on a solid graphite surface.

In this study interactions in the system were modeled with the potentials known from the literature. The structure and energy characteristics of the silver cluster are studied by using Sutton-Chen potential [50]. Parameters of the Sutton-Chen potential (see section 2.3.1) ϵ , a , c , m and n for silver are defined as follows: $\epsilon = 1.88 \times 10^{-3}$ eV, $a = 4.04$ Å, $c = 144.36$, $m = 6$ and $n = 12$ [51]. Note that these parameters differ slightly from the original values in [50], which were suggested to describe the interaction between silver atoms in the bulk. Using parameters were taken from [51], and were developed to account for the finite size of the interacting particles.

The interaction between Ag and C atoms is described by Morse pairwise potential (see section 2.2.2). In the present study were considered two sets of Morse parameters. First set was defined in [90] by using mixing rules. According to [90], parameters for the silver-carbon interaction can be written as $\epsilon^{Ag-C} = 0.29$ eV,

$r_0^{Ag-C} = 2.35 \text{ \AA}$, $\beta^{Ag-C} = 2.66 \text{ \AA}^{-1}$, $n^{Ag-C} = 3.46$. The second set of parameters is differed from the original set by the value of ϵ^{Ag-C} parameter, which is equaled to 0.02 eV. Parameter ϵ^{Ag-C} was varied to show, that a cluster structure on a surface strongly depend on the cluster - solid interactions.

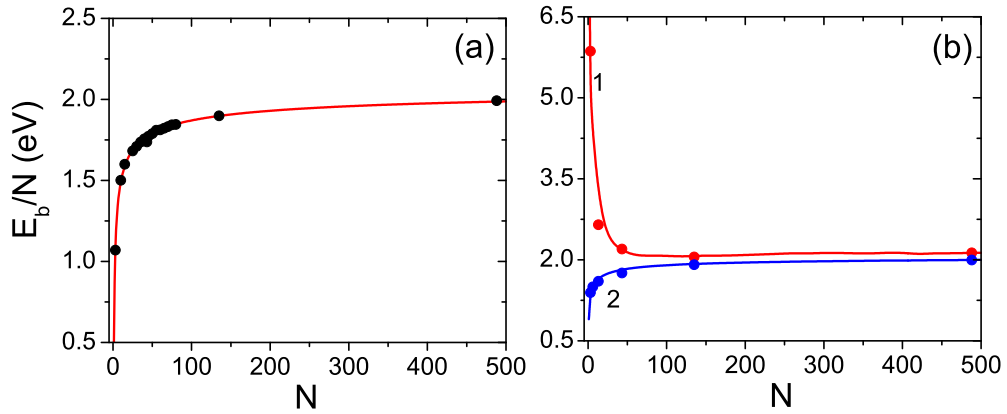


Figure 3.13: Binding energy E_b/N (normalized to the total number N of particles) as function of the cluster size N . (a) Binding energy E_b/N calculated for free Ag cluster: points present the result of numerical calculation from [91]; solid curve shows the results of calculations using the droplet model. (b) Binding energy E_b/N calculated for undeformed Ag clusters on the graphite surface with the MD method (points) and the droplet model (solid curve). The interaction between cluster and surface was modeled via Morse potential. Curve (1) and set of points (1) correspond to the situation, when the parameter ϵ^{Ag-C} for the Morse potential is equal to 0.29 eV; curve (2) and set of points (2) correspond to the situation, when $\epsilon^{Ag-C} = 0.02$ eV

The structure and energy characteristics of most stable free silver clusters have been studied in much detail in work [91]. In Fig. 3.13a, points show a plot of the binding energy E_b (normalized to the number of particles) for free cluster of silver defined according to Eq. (3.1). The plot of E_b/N in Fig. 3.13a was constructed from numerical calculations performed in work [91]. The binding energy of a free cluster of silver can be calculated with the droplet model. According this model, the cluster represents an incompressible drop of spherical shape. The total energy of a free cluster within the framework of the droplet model can be represented as the sum of contributions due to the volume energy (E_V), surface energy (E_S), and curvature energy (E_R). According to the expressions (3.3) - (3.5), the total energy of a free cluster of the spherical shape can be written as (see section 3.1.1):

$$E_{sphere}^{LDM} = \lambda'_V N + \lambda'_S N^{2/3} + \lambda'_R N^{1/3}. \quad (3.31)$$

The values of parameters λ'_V , λ'_S , and λ'_R can be refined by fitting to the total energy calculated with allowance for the exact positions of atoms in the system [75,80]. Figure 3.13a (solid curve) shows the binding energy per particle, which was calculated as a function of their number N within the framework of the droplet model with the following coefficients: $\lambda'_V = -2.14$ eV, $\lambda'_S = +1.10$ eV, and $\lambda'_R = +0.62$ eV. As can be seen from Fig. 3.31, the droplet model is capable of describing the binding energy of a free silver cluster with the quite high accuracy.

Let us to consider a spherical cluster on a solid surface, the total energy of the system is the sum of the energy of free cluster (E_{sphere}^{LDM}), and the energy of interaction (E_{int}) between the cluster and the solid. In present study the energy of a solid E_{bulk} is excluded from the consideration. It is possible to exclude the energy of the solid from the consideration, because the solid deformations are ignored. Subdividing a cluster interacting with a solid surface into n elementary layers parallel to the surface, the cluster - solid interaction energy can approximately represent by a finite sum

$$E_{int} \approx \sum_{i=1}^n \lambda_i V_i, \quad (3.32)$$

where V is the total cluster volume, V_i is the volume of the i th layer, $\sum_{i=1}^n V_i = V$, and λ_i are coefficients dependent on the distance from the i th layer to the solid surface. These coefficients were determined for the silver - graphite interaction by fitting to the energy of interaction of the undeformed cluster calculated using the molecular dynamics technique. Figure 3.13b (points) shows the results of calculations of the binding energy per atom with the molecular dynamics method for Ag_3 , Ag_6 , Ag_{13} , Ag_{43} , Ag_{135} and Ag_{488} clusters interacting with the graphite surface. Set of points (1) corresponds to situations, when the interaction energy between cluster and surface are modeled via Morse potential with the parameter $\epsilon^{Ag-C} = 0.29$ eV. Set of points (2) shows the results of simulations performed with the same potential, but with the ϵ^{Ag-C} is equal to 0.02 eV. The solid curves (1) and (2) represent the results of calculations performed in framework of the droplet model for the spherical cluster on a surface, for different interactions between cluster and solid. As can be seen, the binding energy for the strong interaction of a spherical cluster with a surface, see curve (1) in Fig. 3.13b, first rapidly decreases with increasing number N and then slowly increases with the further growth in N . That behavior of the

total binding energy with increasing N observed for underformed Ag clusters shows evidence for the instability of cluster on the solid surface with respect to fission and/or deformation. In other case, when the interaction between cluster and surface is weak (see curve (2) in Fig. 3.13b), the binding energy almost monotonically increases with the number of particles N . This observation shows that clusters are stable on a surface, but the deformation of a cluster is a possible process. The deformation leads to an increase in the volume of the part of the cluster, which is involved in the interaction with the surface, it results in an increase in the binding energy of the system.

In order to take into account the deformation of a cluster interacting with the surface of a solid, the shape of the deformed cluster was parameterized by a model of a truncated ellipsoid of revolution (see section 3.1.2). The total energy of the deformed cluster on the solid surface in such parametrization depends on two parameters, δ and d . Parameter δ is the deformation parameter and d is the height of the truncated part of a truncated ellipsoid of revolution. In section 3.1.2, the relationship of the volume energy (E_V), surface energy (E_S), curvature energy (E_R) with the parameters of parametrization d , δ was established and discussed in greater details. As was shown in section 3.1.2, it is possible to find the optimum shape of a cluster on a solid surface, by varying the values of parameters δ and d .

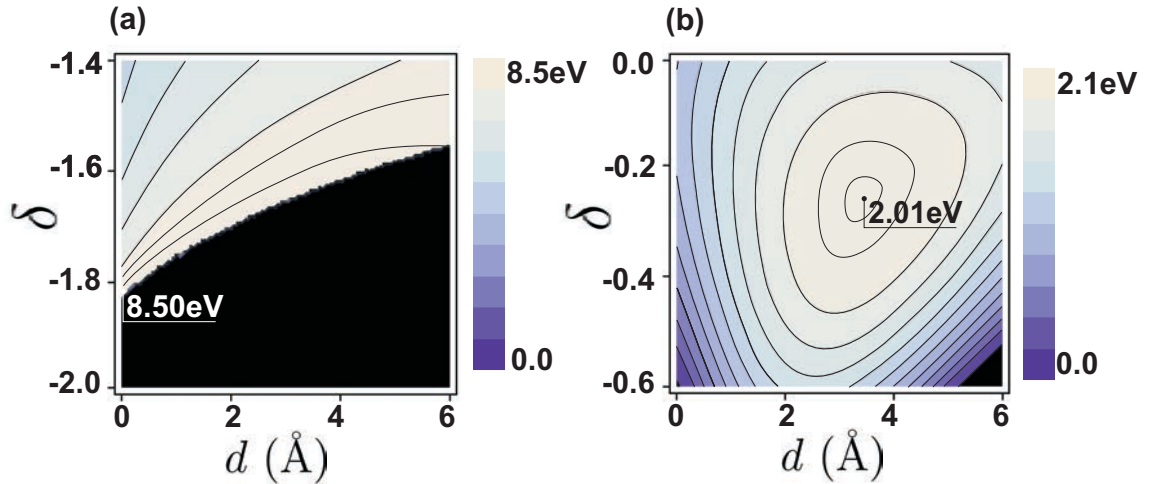


Figure 3.14: Maps of the binding energy E_b/N on the parameters δ and d for Ag_{500} on a graphite surface calculated for different cluster - solid interactions. (a) Strong cluster - solid interaction $\epsilon^{Ag-C} = 0.29$ eV; (b) weak cluster - solid interaction $\epsilon^{Ag-C} = 0.02$ eV. Points indicate the position of the maximum binding energy.

Figure 3.14 illustrates the dependence of the normalized binding energy E_b/N on the parameters δ and d for Ag_{500} cluster on a graphite surface. As can be seen, in case of strong cluster - solid interaction (see Fig. 3.14a) the cluster Ag_{500} becomes flatten, parameter of deformation δ is equal to -1.82 and the height of the truncated part d is 3.11×10^{-8} Å. The values of semiaxes R'_a and R'_c of a truncated ellipsoid of revolution can be defined with the equations (3.16), and for Ag_{500} on a graphite surface are equaled to 28.67 Å and 1.35 Å, correspondingly. The hight of a cluster Ag_{500} after deformation in this case is 2.70 Å, this value corresponds to the hight of a silver monolayer. In case of weak cluster-solid interaction (see Fig. 3.14a) cluster Ag_{500} consist on several atomic monolayers, the hight of the cluster after deformation is 14.41 Å, this value corresponds to $\delta = -0.27$ and $d = 3.47$ Å. It is shown, that droplet model can be used to predict the structure of a cluster depending on the interaction between cluster and solid.

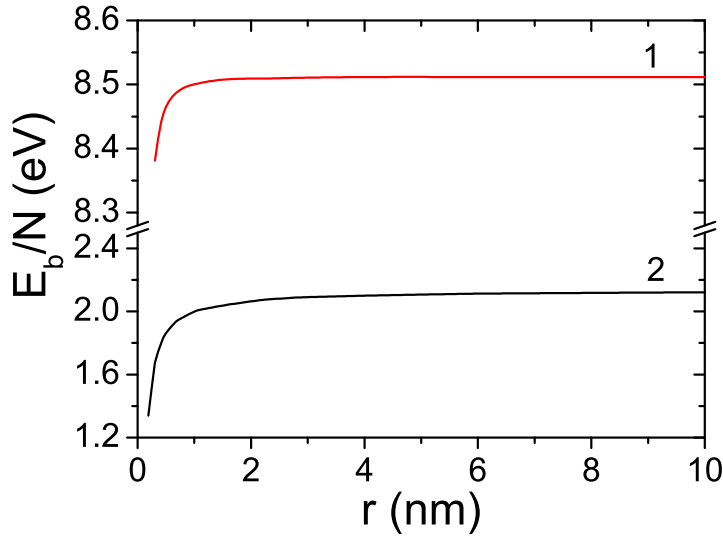


Figure 3.15: A plot of the normalized binding energy E_b/N for silver cluster on the graphite surface calculated with the droplet model for different cluster-solid interactions. Curve (1) and (2) calculated for different interactions between cluster and solid: (1) weak cluster-solid interaction $\epsilon^{Ag-C} = 0.29$ eV; (2) strong cluster-solid interaction $\epsilon^{Ag-C} = 0.02$ eV.

In Fig. 3.15 shows the dependence of the normalized binding energy E_b/N on the cluster radius R (see formula (3.15)) up to 10 nm for deformed Ag clusters on the graphite surface. As can be seen from Fig. 3.15, the E_b/N value monotonically

increases with the cluster size. This behavior shows evidence for the absence of instability with respect to fission for clusters on the solid surface and confirms the important role of deformation as a factor determining the cluster shape.

3.2 Cluster diffusion over a surface

Morphology of a pattern on a surface strongly depends on the mobility of deposited nanoparticles [18,19,70]. It has been demonstrated experimentally that many metallic clusters diffuse on graphite surface at a high rate of about 10^{-8} cm²/s at room temperature [15,19], which is comparable to the rates of a single atom. This was also demonstrated theoretically for the Lennard-Jones clusters on a Lennard-Jones substrates with the molecular-dynamics simulations [6]. In work [6] was shown, that a cluster diffuses as "a whole", and its trajectory of the motion is similar to a Brownian motion. Similar results were obtained using MD with more elaborated potentials models, for example in [92] diffusion of 249-atom gold cluster was theoretically studied. In work of P. Deltour and co-workers [92] was shown that the diffusion mechanisms for the large clusters cannot be explained in terms of dislocation migration within the cluster as proposed to explain the diffusion of 2D islands in [93–95]. The surprising high diffusivity of a large cluster was ascribed with the the interplay between the vibrations of the substrate and the internal vibrations of the cluster. These two vibrations create a "random" force on the cluster center of mass, and execute a Brownian motion in weak external potential [6,71,92].

In present chapter MD technique is employed to study structure and dynamics of silver nanoclusters deposited on a graphite surface. The diffusion coefficient of the silver nanoclusters is analyzed depending on the particle size, temperature and cluster-surface interactions.

3.2.1 Diffusion coefficient

Diffusion is the process by which matter is transported from one part of the system to another. To describe diffusion on a surface is possible to adapt the procedures developed for bulk diffusion [96]. The flux J crossing a line of unit length is given by Fick's first law

$$J = -D \frac{\partial C}{\partial x} \quad (3.33)$$

where $\partial C/\partial x$ is the gradient of the concentration C , and D is called the diffusion coefficient. In practice is difficult to measure the flux J . Let us to transform equation 3.33, for it consider two parallel lines on a surface, distance between two lines Δx is equal to the particle jump length l executed in diffusion. The flux into lines is not equal, because diffusing substance accumulate in the region between the two lines. If the flux is considered per unit length, the

$$J_1 - J_2 = \Delta x \frac{\partial J}{\partial x} = \Delta x \frac{\partial C}{\partial t}. \quad (3.34)$$

However, from Eq. (3.33) is known that

$$\frac{\partial J}{\partial x} = -\frac{\partial(D\frac{\partial C}{\partial x})}{\partial x}. \quad (3.35)$$

If the diffusion coefficient will not be a function of diffusing particles concentration than

$$\frac{\partial C}{\partial t} = -D \frac{\partial^2 C}{\partial x^2}. \quad (3.36)$$

Eq. (3.36) is the second Fick's law, that equation can more directly applicable to examining surface diffusion. In the present chapter the diffusion of a single atomic cluster over crystal surface is discussed, in this case the diffusion coefficient D is not a function of the clusters concentration. Note, that the Eqs. (3.33)-(3.36) are written only for one-dimensional diffusion, with the flux as well as the gradient along x -axis. Eq. (3.36) for the the general case can be written as

$$\frac{\partial C(r, t)}{\partial t} = -D \nabla^2 C(r, t), \quad (3.37)$$

In case of the two-dimensions solution of the Eq. (3.37) is

$$C(r, t) = \frac{1}{4\pi Dt} \exp\left(\frac{-r^2}{4Dt}\right), \quad (3.38)$$

That solution gives the probability to find a particle at the instant t being at the distance $[r, r + dr]$ from its initial position as

$$\omega(r, t)dr = c(r, t)dS, \quad (3.39)$$

where $dS = \int_0^{2\pi} r dr d\varphi = 2\pi r dr$ therefore

$$\omega(r, t)dr = \frac{1}{2Dt} \exp\left(-\frac{r^2}{4Dt}\right) r dr. \quad (3.40)$$

Using this probability function one derives the mean square displacement of a particle as [97, 98]

$$\overline{(r_1 - r_0)^2} = \int_0^\infty \omega(r, t) r^2 dr = 4D(t_1 - t_2), \quad (3.41)$$

where r_0 and r_1 are the distances to a particle from the initial position at two successive instances t_0 and t_1 . Equation (3.41) allows to express the diffusion coefficient as

$$D = \frac{\langle \Delta r^2 \rangle}{2z \Delta t}, \quad (3.42)$$

where $\langle \Delta r^2 \rangle$ is the mean-square displacement of a particle per time Δt , and z is defined by the dimensionality of space [97, 98]. In the case of particle diffusion on surface $z = 2$ (see Eq. (3.41)).

In other hand, let us to interpret the diffusion coefficient in terms of the particle jump process. The mean-square displacement proportional to the rate of particle jumps Γ and the size of the particle hopping length

$$\langle \Delta r^2 \rangle = \Gamma \ell_0^2 \Delta t, \quad (3.43)$$

Substituting Eq. (3.43) into Eq. (3.42), one obtains

$$D = \frac{\Gamma \ell_0^2}{2z}. \quad (3.44)$$

The jump rate of a particle can written with the expression available from transition state theory for the rate of overcoming a potential barrier height E_a [7, 97, 98],

$$\Gamma = \nu \exp\left(-\frac{E_a}{k_B T}\right), \quad (3.45)$$

where ν is the attempt frequency, k_B is the Boltzmann constant and T is the temperature. Therefore, diffusion coefficient D can be written as

$$D = \frac{\nu \ell^2}{2z} \exp\left(-\frac{E_a}{k_B T}\right). \quad (3.46)$$

That equation demonstrates the relation between the diffusion coefficient and system temperature.

3.2.2 Silver cluster diffusion over graphite surface: simulations versus experiment

In this work, the diffusion of silver clusters Ag_{43} , Ag_{135} and Ag_{488} on a graphite surface was modeled with the classical molecular dynamics technique. The initial shape of the clusters was approximate spherical. The initial distance between the nanocluster and graphite is set to 0.2 nm. The size of the graphite structure depends on the cluster diameter, the width and length of the graphite sheet were taken in 10 times larger of the diameter of a cluster. In the work, the constant-temperature molecular dynamic simulations with a time step of $\Delta t = 1$ fs were performed. The simulation time was 1 ns for the equilibration and 9 ns for the production state. The temperature control was achieved by means Berendsen thermostat with the damping constant 100 fs [44].

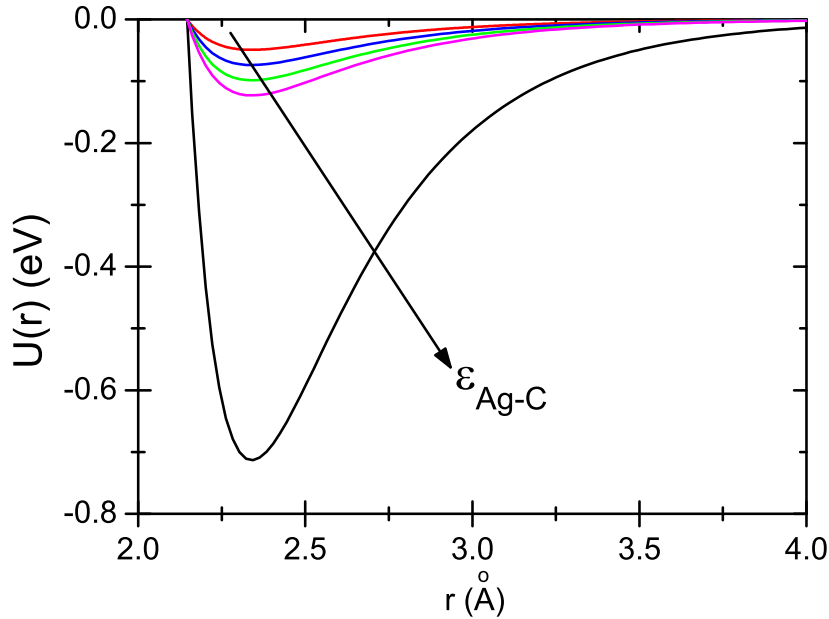


Figure 3.16: The form of the pairwise Morse potential for the silver and carbon atoms, as function of the distance between atoms for different values of the parameter $\epsilon^{Ag-C} = (0.02, 0.03, 0.04, 0.05, 0.29)$ eV. The direction of growth of the parameters ϵ^{Ag-C} is shown in the plot.

The interactions between the atoms are described by using model potentials known from the literature. The total potential energy of the system can be written

as

$$U = U_{Ag-Ag} + U_{C-C} + U_{Ag-C} \quad (3.47)$$

where the terms U_{Ag-Ag} , U_{C-C} and U_{Ag-C} refer to the silver-silver, carbon-carbon and silver-carbon interaction respectively. To reduce the computation costs, in the present work only a static (solid) substrate was considered, that corresponds to the situation when the position of the C atoms are fixed.

The molecular dynamics study of the Ag clusters has been performed using the Sutton-Chen many-body potential [50] (see also section 3.1.3). The most crucial potential for the system which consists of a metal nanoparticle and graphite surface is the potential representing metal-carbon interactions. The interaction between the metal cluster and graphite surface is mainly dominated by a weak van der Waals force. In the present work, the interaction between Ag and C atoms is modeled by Morse pairwise potential (see section 2.2.2). Parameters of the Morse potential can be determined by fitting the metal-carbon interaction obtained by using *ab initio* density functional theory, as was done in work A.G. Lyalin and co-workers [99] for the $Ni-C$ interactions. In other hand, parameters of the interaction can be obtained by using mixing rules, which are described in [90]. According to [90], parameters for the silver-carbon interaction can be written as $\epsilon^{Ag-C} = 0.297172$ eV, $r_0^{Ag-C} = 2.3495$ Å, $\beta^{Ag-C} = 2.6617$ Å⁻¹, $n^{Ag-C} = 3.4641$. Parameter ϵ and parameter n in Morse potential defines the energy of the potential in its minimum r_0 as $\epsilon(n-1)$. According to this relation the binding energy between the Ag and C is equal to 0.732262 eV. The structure of the cluster and the diffusion mechanism strongly depend on the cluster-surface interaction. In the present work, the influence of the binding energy between silver and carbon on the dynamics of silver nanoparticle on graphite surface was studied by varying parameter ϵ^{Ag-C} in Morse potential. The forms of the Morse potential for different value of the parameter ϵ^{Ag-C} are shown in Fig. 3.16.

The computations in the present work were performed with the use of the **MBN Explorer** computer package, which is developed for structure optimization, simulation of dynamics and growth processes in various nanosystems [100].

In the present work, the trajectories of the deposited on a graphite surface silver nanoparticles depending on the systems size, temperature and parameter ϵ^{Ag-C} are analyzed. The diffusion coefficient of center of mass of a nanoparticle is defined as [97, 98]:

$$D = \frac{1}{4} \frac{\partial \langle r^2(t) \rangle}{\partial t} \quad (3.48)$$

where $r^2(t)$ is the mean square displacement of the center mass of a nanoparticle on a surface as function of time.

$$\langle r^2(t) \rangle = \frac{1}{n_t} \sum_{i=1}^{n_t} [R(t_{0i} + t) - R(t_{0i})] \quad (3.49)$$

Here $R(t)$ is the radius vector of the particle center of mass at the instant t . This equation assumes the splitting of the trajectory of a particle in n_t segments of equal duration. This is done in order to improve the statistics when evaluating the mean square displacement.

Cluster-surface interaction influence on the shape of a nanoparticle

The shape of a cluster on a surface strongly depends on the interaction between cluster and solid, it was demonstrated in framework of liquid drop model (see section 3.1.3). In the present chapter the shape evolution of the silver cluster on a graphite surface is modeled with the molecular dynamics approach.

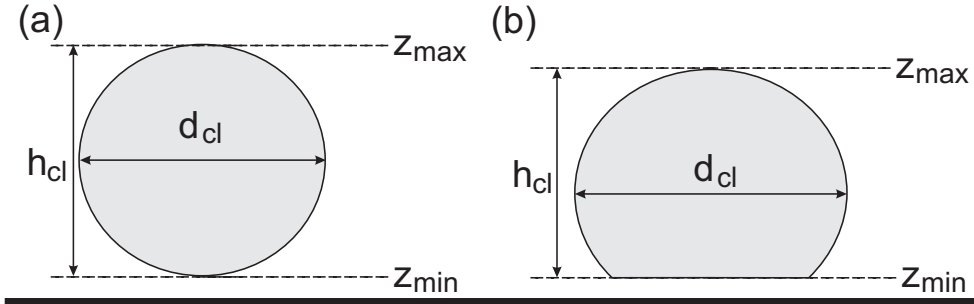


Figure 3.17: Schematic diagram of a cluster on a solid surface: (a) undeformed spherical cluster; (b) cluster with allowance for deformation in the form of a truncated oblate ellipsoid. z_{max} , z_{min} are the distances between the solid surface and the minimally and maximally disposed points of the cluster, correspondingly. h_{cl} and d_{cl} are the height and width of the cluster.

The schematic diagram of underformed and deformed clusters on the solid surface are shown in Fig. 3.17. The height of the cluster h_{cl} on a surface is calculated as

$$h_{cl} = z_{max} - z_{min}, \quad (3.50)$$

where z_{max} and z_{min} are the distances between the surface of substrate and the minimally and maximally disposed points of the cluster, correspondingly. The width of the cluster d_{cl} is the maximal diameter of the cluster in the plane which is parallel to the surface of the solid (see Fig. 3.17).

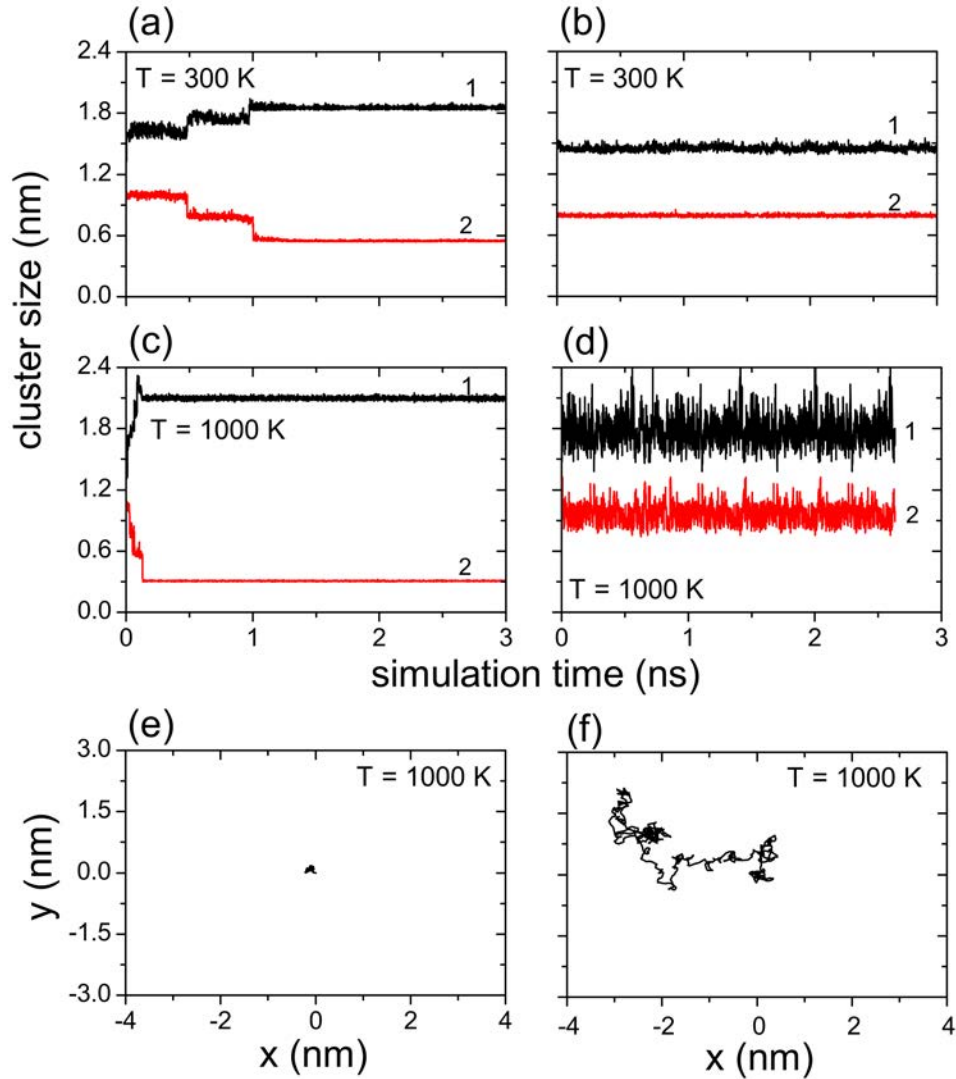


Figure 3.18: The shape evolution of the cluster Ag_{43} on a graphite surface. Time evolution of the width d_{cl} and height h_{cl} of a cluster calculated for $\epsilon^{Ag-C} = 0.29$ eV (a), (c) and for $\epsilon^{Ag-C} = 0.03$ eV (b), (d). Trajectories of center of mass of Ag_{43} cluster on the graphite surface calculated for $\epsilon^{Ag-C} = 0.29$ eV (e), and for $\epsilon^{Ag-C} = 0.03$ eV (f). The corresponding simulating temperature of the system is given in the insets to the plot.

In figure 3.18, the time evolution of the height h_{cl} and width d_{cl} of Ag_{43} cluster

on a graphite depending on the interaction between cluster and solid are presented. In case of the strong interaction between cluster and solid ($\epsilon^{Ag-C} = 0.29$ eV), the height h_{cl} of the cluster decrease in course of simulation, at some point the value of h_{cl} becomes constant and equals to the diameter of a single silver atom (see Fig. 3.18a,c). Atoms of the Ag_{43} cluster are formed a monolayer on the surface. As can be seen from the figure 3.18a,c the speed of the shape transformation of the cluster depends on the system temperature. At room temperature $T = 300$ K the time of the cluster melting is 1.0 ns, at high temperature $T = 1000$ K the time of the cluster “melting“ is 0.16 ns. In opposite case, when the interaction between cluster and solid is weak ($\epsilon^{Ag-C} = 0.03$ eV), the height of a cluster h_{ch} after cluster transformation is 0.84 nm at room temperature, at the high temperature 1000 K the large fluctuations in $h_{cl}(t)$ and $d_{cl}(t)$ dependencies are observed, the height of a cluster is varied between 0.8 and 1.11 nm (see Fig. 3.18b,d). This transformation of a cluster shape depending on the cluster-surface interaction stays in good agreement with the results, which are obtained in framework of the liquid drop model (see section 3.1.3). LDM predicts the transformation of the cluster to monolayer for $\epsilon^{Ag-C} = 0.29$ eV.

Trajectories of the Ag_{43} center of mass are shown in figure 3.18e,f. The diffusion of the cluster Ag_{43} is observed at the temperature 1000 K, when the value of the parameter ϵ^{Ag-C} is equal to 0.03 eV.

Temperature effect on the diffusion of a nanoparticle over a surface

The diffusion coefficient of a nanoparticle on a surface can be experimentally measured. For example, the diffusion coefficient of the cluster Ag_{500} on graphite surface at room temperature was measured as $2 \cdot 10^{-7}$ cm²/s [19]. Therefore, it is possible to compare the experimentally measured values of the diffusion coefficients with the results of the theoretical calculation. In the present work, the diffusion coefficients of Ag_{135} and Ag_{488} on a graphite surface was analyzed depending on the temperature and the parameter ϵ^{Ag-C} .

Diffusion coefficients of silver nanoparticles Ag_{488} and Ag_{135} on the graphite surface D are evaluated at different temperatures (400, 600, 800 and 1000 K) using the mean-square displacement as a function of time (see Eqs. 3.48-3.49). These results are given in Table 3.1 and shown in Fig. 3.19. Points in Fig. 3.19 represent results of the MD simulations. In Fig. 3.19b the diffusion coefficient of a nanoparticle as

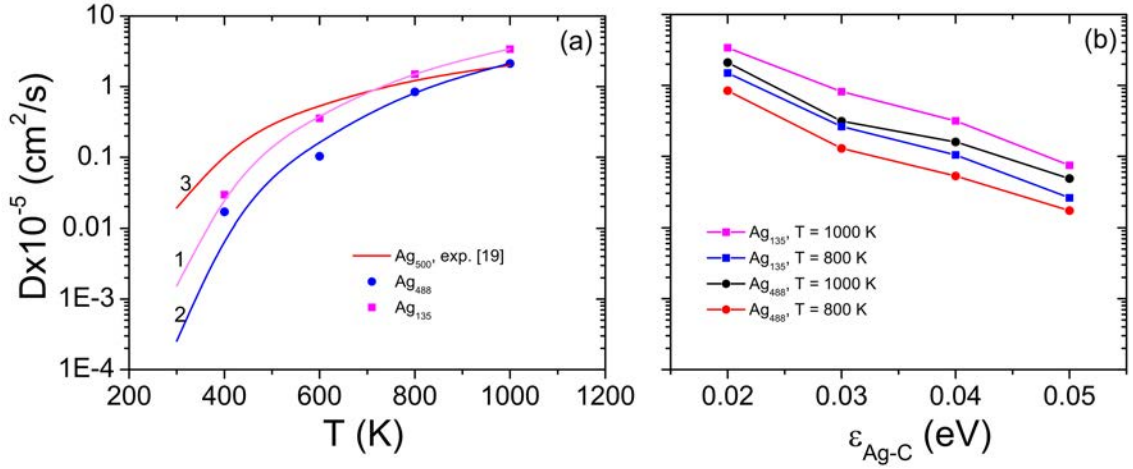


Figure 3.19: Diffusion coefficient of the silver nanoparticle on the graphite surface depending on the temperature and the value of the parameter $\epsilon^{\text{Ag-C}}$ calculated according to Eq. (3.48). (a) Diffusion coefficient of the nanoparticle as the function of a temperature. Points are shown the results of MD simulations with the parameter $\epsilon^{\text{Ag-C}} = 0.02 \text{ eV}$. The corresponding size of silver cluster are given in the insets to the plot. Lines (1) and (2) are temperature dependence of the diffusion coefficient of clusters Ag_{135} and Ag_{488} , correspondingly, calculated by fitting of MD simulation results with the equation (3.46). Line (3) is the temperature dependence of the diffusion coefficient of cluster Ag_{500} on graphite surface from [19]. (b) Diffusion coefficient of the nanoparticle as function of the parameter $\epsilon^{\text{Ag-C}}$. The corresponding simulating temperature and size of the nanoparticle are given in the insets to the plot.

a function of parameter $\epsilon^{\text{Ag-C}}$ are shown. Temperature dependence of the diffusion coefficient are presented in Fig. 3.19a. Relation between the diffusion coefficient

Table 3.1: Diffusion coefficients of the nanoparticles Ag_{135} and Ag_{488} on the graphite surface calculated according to Eq. (3.48) for different temperatures and values of the parameter $\epsilon^{\text{Ag-C}}$.

$\epsilon^{\text{Ag-C}}, \text{ eV}$	$D, \text{ cm}^2/\text{s}$							
	Ag_{135}				Ag_{488}			
	1000 K	800 K	600 K	400 K	1000 K	800 K	600 K	400 K
0.02	3.4×10^{-5}	1.5×10^{-5}	1.60×10^{-7}	3.0×10^{-7}	2.2×10^{-5}	8.4×10^{-6}	1.0×10^{-6}	1.7×10^{-7}
0.03	8.2×10^{-6}	2.6×10^{-6}	-	-	3.1×10^{-6}	1.3×10^{-6}	-	-
0.04	3.2×10^{-6}	1.0×10^{-6}	-	-	1.6×10^{-6}	5.3×10^{-7}	-	-
0.05	7.4×10^{-7}	1.6×10^{-7}	-	-	4.8×10^{-7}	1.2×10^{-7}	-	-

and system temperature is demonstrated with the Eq. (3.46) in section 3.2.1. The results of the MD simulation can be fitted with the Eq. (3.46), if the height of the potential barrier E_a and the attempt frequency ν are assumed to be fixed. The lines (1) and (2) in Fig. 3.19a show the dependence of the diffusion coefficient on the system temperature calculated by fitting results of the MD simulations. Line (3) is the function $D(T)$ calculated with the Eq. (3.46) for the fixed values of the E_a and ν experimentally measured in [19, 55]. As can be seen from Fig. 3.19a, the values of the diffusion coefficient calculated with the MD approach at high temperature has a good agreement with the values obtained with the Eq. (3.46) for the experimentally measured values of the parameters E_a and ν . At room temperature diffusion coefficient of the Ag_{488} predicted with the MD technique is equaled to 2.6×10^9 cm²/s. It is smaller than the value of the diffusion coefficient of an Ag_{500} cluster on the graphite surface (2×10^{-7} cm²/s) experimentally measured in [19]. The height of the potential energy barrier E_a for the transition of the Ag_{488} on the graphite substrate from one position to another calculated in framework of MD approach is 0.35 eV. This value about two times higher than the potential energy barrier reported in [55]. The difference between the results of the MD simulation and results of the experimental observation can be ascribed by several simplifications which were performed to reduce the computation costs.

The results presented in this section demonstrate the modeling of the diffusion process of a single nanoparticle on a surface with the molecular dynamics approach. Note that in the present work a simple velocity scaling thermostat (Berendsen thermostat, see sec. 2.1.3) is used to control temperature of a system. Scaling of the particle velocities in the system might be considered as an "unphysical" alteration of the systems dynamics. However, if the coupling of the thermostat to the system is weak (parameter "rise time" τ_T , see Eq. (2.15) in sec. 2.1.3), i.e. all the thermodynamic relations are conserved for each small fraction of the system, the overall influence of the thermostat on the dynamical properties of the cluster can be neglected. The influence of the thermostat becomes more important if the system consists of a small number of particles or if the system is not in the thermodynamic equilibrium. The molecular dynamics simulations at constant temperature imply usage of a thermostat. The thermostat adds certain constraints on the system and influence its dynamical properties. In order to avoid the undesirable influence of the thermostat on the systems dynamics it is necessary to conduct the molecular dynamics simulations with a sufficiently weak coupling of the thermostat to the sys-

tem. The molecular dynamics simulations reported in the present work are believed to be performed in the regime of the weak thermostat coupling. The accurate analysis of the influence of the thermostat on systems dynamics is not performed and the corrections to the diffusion properties of the clusters caused by the Berendsen and other thermostats are left for further considerations.

It is important to mention that the MD simulations of the clusters are performed on the static (frozen) substrate. Freezing of the degrees of freedom associated with the motion of the substrate atoms allowed to substantially reduce the number of degrees of freedom in the system and considerably extend the simulation timescales. Accounting for the substrate degrees of freedom may influence the barriers associated with the transition of the cluster on the substrate from one position to another. Change of the heights of the potential energy barriers associated with the diffusion influences the diffusion coefficient. One can assume that accounting for the substrates degrees of freedom should lower the potential energy barriers. Indeed, the transition from one stable point to another on the multidimensional potential energy surface of the system occurs along the path with lower energy barriers if one increases the number of the accessible degrees of freedom in the system. This statement is applicable only for the solid substrates in which the atoms vibrate in the vicinity of the stable positions. The substantial deformations of the substrate or its melting can have an opposite effect and lead to the increase of the transition barriers. The assumption about the rigidity of the substrate is in an agreement with experimental observations [55] that report the transition barriers about two times lower than the transition barriers calculated in the thesis. In the present work the influence of the substrate degrees of freedom on the cluster diffusion properties is not considered and left for further investigations.

Chapter 4

Kinetic model for assembly of nanoparticles on a surface

In previous chapters (see sections 2.4, 3.1.3 and 3.2) it was shown that methods of classical molecular dynamics are hardly applicable for modeling behavior of an assembly of atomic clusters on a surface. Therefore, it is important to find suitable approaches, which can be used for modeling dynamics of an assembly of nanoparticles on a surface. One of such alternative approaches is the kinetic Monte Carlo method. In this approach, the evolution of the system governs by several typical processes, which occur with certain predefined rates.

The results of molecular dynamics simulations for silver clusters on a graphite surface shown that clusters diffuse over the surface as a whole with a high rate, that stands in a good agreement with the results of experimental observations performed in the group of Prof. C. Bréchnac [9, 10, 17]. Based on these facts a Monte-Carlo based approach has been developed to describe the dynamics of the self-assembly of nanoparticles on a surface. This method accounts for the nanoparticle diffusion over a surface, aggregation into islands and detachment from these islands. This processes occur in the system with certain kinetic rates which are input into the model. The kinetic rates are material-based parameters, which in the case of nanoparticle diffusion on a surface depend on the atomic composition of nanoparticles, substrate material and interparticle interactions. The main advantage of that method is the possibility to account for different processes, which influence the system dynamics.

The main idea of the method is discussed in section 4.1. One of the possible implementations of the kinetic model, which is based on the modified version of the conventional kMC method is shown in section 4.2. The physical meaning of the

model parameters are discussed in section 4.3. The values of the model parameters are indicated for the concrete system - silver cluster on graphite surface. In appendix B, implementation of developed model in **MBN Explorer** software package and corresponding logical test are discussed in details.

4.1 Basic principles and assumptions of the kinetic model

The main idea of the kinetic model is the following. Consider a molecular system constituting of a number of rigid particles of equal radii, e.g. silver clusters deposited on graphite surface [101,102]. For each particle in the system first the number of possible diffusion directions are determined. Thereby, a particle can either diffuse freely, or diffuse along the periphery of the already pre-formed structure as illustrated for a chosen example in Fig. 4.1. A diffusion direction for a particle is chosen randomly in such a manner that all possible diffusion directions are equally probable. For the given diffusion direction the probability for particle diffusion is then calculated from the predefined physical parameters input into the system, and the particle is translated with calculated probability in the direction defined earlier.

To speed up the calculation, we simulated particle dynamics on a hexagonal grid, on which a particle has up to six neighbors in 2D case, as illustrated in Fig. 4.1. The size of a single grid cell in this case is defined by the particle diameter d_0 .

To simulate a pattern growth on a surface the following procedure has been adopted. At every step of the simulation new particles are deposited on the surface according to the deposition rate and occupy some of the free cells in the grid. Simultaneously, the already deposited particles diffuse on the surface, with the rate

$$\Gamma = \nu_1 \exp \left[-\frac{E_a}{k_B T} \right], \quad (4.1)$$

where E_a is the activation energy, ν_1 is the attempt escape rate, T is the temperature of the system and k_B is the Boltzmann constant. The process of particle diffusion on surface is schematically illustrated in Fig. 4.1.

An important quantity in the kinetic model is the time step, Δt , which defines the characteristic time for particle diffusion over a surface as

$$\Delta t = 1/\Gamma. \quad (4.2)$$

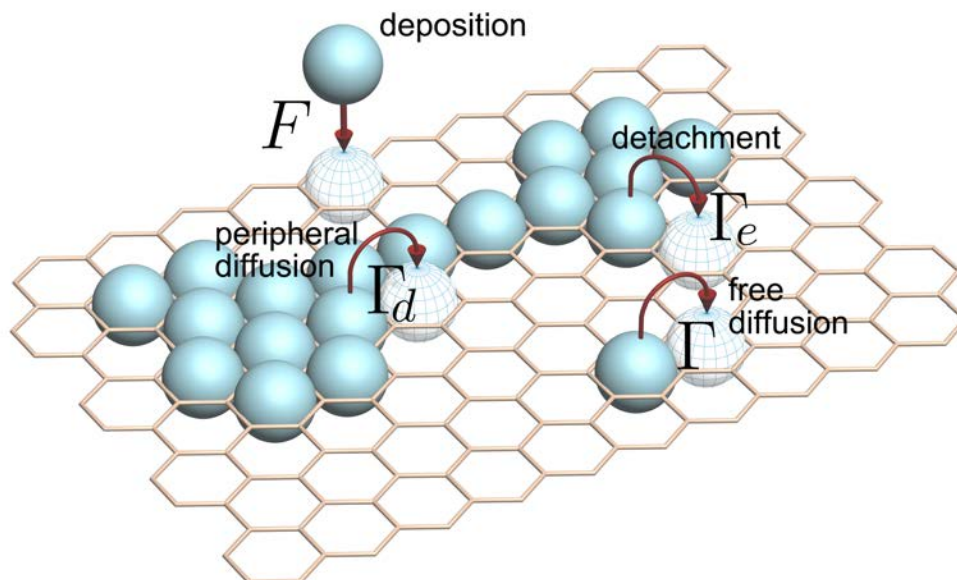


Figure 4.1: Arrangement of deposited nanoparticles on a surface. The important processes which govern pattern formation on a surface are indicated by arrows: F is the particle deposition rate, Γ is the diffusion rate of a free particle, Γ_d is the diffusion rate of a particle along the periphery of an island, and Γ_e is the detachment rate of a particle from the island.

The time step Δt is related to the diffusion coefficient D of a particle diffusion over a surface arising in the equation of diffusion [97, 98]. The solution of the diffusion equation in two dimensions gives the probability to find a particle at time t being at distance $[r, r + dr]$ from its initial position as

$$\omega(r, t)dr = \frac{1}{2Dt} \exp\left(-\frac{r^2}{4Dt}\right) r dr. \quad (4.3)$$

Using this probability function one derives the mean square displacement of a particle as [97, 98]

$$\overline{(r_1 - r_0)^2} = \int_0^\infty \omega(r, t)r^2 dr = 4D(t_1 - t_2), \quad (4.4)$$

where r_0 and r_1 are the distances to a particle from the initial position at two successive instances t_0 and t_1 . Equation (4.4) allows to express the diffusion coefficient as

$$D = \frac{\langle \Delta r^2 \rangle}{2z\Delta t}, \quad (4.5)$$

where $\langle \Delta r^2 \rangle$ is the mean-square displacement of a particle per time Δt , and z is defined by the dimensionality of space [97, 98]. In the case of particle diffusion on surface $z = 2$ (see Eq. (4.4)).

On the other hand, the mean-square displacement depends on the diffusion rate and on the particle hopping length, which in the example considered equal to the particle diameter d_0 :

$$\langle \Delta r^2 \rangle = \Gamma d_0^2 \Delta t. \quad (4.6)$$

Here Δt has a meaning of a single simulation step defined in Eq. (4.2). Substituting Eq. (4.6) into Eq. (4.5), one obtains

$$D = \frac{\Gamma d_0^2}{2z}. \quad (4.7)$$

Equation (4.7) allows to estimate Γ (and therefore Δt) once the diffusion coefficient is known:

$$\Delta t = \frac{d_0^2}{2zD}. \quad (4.8)$$

For example, the diffusion coefficient of an Ag_{500} cluster on graphite at room temperature was measured as $2 \times 10^{-7} \text{ cm}^2/\text{s}$ [19]. Substituting this value into Eq. (4.8), one obtains $\Delta t = 78 \text{ ns}$.

Substituting Eq. (4.1) into Eq. (4.7), one relates the diffusion coefficient to the activation energy and temperature:

$$D = \frac{d_0^2 \nu_1}{2z} \exp \left[-\frac{E_a}{k_B T} \right]. \quad (4.9)$$

From Eq. (4.9) follows that the diffusion coefficient decreases as the activation energy grows. This results in an exponential growth of the time step Δt with E_a , since $\Delta t \sim 1/D$ (see Eq. (4.8)). Equation (4.8) introduces the optimal time step for the computations, because it defines the characteristic time at which a freely deposited particle gets displaced for the distance d_0 , i.e. to the neighboring lattice cell (see Fig. 4.1). Note that the diffusion of deposited particles is typically the fastest process in the system. Therefore, it determines the minimum time step and time scale for the growth and fragmentation of pattern on surface. It is computationally inefficient

to perform simulation with a time step less than Δt , because in this case the particles will practically not move during $t \ll \Delta t$.

In present method the following procedure to model particle dynamics on surface was employed: for each step of the simulation all freely deposited particles have six diffusion possibilities (see Fig. 4.1). The direction of displacement is chosen randomly and each particle is moved to a neighboring lattice cell in the chosen direction. Thereby each step of the simulation corresponds to $\Delta t = 78$ ns, as estimated above. The particles at the islands periphery diffuse slower, and therefore are displaced less frequently.

The relaxation of the system in such model is driven by diffusion of particles along the agglomerated islands periphery and particle detachment from the islands. Both processes are schematically depicted in Fig. 4.1. The diffusion and the detachment rates depend on the activation energy and the particle-particle interaction. In Arrhenius approximation, the diffusion rate of a particle along the periphery of an agglomerated island reads as:

$$\Gamma_d(m, n) = \nu_2 \exp \left[-\frac{mE_b}{k_B T} - \frac{n\Delta\epsilon}{k_B T} - \frac{E_a}{k_B T} \right], \quad (4.10)$$

where m is the number of bonds that are broken due to the particle motion, $E_b > 0$ is the binding energy of two particles, n is the number of maintained neighboring bonds between two particles and $\Delta\epsilon \leq E_b$ is the diffusion energy barrier [10,102], ν_2 is the attempt escape rate. Equation (4.10) describes the probability of a particle to overcome a potential energy barrier, which for a particle diffusing along the island periphery is parameterized by the energies E_b , $\Delta\epsilon$, and E_a . Note that the parameter E_a , which enters Eq. (4.10), depends on the simulation time step Δt , as discussed above. Therefore, only the parameters E_b and $\Delta\epsilon$ define the potential energy barrier for particle diffusion along the island periphery, while E_a characterizes the time scale.

Note that Eq. (4.10) does not account for the bonds which may be created in the system when a particle diffuses. This feature of Eq. (4.10) is easy to understand. Indeed, in our model the particle diffusion process is considered stepwise, i.e., at each step of the computation a particle is displaced with a certain probability on the distance equal to its diameter in a random direction. But prior the particle is displaced to its new location there is no information about the newly created bonds in the system (causality principle). Therefore only those bonds which the particle forms with its neighbors prior the displacement influence the diffusion dynamics in

the system.

The evaporation (detachment) rate of a particle from the island is given by

$$\Gamma_e(l) = \nu_3 \exp \left[-\frac{lE_b}{k_B T} - \frac{\Delta\mu}{k_B T} - \frac{E_a}{k_B T} \right], \quad (4.11)$$

where l is the number of bonds broken after particle detachment from the island, $\Delta\mu$ is the chemical potential of particle detachment [2,10,102,103], ν_3 is the attempt escape rate of a particle from its equilibrium position. Equation (4.11) can be understood within the framework of the classical nucleation theory [103], which studies the liquid \leftrightarrow gas transition in droplets. It is written in the Arrhenius approximation, similarly to Eq. (4.11). For the further description was established that:

$$\nu_2 \simeq \nu_3 = \nu. \quad (4.12)$$

Such situation occurs when the characteristic attempt escape rate of a particle leading to its diffusion or detachment are close. Equations (4.10)-(4.11) describe the dependence of the the probability of different essential kinetic processes on the values of E_a , E_b , $\Delta\epsilon$, $\Delta\mu$, which below are called the kinetic parameters. For the convenience, in this text all the kinetic parameters are defined in the units of $k_B T$ ($1 k_B T = 0.026$ eV) at room temperature (300 K).

4.2 Algorithm for the implementation of the kinetic model

Kinetic model was implemented in **MBN Explorer** computer package. In this section one possible algorithm of implementation is considered. Implementation of the kinetic model in **MBN Explorer** based on the modified version of the conventional kMC method. In this case, for each particle in the system first the number of possible diffusion directions are determined. Thereby, a particle can either diffuse freely, or diffuse along the periphery of the already pre-formed structure as illustrated in Fig. 4.1. A diffusion direction for a particle is chosen randomly in such a manner that all possible diffusion directions are equally probable. For the given diffusion direction the probability for particle diffusion is then calculated from the predefined physical parameters input into the system, and the particle is translated with calculated probability in the direction defined earlier.

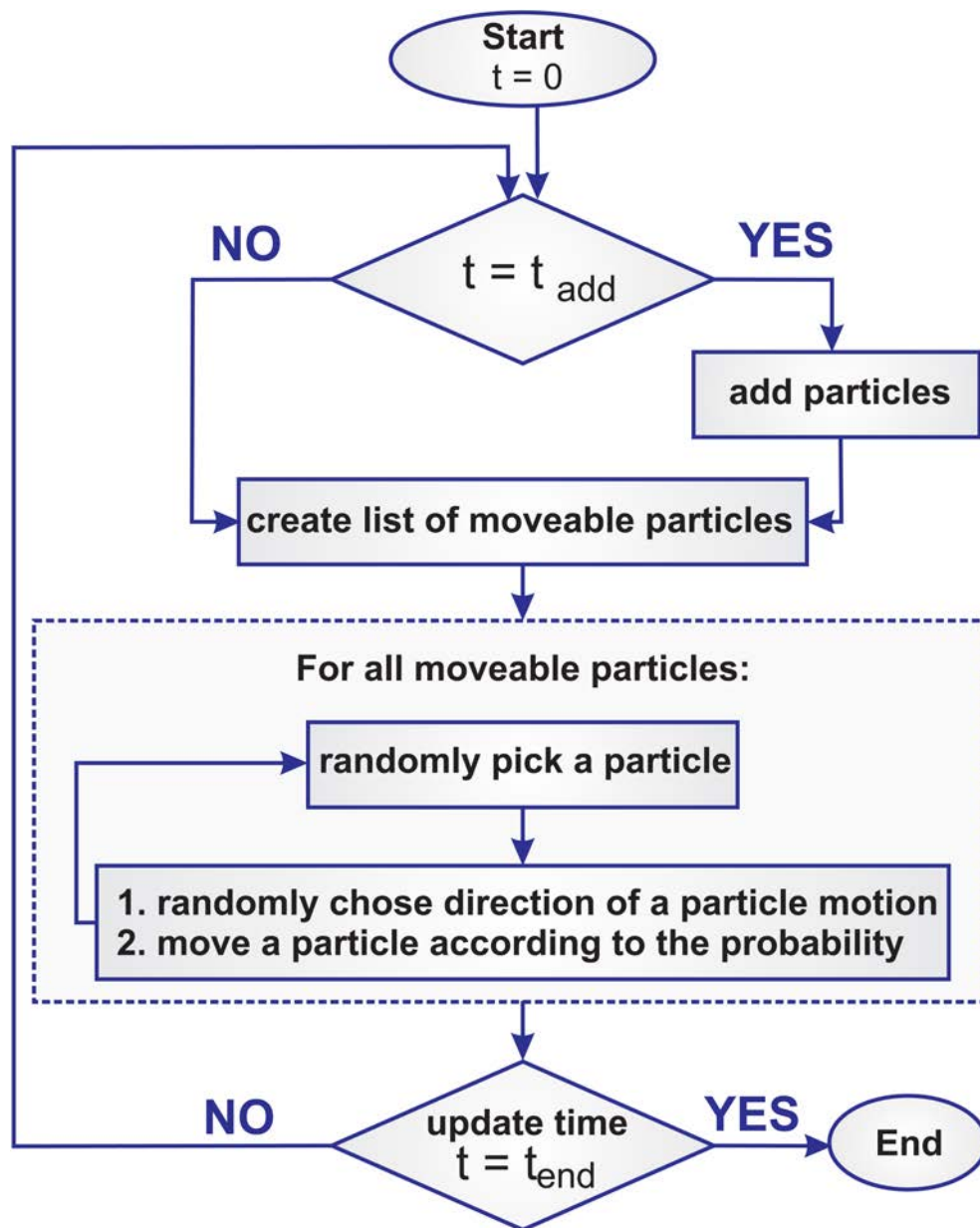


Figure 4.2: The principal scheme of the kinetic Monte Carlo algorithm, implemented in *MBN Explorer*, and used for the simulations of nanofractals formation and fragmentation on a surface.

The procedure is repeated at each simulation step of the random walk dynamics algorithm. The schematic representation of the algorithm is illustrated in Fig. 4.2. The algorithm proceeds as follows:

1. Load of the configuration from the input file (if applicable), code terminates.

2. Next the simulation time step is increased sequentially. At equal intervals, determined by the keyword in the task file, new particles are added into the system. The number of particles added at each step of the simulation is controlled by the relevant keywords in the task file.
3. At each step of the simulation the algorithm constructs a list of moveable particles in the system. If the particles in agglomerated islands are allowed to move, then the algorithm considers all particles in the system as potentially moveable.
4. The list of moveable particles is processed in the random order and all particles in the list are displaced in a random direction with a certain pre-calculated probability which is determined by the surrounding of each displaced particle (see Fig. 4.1).
5. The simulation is stopped once the total number of simulation steps reaches the maximal value specified in the task file.

To simplify the calculations, the random walk motion of particles is simulated on a lattice (grid). A lattice in the simulation represents an artificial subdivision of the entire simulation space into individual unit cells which can accommodate particles in the system. A particle on the lattice can occupy only a single unit cell and can move from the occupied cell only to the non-occupied neighboring cell (see Fig. 4.1). The number of possible diffusion directions of a particle depends on the packing of the lattice and on the number of occupied neighbor cells. **MBN Explorer** includes the cubic and the hexagonal types of the lattice packing which are described in appendix B in greater details.

4.3 Parameters of the kinetic model

Activation energy E_a

The interaction energy between the deposited particles and the substrate is responsible for the particle mobility on surface, as follows from Eq. (4.1). The interaction energy of Ag_{500} (E_a^{Ag}), C_{60} ($E_a^{\text{C}_{60}}$), and Sb_{2300} , (E_a^{Sb}) clusters with graphite surface at room temperature has been estimated as $E_a^{\text{Ag}} = 6.6 kT$ [55], $E_a^{\text{C}_{60}} = 6.9 kT$ [104] and $E_a^{\text{Sb}} = 27.1 kT$ [15]. The significant spread of the values indicates the essential

role of interatomic interactions in defining the activation energy. The value of E_a defines the time scale of the islands growth and fragmentation processes, as discussed in section 4.1. This work focuss on the study of silver cluster fractals, parameter E_a is assumed to be fixed.

Another important quantity characterizing the particle diffusion on surface is its attempt escape rate ν (see Eqs. (4.10)-(4.12)), which can be estimated as

$$\nu = \frac{2Dz}{d_0^2} \exp \left[\frac{E_a}{k_B T} \right]. \quad (4.13)$$

For a silver nanoparticle with $d_0 = 2.5$ nm deposited on graphite the diffusion coefficient at room temperature $D \simeq 2 \cdot 10^{-7}$ cm²s⁻¹ [19], resulting in $\nu = 0.94 \cdot 10^{10}$ s⁻¹.

Binding energy E_b and diffusion energy barrier $\Delta\epsilon$

The interaction energy of two particles, E_b , depends on the atomic composition of the particles and on the presence of impurities in the system [9, 10, 19]. It was shown that the presence of oxygen impurities in a silver cluster deposited on graphite leads to the decrease of E_b and consequently to the degradation of island stability. A systematic study of the afore mentioned factors on the interparticle interaction energy is beyond the scope of this paper and deserves a separate investigation. Note that in experiment [9, 19] silver cluster fractals are formed and may decay on the comparable time scales. This is only possible if E_b is of the same order of magnitude as E_a . The diffusion barrier energy $\Delta\epsilon$ depends on the atomic composition of the cluster and usually amounts 0.05 – 0.2 of the bonding energy of two clusters [105].

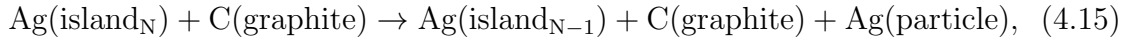
Chemical potential change

The change in the chemical potential $\Delta\mu$ arises due to the energy difference caused by the change of the number of particles in the system. The chemical potential characterizes the ability of particles to diffuse from regions of high chemical potential to those of low chemical potential and is virtually defined as the partial derivative [43]

$$\mu = \left(\frac{\partial U}{\partial N} \right)_{V,S}, \quad (4.14)$$

where U and S are the total energy and the entropy of the system, V is its volume and N is the number of particles in the system. The variation of the chemical

potential arising due to a structural transformation in the system can be calculated from the known values of the chemical potential of individual components of the system before and after the transformation. For example, for the evaporation of a silver nanoparticle from a agglomerated islands with N particles on graphite surface



the corresponding change of the chemical potential can be calculated as a difference between the chemical potential of the products and the adducts. With $\mu_{\text{Ag}(\text{island}_N)} \approx \mu_{\text{Ag}(\text{island}_{N-1})}$ one obtains

$$\Delta\mu = \mu_{\text{Ag}(\text{particle})}. \quad (4.16)$$

The chemical potential can be measured experimentally [106] and is tabulated for many substances (see e.g. [107, 108]). It depends on the phase state of the system: for the gas of silver atoms $\mu_{\text{Ag}}^{(\text{gas})} = 2.55$ eV, while for the silver in the liquid phase $\mu_{\text{Ag}}^{(\text{liquid})} = 0.8$ eV [107]. These values and Eq. (4.16) allow one to suggest that the change of the chemical potential in the silver islands fragmentation process, at room temperature lies within the range $30 - 100 kT$.

Chapter 5

Formation and fragmentation of nanofractals by nanoparticles deposited on a surface

In this chapter, the results of investigation of nanopattern formation and post-growth relaxation on a surface are presented. Particularly, formation and post-growth evolution of nanofractals were modeled with the kinetic model. Basic principles and assumptions of the kinetic model for an assembly of nanoparticles on a surface were discussed in pervious chapter (see chapter 4). The values of input model parameters were taken from the estimations performed in chapter 3 and from available data of experimental measurements (see section 4.3) .

In section 5.1, formation of nanofractals and nanodroplets on a surface, is explored. Kinetic model for an assembly of particles on a surface was used to simulate growing of a nanopattern on a surface by atomic cluster deposition. Based on the analysis of results of simulations, criteria, which can be used to distinguish between different patterns on a surface in the course of the pattern formation, are suggested, e.q. between fractals or compact islands. The criteria can be used to predict a morphology of growing structures on a surface.

In section 5.2, the post-growth evolution of patterns on a surface are analyzed. In particular, attention in the thesis is payed to a systematical theoretical analysis of the post-growth processes occurring in nanofractals on a surface. The time evolution of fractal morphology in the course of the post-growth relaxation was analyzed. The results of these calculations were compared with experimental data available for the post-growth relaxation of silver cluster fractals on graphite substrate [9, 10, 19].

5.1 Formation of a nanofractal by nanoparticles deposited on a surface

The conventional technique of thin-film growth by deposition of atoms [1, 3], small atomic clusters [2, 3] and molecules [1, 4, 5] on surfaces gives a possibility to construct materials with pre-defined properties. Recent experiments show that patterns with different morphology can be formed in the course of clusters deposition process on a surface [2, 3, 6]. Among other possible shapes, droplet-like and fractal islands have been observed in various systems [2, 3, 6]. Frequently a small change in the structure or composition of constituent nanoparticles or in the substrate results in a dramatic change in the properties of the entire system created in the course of the self-organization processes. Such factors, that we call critical factors can be the presence of activator-particles, defects, heterogeneity, the patterning, the roughness deformations of the supporting surface (substrate), acoustic waves, etc. Changes in properties can also be a result of variation of some characteristics of the environment in which the formation or the growth processes occur.

The investigation of the dendritic structures (fractals) has attracted considerable attention of many scientists [6, 9, 10, 19, 30–34]. The formation of such systems provides a natural framework for studying disordered structures on a surface because fractals are generally observed in far-from-equilibrium growth regime. During the last years fractal shape have been recordered for a variety of systems. For example, fractals consisting of Ag [9, 10, 19], Au [35], Fe-N [33] clusters and C₆₀ molecules [36, 37] have been fabricated on different surfaces with the use of the cluster deposition technique [1, 4].

The growth process of fractals has been extensively studied in experiments [15–18, 35, 36, 39]. In [15, 16] a quantitative experimental study of spherical antimony cluster diffusion on graphite was performed. It was shown that the size of the emerging fractals depends on the cluster deposition rate. The influence of cluster size on fractal morphology was experimentally studied in [14]. In that work antimony clusters of different size were subsequently deposited on graphite surface, and it was demonstrated that the fractal branch width depends on the size of the deposited clusters. Molecular processes, underlying the C₆₀-fractal formation on graphite substrate were investigated experimentally by use of the scanning tunneling microscopy [36]. The self-organization of silver clusters on graphite surfaces with different crystallographic orientations was experimentally investigated in [17].

It was shown that the size of the formed fractals depends on the crystallographic planes of graphite, which influences the cluster mobility on a surface.

5.1.1 Simulation of a nanofractal growth

The self-organization dynamics of particles on a surface was studied theoretically. An efficient theoretical tools for describing particle dynamics on a surface is the diffusion limited aggregation (DLA) method [109]. In this method each particle on a surface moves freely in a random direction until it collides with another particle. In case of collision, both particles stick together and become immobile. The DLA model was used for a qualitative description of the process of fractal formation on a surface [13, 15, 18, 102].

As a first approximation to model the growth of a fractal on a surface the diffusion limited aggregation (DLA) method [109] was used. Using a module of the `MBN Explorer` software package [110] the growth process of a fractal by depositing particles on a surface in the vicinity of the pre-defined growth center was computed. For the sake of illustration in Fig. 5.1a, fractals of the silver clusters on graphite surface are shown [9], while the fractal structures obtained from the calculation are shown in Fig. 5.1b. To compare with the experimental measurements [9, 10, 19] in our simulations the model parameters consistent with the experiment was used. Thus, the diameter of a particle has been taken 2.5 nm, which corresponds to the size of an Ag_{500} cluster used in Refs. [9, 10, 19]. The deposition flux has been decreased from $F_{start} = 7.2 \times 10^{13}$ particle/cm²s to $F_{end} = 1.1 \times 10^{11}$ particle/cm²s because the area to which the particles are added decreases as the size of the fractal increases. The used values of the particle deposition flux are chosen higher than the experimental value reported in Ref. [9, 19], $F = 10^{10}$ particle/cm²s, in order to accelerate simulation of the fractal growth.

The important characteristic of a fractal is the fractal dimension d_f . The Hausdorff fractal dimension is defined as [111, 112]:

$$d_f = \lim_{l \rightarrow 0} \frac{\log[N(l)]}{\log[1/l]}. \quad (5.1)$$

Here $N(l)$ is the number of self-similar structures of linear size l needed to cover the whole structure. In practice the fractal dimension is usually calculated by the box-counting method [113]. Equation (5.1) has been used to calculate the fractal dimension of the structures shown in Fig. 5.1b. This calculation resulted in $d_f^{th} =$

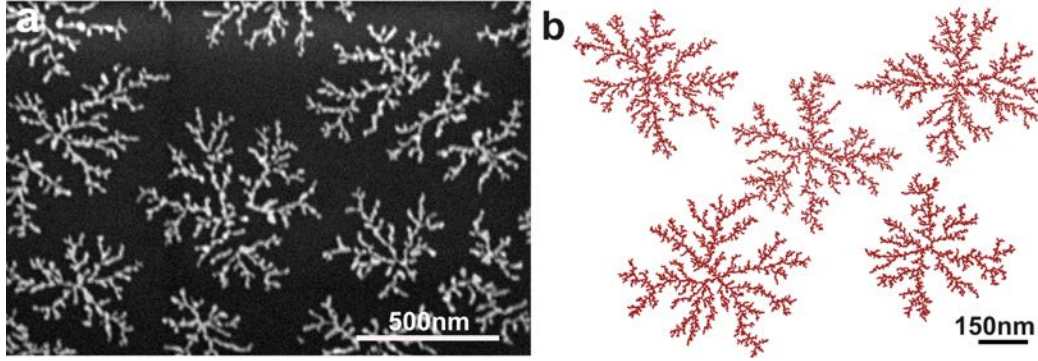


Figure 5.1: (a) Structures of the silver cluster fractal grown by clusters deposition technique on the graphite surface [9]; (b) Fractal structures grown by the DLA method;

1.7 ± 0.05 . This value is in a good agreement with experiment for silver cluster fractals grown on the graphite surface, which gives $d_f^{exp} = 1.7 \pm 0.1$ [9].

As illustrated in Fig. 5.1 the topology of fractals simulated by the DLA method is very similar to the fractal topology grown in experiment. In both cases the fractals shown in Fig. 5.1 have several main branches, growing from the center of the fractal. The branch width of the fractal simulated by the DLA method is ~ 10 nm, while the typical experimental width of the branch is 15 – 30 nm [9]. The difference arises because the particles in the simulation were deposited on a surface at a higher rate than those in experiment. In addition, the implemented DLA method does not allow the deposited particles to be placed atop of a growing fractal. Another factor affecting this difference is the sticking probability of the deposited particles assumed to be equal to one, meaning that if a particle meets another particle on a surface the two particles stick and do not move together. The central simulated fractal from the Fig. 5.1b have been used as initial structure in the investigation of fractal fragmentation.

5.1.2 Criteria for nanoscale surface pattern formation

Other task which was considered in the present work, was to understand the self-organization processes on a surface consider different characteristic time scales for different kinetic processes occurring with deposited particles on a surface. The important kinetic processes which govern pattern formation on a surface are illustrated in Fig. 5.2. The particle deposition time τ_{dep} (see Fig. 5.2a) is related to the particle flux F and the surface area S of the substrate as follows

$$\tau_{dep} = \frac{1}{FS}. \quad (5.2)$$

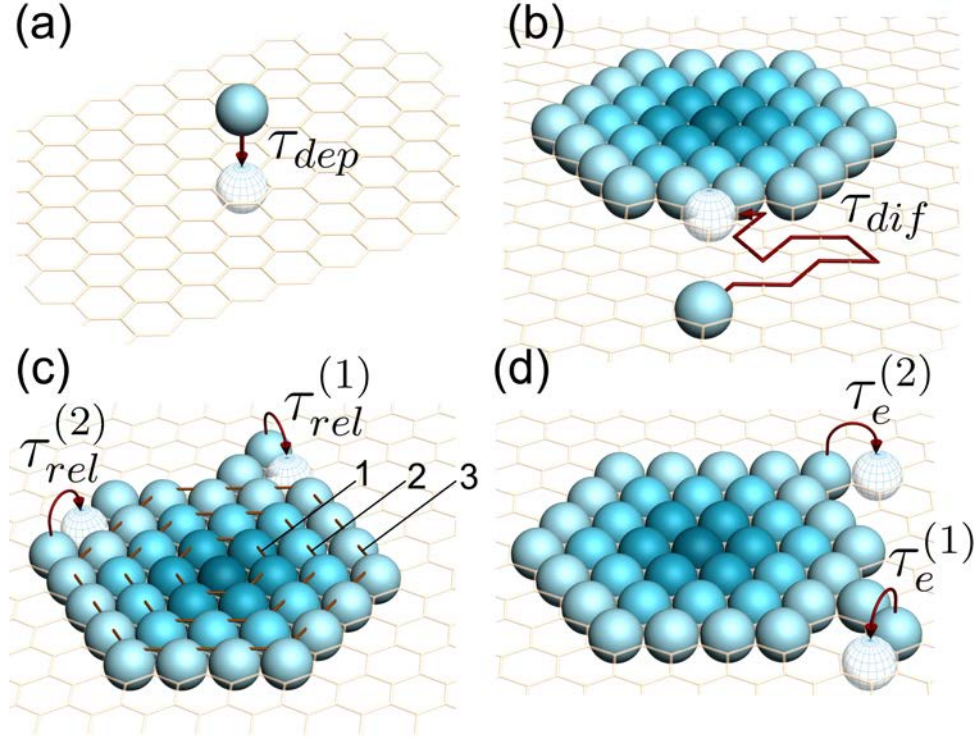


Figure 5.2: Characteristic times for different kinetic processes occurring with deposited particles on a surface: (a) particle deposition time τ_{dep} ; (b) particle diffusion time towards the periphery of a forming island τ_{dif} ; (c) peripheral particle diffusion time $\tau_{rel}^{(1)}$ without breaking bonds with neighbor particles, and $\tau_{rel}^{(2)}$ (with breaking bonds with neighbor particles); (d) detachment time of a particle from an island after breaking one bond $\tau_e^{(1)}$, and after breaking several bonds $\tau_e^{(2)}$

In the next series of the simulations of the pattern formation on a surface the substrate size was chosen as $500 \times 500 \text{ nm}^2$ and the deposition flux as $F = 10^{10}$ particle/cm²s, corresponding to the experimental value reported in [9, 19]. Thus, from Eq. 5.2 one obtains $\tau_{dep} = 0.04 \text{ s}$.

The diffusion time of a particle towards the periphery of an emerging island (see Fig. 5.2b) can be calculated as the time of the first passage of a particle from the deposition site to the periphery of the agglomerating structure as

$$\tau_{dif} = n_{steps} \Delta t, \quad (5.3)$$

where n_{steps} is the number of 'jumps' which a particle undertakes in the course of its random Brownian motion before reaching the periphery of an agglomerating

structure and Δt is defined in Eq. 4.8 (see chapter 4). For a $500 \times 500 \text{ nm}^2$ substrate $n_{steps} \leq 100$, allowing to estimate $\tau_{dif} \leq 7.8 \times 10^6 \text{ s}$, i.e. significantly smaller than τ_{dep} .

Particle peripheral diffusion time, or the particle rearrangement time, (see Fig. 5.2c) is decisive for pattern formation on a surface. Depending on the kinetic processes which occur on the periphery of an agglomerating structure one can expect various morphologies to emerge which may be as different as spherical droplets and tree-like fractal structures. The kinetic processes for a particle on the periphery of an agglomerated structure depend on the number of its neighbors. Figure 5.2c illustrates two abundant processes of particle peripheral diffusion which occur on characteristic time scales $\tau_{rel}^{(1)}$, and $\tau_{rel}^{(2)}$. These processes correspond to a particle diffusion along the periphery of an island without breaking bonds with the neighbor particles and with breaking a single bond with a neighbor particle, respectively. Using Eq. 4.10 and Eq. 4.8 (see chapter 4) the particle peripheral diffusion times $\tau_{rel}^{(1)}$ and $\tau_{rel}^{(2)}$ can be related to the diffusion coefficient D of a particle on a surface and the kinetic parameters $\Delta\epsilon$ and E_b :

$$\tau_{rel}^{(1)} = \frac{d_0^4}{4D} \exp\left(\frac{\Delta\epsilon}{k_B T}\right) \quad (5.4)$$

$$\tau_{rel}^{(2)} = \frac{d_0^4}{4D} \exp\left(E_b + \frac{\Delta\epsilon}{k_B T}\right) \quad (5.5)$$

Note that $\tau_{rel}^{(1)}$ and $\tau_{rel}^{(2)}$ are the times of particle peripheral diffusion calculated for the two abundant kinetic processes on the particle periphery. Other kinetic processes are significantly less probable and do not play a decisive role in distinguishing different growth paths of patterns on a surface.

Similar to the particle peripheral diffusion, one should also distinguish times for particle detachment processes (see Fig. 5.2d). The detachment time of a particle from an island after breaking one bond $\tau_e^{(1)}$ and after breaking two bonds $\tau_e^{(2)}$ can thus be written as:

$$\tau_e^{(1)} = \frac{d_0^4}{4D} \exp\left(E_b + \frac{\Delta\mu}{k_B T}\right) \quad (5.6)$$

$$\tau_e^{(2)} = \frac{d_0^4}{4D} \exp\left(2E_b + \frac{\Delta\mu}{k_B T}\right) \quad (5.7)$$

which depend on the diffusion coefficient D and the kinetic parameters $\Delta\mu$ and E_b . At room temperature, the rate of particle detachment is usually significantly lower than the rate of particle diffusion [107,108], because the change of the chemical

potential $\Delta\mu$ associated with particle detachment is $\Delta\mu > 100k_B T$ [107,108], leading to a fairly small values of $\tau_e^{(1)}$ and $\tau_e^{(2)}$.

Thus, for the studied value of particle deposition flux the morphology of pattern on a surface is determined by the particle deposition rate, the particle diffusion rate, and the particle rearrangement rate. The analysis of characteristic times for these kinetic processes allows to suggest the following conditions to distinguish between three different morphologies on a surface

$$\begin{aligned} \tau_{dep} + \tau_{dif} &\gg \tau_{rel}^{(2)}, & (\text{compact droplet}) \\ \tau_{rel}^{(1)} < \tau_{dep} + \tau_{dif} < \tau_{rel}^{(2)}, & (\text{fractal with thick branches}) \\ \tau_{dep} + \tau_{dif} &\ll \tau_{rel}^{(1)}, & (\text{fractal with thin branches}) \end{aligned}$$

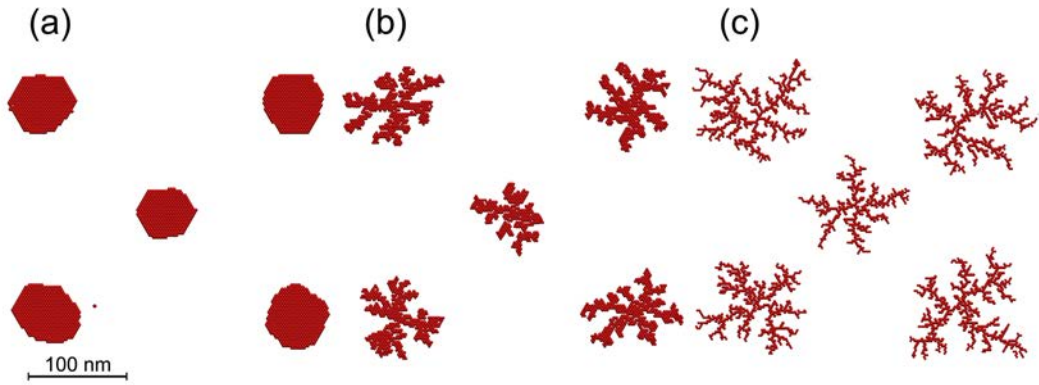


Figure 5.3: Morphology of different patterns observed after self-organization of particles on a surface at different conditions after 100 s of simulation. (a) Compact droplets are formed when the rearrangement time of particles is shorter than the nucleation time; (b) Fractals with thick branches form when some peripheral particles have enough time to rearrange and form a more compact structure; (c) Fractals with thin branches form when the inner dynamics of particles in the fractal is almost frozen.

The first inequality describes a situation when the agglomerated particles undergo fast relaxation. In this case the rearrangement time of particles is shorter than the nucleation time and therefore compact droplets are formed on a surface. The second condition is an intermediate case, which arises when some peripheral particles in agglomerated structures have enough time to rearrange and form a more compact structure. It generally should lead to the formation of fractals with thick branches. Finally, the third inequality in Eq. (5.8) describes the pattern formation regime when the inner dynamics of particles in the agglomerated structures is almost

frozen, and no rearrangement is possible, what leads to the formation of fractals with thin branches. Figure 5.3 illustrates the morphology of different patterns observed after self-organization of particles on a surface at different conditions after 100 s of simulation. The difference in the structure shown in Fig. 3 arises due to the variation of the kinetic parameters E_b and $\Delta\epsilon$ in Eqs. (5.4)-(5.5). Thus, for $E_b = 6k_B T$, $\Delta\epsilon = 2k_B T$ (see Fig. 5.3 a) one obtains $\tau_{rel}^{(1)} = 0.576 \mu\text{s}$ and $\tau_{rel}^{(2)} = 0.233 \text{ ms}$, satisfying the first inequality in Eq. (5.8). Fractals with thick branches (see Fig. 5.3 b) were obtained for $E_b = 30 k_B T$, $\Delta\epsilon = 10 k_B T$, which lead $\tau_{rel}^{(1)} = 1.718 \text{ ms}$ and $\tau_{rel}^{(2)} = 1.836 \times 10^{10} \text{ s}$. Increasing the values of the kinetic parameters leads to the increase of the relaxation times. Thus, for $E_b = 60k_B T$, $\Delta\epsilon = 20 k_B T$ one obtains $\tau_{rel}^{(1)} = 37.843 \text{ s}$ and $\tau_{rel}^{(1)} = 4.322 \times 10^{27} \text{ s}$, which fulfill the third condition in Eq. (5.8). As seen in Fig. 5.3 c, in this case the particles selforganize on a surface in a fractal structures with thin branches, whose width equal to the diameter of a single particle.

Figure 5.3 shows that by varying the kinetic parameters E_b and $\Delta\epsilon$ one obtains different pattern on a surface, as predicted by the conditions in Eq. (5.8). Thus, the conditions in Eq. (5.8), may be used in experiment to estimate the values of the kinetic parameters, once the morphology of a pattern on a surface is known, and therefore to provide an important tool for measuring interparticle energies.

5.2 Different paths of nanofractal fragmentation

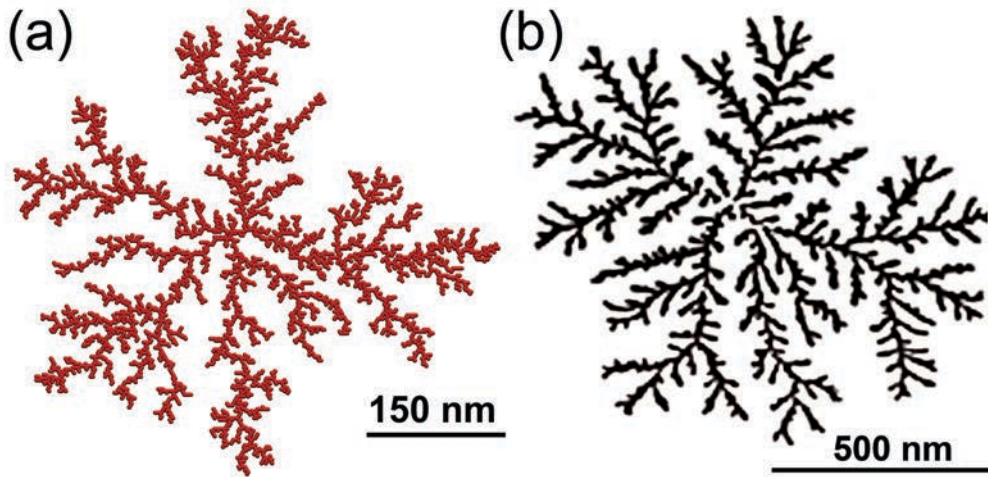


Figure 5.4: (a) Fractal structure grown by the DLA method; (b) structure of silver cluster fractal grown by clusters deposition technique on graphite surface [10];

Several fractal structures which are similar to the silver cluster fractals on graphite surface reported to be observed in experiment [9,10,19] was obtained using the DLA method (see section 5.1.1). The fractal structure shown in Fig. 5.4a was chosen for the further investigation of the post-growth relaxation processes in fractals. The diameter of the fractal is 550 nm, which is somewhat similar to than the diameter of experimentally grown structures [9,10,19]. For the sake of illustration in Fig. 5.4b is shown the experimentally grown silver cluster fractal prior thermal annealing, which triggers the fractal fragmentation [9,10,19]. As discussed in section 5.1 the topology of the fractal simulated by the DLA method is close to the fractal topology grown in experiment.

In this section we perform analysis of the fractal post-growth relaxation using kinetic model for an assembly of particles on a surface, which is discussed in detail in chapter 4. According to the estimates performed in Sec. 4.1, a single time step in calculation is equal to $\Delta t = 78$ ns, which allows one to simulate the process during the time period

$$t = N_{step}\Delta t, \quad (5.8)$$

where N_{step} is the number of simulation steps. In the present work several paths of fractal fragmentation was analyzed. The rate of fractal decay depends on the interparticle interaction, and it defines the morphology of the fragments that are formed during the process. Snapshots of the structures arising at different stages of the fragmentation process simulated at different parameters of interparticle interactions are shown in Fig. 5.5. This example shows how different can be the fragmentation paths and the fragments morphology.

Figure 5.5 shows that for $E_b = 1 k_B T$, $\Delta\epsilon = 0.2 k_B T$ one observes an entire defragmentation of a fractal, which is the fastest fragmentation path. In this case the interaction energy between the particles is relatively weak and the probability to evaporate a particle from the fractal is much higher than the probability of newly deposited particles to nucleate. This fragmentation scenario can be realized in experiment if the temperature of the system is rapidly elevated after the fractal was created.

Figure 5.5 shows that for $E_b \geq 2 k_B T$ the fractal melts in a number of compact droplets. Depending on the energies of interparticle interactions the shape of the droplets becomes different. Thus, for $E_b = 2 k_B T$, $\Delta\epsilon = 0.4 k_B T$ three large, almost spherical, droplets of a similar size are formed. In this case the binding energy E_b

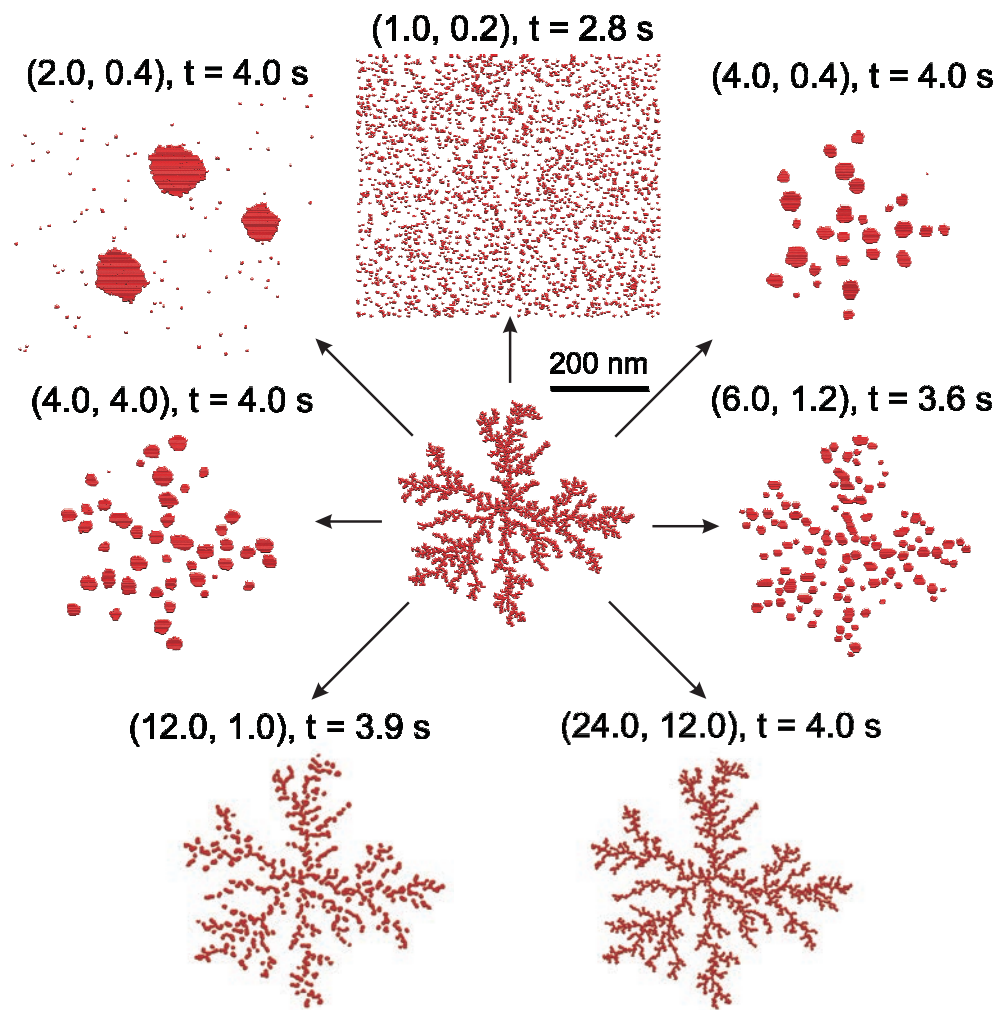


Figure 5.5: Evolution of fractal structure on a $650 \times 750 \text{ nm}^2$ substrate with periodic boundary conditions. The initial fractal structure shown in the middle undergoes fragmentation in different final states depending on the interparticle interactions in the system. Numbers above the corresponding images indicate the values of E_b and $\Delta\epsilon$ used in the simulations (in units of $k_B T$), $\Delta\mu = 2 k_B T$ in all cases. The simulation time t is given for each path of the fragmentation.

between the particles is rather small, allowing relatively easy detachment of particles, but at the same time it is large enough to make the characteristic particle detachment time comparable with the characteristic particle nucleation time, thereby preventing the system from entire defragmentation, observed at $E_b = 1 k_B T$. Thus, the fragmentation path at $E_b = 2 k_B T$ goes via the rearrangement of the entire system, and the formation of large stable droplets.

A further increase of the interparticle interaction energy leads to the change of the fractal fragmentation pattern. As seen in Fig. 5.5 at $E_b = 4 - 6 k_B T$ the fractal fragments into several compact droplets. The analysis of morphology of the created patterns leads us to the following main conclusions: (i) the growth of E_b leads to the increase of the number of droplets on a surface (see $E_b = 4 k_B T$ and $E_b = 6 k_B T$) and to the decrease of their average size. This happens because the detachment of particles from the fractal becomes energetically an unfavorable process, and the fractal fragments mainly due to the peripheral diffusion of particles, initiated at the peripheral defect sites. (ii) The increase of the peripheral diffusion barrier energy $\Delta\epsilon$ suppresses the diffusion of particles, resulting in a slower evolution and fragmentation of the fractal shape. It is remarkable that at $E_b = 6 k_B T$ and $\Delta\epsilon = 1.2 k_B T$ one observes the formation of elongated islands on a surface which follow the direction of the fractal branches. A further increase of the interparticle binding energy with the simultaneous lowering the barrier energy for the particle peripheral diffusion favors the formation of elongated islands on a surface. Figure 5.5 illustrates this for $E_b = 12 k_B T$ and $\Delta\epsilon = 1 k_B T$. In this case the timescale for the particles to detach from the fractal is significantly larger than that for the peripheral particle diffusion.

A simultaneous increase of the interparticle binding energy and the barrier energy for the particle peripheral diffusion leads to the growth of the fractal life time. Figure 5.5 shows that for $E_b = 24 k_B T$ and $\Delta\epsilon = 12 k_B T$ the fractal has no noticeable changes in its morphology after 4 s of simulation. In the case when the interparticle energies are large, the fractal fragmentation is expected to occur on a larger time scale and can be simulated numerically if the value of the simulation time step is increased.

The important characteristic of the fractal fragmentation is the number of fragments at a given time. The smallest fragment is a single particle. The time evolution of the number of fragments calculated for different sets of model parameters is shown in Fig. 5.6a and Fig. 5.6d. Curve 1 in Fig. 5.6a shows the time evolution of

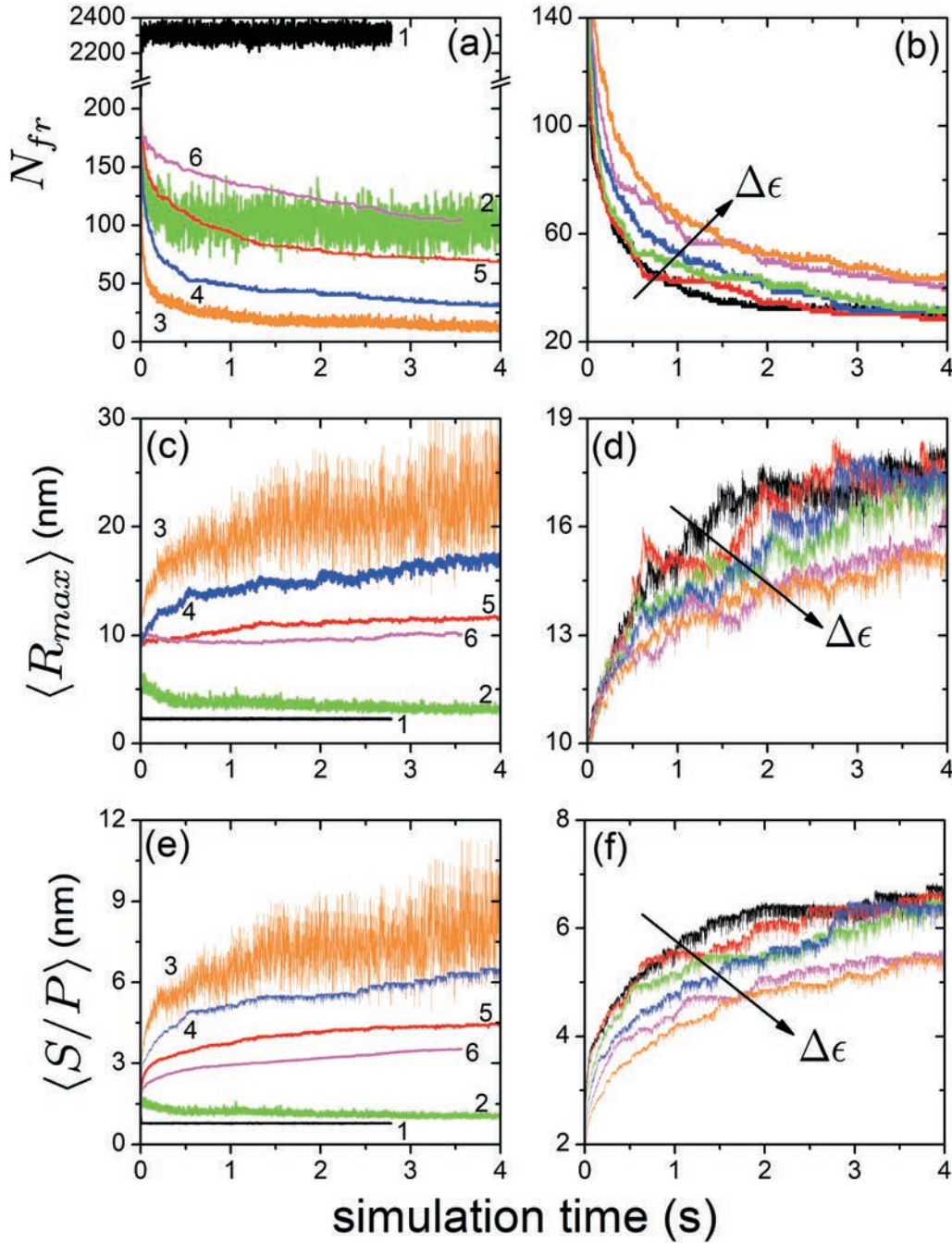


Figure 5.6: Time evolution of the number of fragments N_{fr} , $\langle R_{max} \rangle$ introduced in Eq. (5.9) and of the $\langle S/P \rangle$ ratio introduced in Eq. (5.17) calculated for the fractal structure shown in Fig. 5.5. The fractal fragmentation have been analyzed at $\Delta\mu = 2 k_B T$ for different values of the binding energy E_b and the barrier energy $\Delta\epsilon$. Plots (a), (c), (e) show the results of calculation obtained for $\Delta\epsilon = 0.2E_b$ and the different values of the binding energies between two particles. Lines 1-6 correspond to $E_b = (1, 2, 3, 4, 5, 6) k_B T$, respectively. Plots (b), (d), (f) represent the results obtained at $E_b = 4 k_B T$ for different values $\Delta\epsilon = (0, 0.4, 0.8, 1.0, 3.2, 4) k_B T$. The direction of growth of $\Delta\epsilon$ is shown in these plots.

the number of fractal fragments at $E_b = 1 k_B T$. The number of fragments in this case rapidly approaches the asymptotic value, approximately equal to the half of the total number of particles in the fractal. This means that the system dominantly consists of dimers. With increasing E_b the number of fragments at the equilibrium decreases, as seen in Fig. 5.6. It is interesting to note that at $E_b = 2 k_B T$ there are three dominating large islands (see Fig. 5.6). The total number of fragments at the end of the simulation in this case is equal to 100, being much smaller than the total number of particles in the system. This feature arises in the situation when a large number of single particles detach from the large droplets but later stick back. In this case the number of single particles fluctuates rapidly resulting in the large fluctuations of $N_{fr}(t)$ dependence shown in Fig. 5.6a by curve 2. These results have been calculated for a fractal on a $650 \times 750 \text{ nm}^2$ substrate with periodic boundary conditions.

Figure 5.6b shows that there is no dramatic change in $N_{fr}(t)$ dependence with the growth of $\Delta\epsilon$ at a constant value E_b . This analysis shows also that the growth of $\Delta\epsilon$ preventing particles peripheral diffusion hinders the fast transformation of droplets into compact islands which eventually results in the increase of the number of fragments on a surface.

As seen in Fig. 5.5, in the course of fractal fragmentation the mobile particles can coalesce into islands, i.e. groups of particles bound together. The size and the number of islands on the substrate depend on the binding energy E_b and the barrier energy $\Delta\epsilon$. The important characteristic of the fragmentation pattern on a surface is the average maximal radius of the created islands which reads as

$$\langle R_{max} \rangle = \frac{1}{N_{fr}} \sum_{i=1}^{N_{fr}} R_{max}^{(i)}, \quad (5.9)$$

where N_{fr} is the total number of islands on a surface, $R_{max}^{(i)}$ is the maximal radius of the i -th island. The dependencies of $\langle R_{max} \rangle(t)$ calculated at different values of E_b and $\Delta\epsilon$ are shown in Fig. 5.6c and Fig. 5.6d. These figures show that in average $\langle R_{max} \rangle$ approaches the equilibrium value at the chosen values of model parameters except for $E_b = 3 k_B T$, $\Delta\epsilon = 0.6 k_B T$ when the large fluctuations of $\langle R_{max} \rangle$ develop and grow with time. This happens because at $E_b = 3 k_B T$ the rate of single particle detachment turns out to be so that only several particles are able to overcome the detachment energy barrier at one simulation step. The escaped particles freely diffusing over the surface after a short period of time return to the same or some

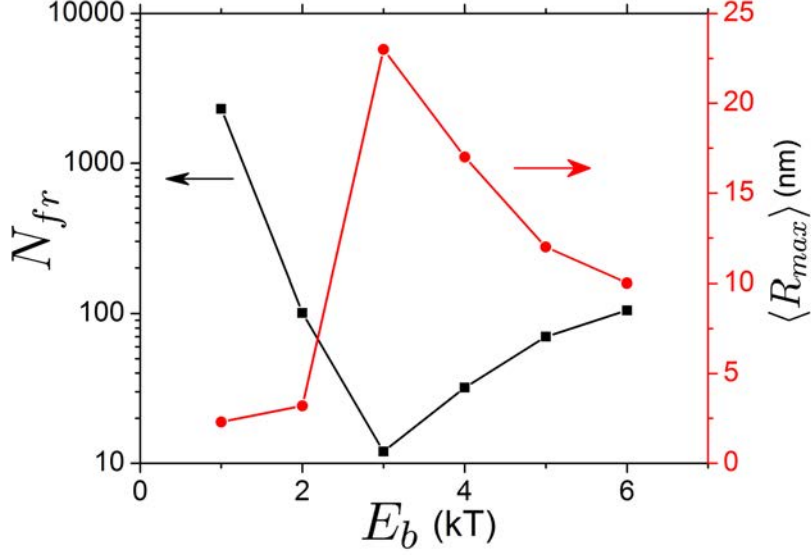


Figure 5.7: Dependence of the equilibrium value of N_{fr} (squares, left scale) and $\langle R_{max} \rangle$ (dots, right scale) on the binding energy E_b calculated for the barrier energy $\Delta\epsilon = 0.2E_b$, corresponding to the dependencies shown in Fig.5.6a and Fig. 5.6a.

other island. Although the number of fluctuating fragments on the surface in this case is relatively small (see Fig. 5.6a and Fig. 5.7), the fluctuations of $\langle R_{max} \rangle$ become considerable because at these conditions small islands can be spontaneously created but most of them disappear just after several simulation time steps. Thus, for example, for $t_1 = 3.490$ s $\langle R_{max} \rangle_1 = 14.3$ nm, while for $t_2 = 3.493$ s $\langle R_{max} \rangle_2 = 24.3$ nm. The change of the maximal radius $\Delta\langle R_{max} \rangle$ in this case is 10 nm within 3 ms time interval. This happens because for the time frame t_1 there are $N_S^{(1)} = 11$ single particles and $N_L^{(1)} = 10$ fragments of a larger size with approximately equal diameter on the surface. For the time frame t_2 the number of large fragments is $N_L^{(2)}$, still equal to 10, while there are only $N_S^{(2)} = 2$ single particles on the surface. With $R_L^{(1)} = R_L^{(2)} = R_L$ being the characteristic radius of the large island, $R_S^{(1)} = R_S^{(2)} = R_S$ the radius of a single particle, and $N_L^{(1)} = N_L^{(2)} = N_L$, one derives

$$\Delta\langle R_{max} \rangle = \frac{\Delta N_S N_L}{N_1 N_2} (R_L - R_S), \quad (5.10)$$

where $\Delta N_S = N_S^{(1)} - N_S^{(2)}$ is the change of the number of single particles, $N_1 = N_L + N_S^{(1)}$ is the total number of particles at instance t_1 , and $N_2 = N_L + N_S^{(2)}$ is the total number of particles at instance t_2 . Substituting values for ΔN_S , N_L , N_1 and

N_2 in Eq. (5.10) for the special case considered one obtains

$$\Delta\langle R_{max} \rangle = \frac{15}{42} (R_L - R_S). \quad (5.11)$$

Substituting $R_L=28.6$ nm and $R_S = 1.25$ nm in Eq. (5.11), one derives $\Delta\langle R_{max} \rangle = 10.7$ nm. Equation (5.11) shows that $\Delta\langle R_{max} \rangle$ increases with R_L which grows with time until it reaches the equilibrium value. Equation (5.10) can also be rewritten as

$$\Delta\langle R_{max} \rangle = \frac{\Delta N_S N_L}{N_1^2 (1 - \Delta N_S / N_1)} (R_L - R_S), \quad (5.12)$$

which shows that for $\Delta N_S \lesssim N_1$ the fluctuation of the average radius $\Delta\langle R_{max} \rangle$ can be several times larger than the value of the average radius. Note that although the largest islands are observed for the model parameter $E_b = 2 k_B T$ (see Fig. 5.5), the largest average maximal radius is expected for $E_b = 3 k_B T$ as depicted in Fig. 5.6. This happens because the number of single particles on the surface for $E_b = 3 k_B T$ is about 10, while for $E_b = 2 k_B T$ it is exceeding 100.

Figure 5.6c shows some dependence of $\langle R_{max} \rangle$ on $\Delta\epsilon$. The growth of $\Delta\epsilon$ leads to the decrease of $\langle R_{max} \rangle$, which is a natural result of a lower peripheral mobility of particles.

Figure 5.8 shows the distributions of island sizes in the system after 4 s of simulation. In order to improve the statistics, the distributions shown in Fig. 5.8 have been averaged over a time interval $\tau = 0.78$ s as follows

$$\overline{N_{fr}(t)} = \frac{1}{\tau} \int_{-\tau/2}^{\tau/2} N_{fr}(t-x) dx. \quad (5.13)$$

The histograms in Fig. 5.8 have been calculated with different barrier energies. The maxima in the distributions show the most abundant island sizes. Figure 5.8 shows that the sizes of the islands created in the fractal post-growth fragmentation process depend strongly on the binding energy E_b and the barrier energy $\Delta\epsilon$. At some values of E_b and $\Delta\epsilon$ one can identify two maxima in the island size distributions. Especially clear this feature manifests itself at $\Delta\epsilon = 0 k_B T$, $\Delta\epsilon = 0.4 k_B T$ and $\Delta\epsilon = 3.2 k_B T$. The presence of two maxima in the island size distributions tells that there are two groups of islands on the surface having different preferential island size.

Let us also analyze the time evolution of the distributions shown in Fig. 5.8. Figures 5.9 and 5.10 show distributions of the island sizes calculated at different fragmentation stages for a fixed set of the model parameters. Figure 5.9 illustrates

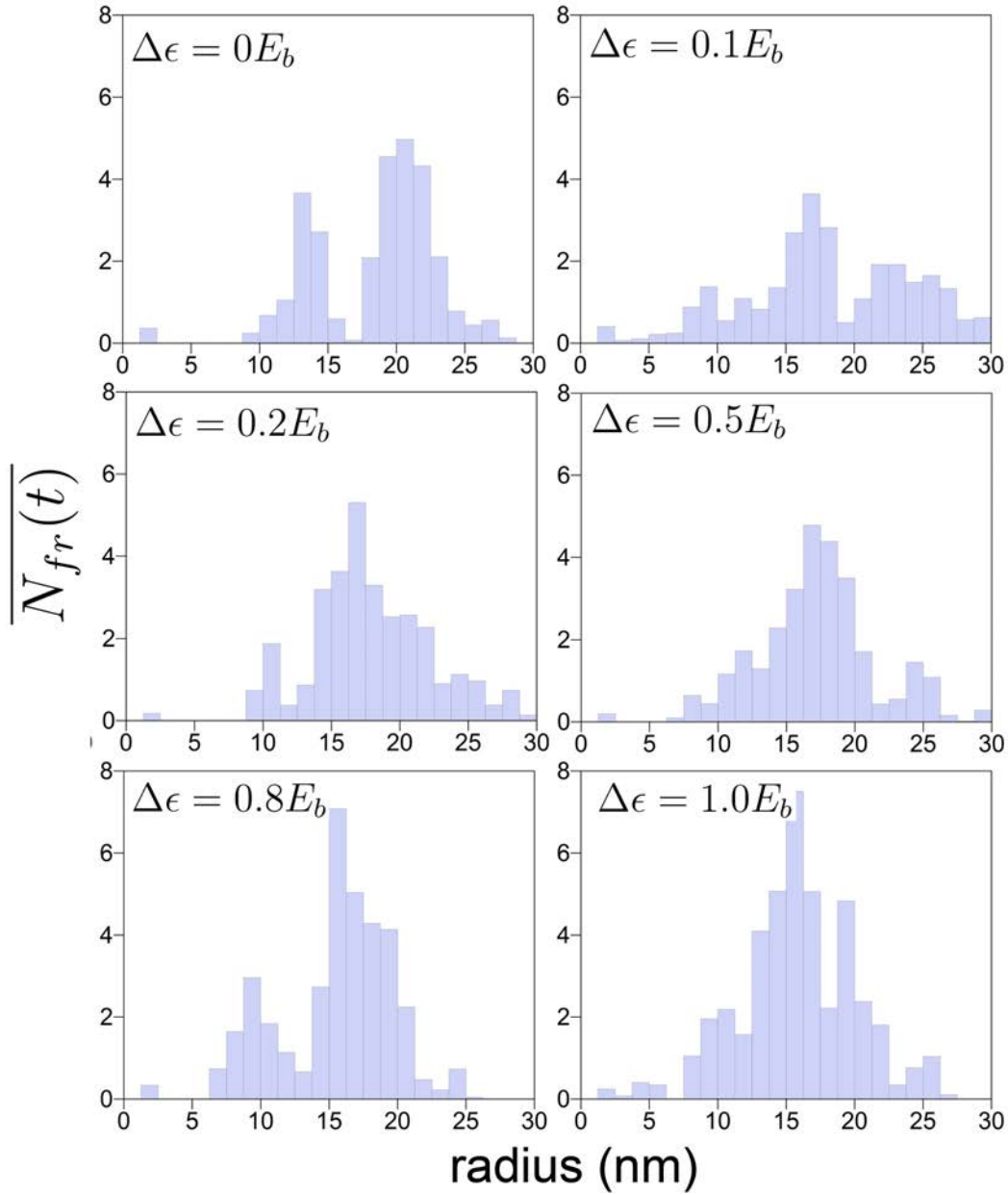


Figure 5.8: Distributions of island sizes formed on the substrate after 4 s of simulation. The distributions were calculated at the fixed values of $E_b = 4 k_B T$, and $\Delta\mu = 2 k_B T$ for different values of $\Delta\epsilon$ as indicated.

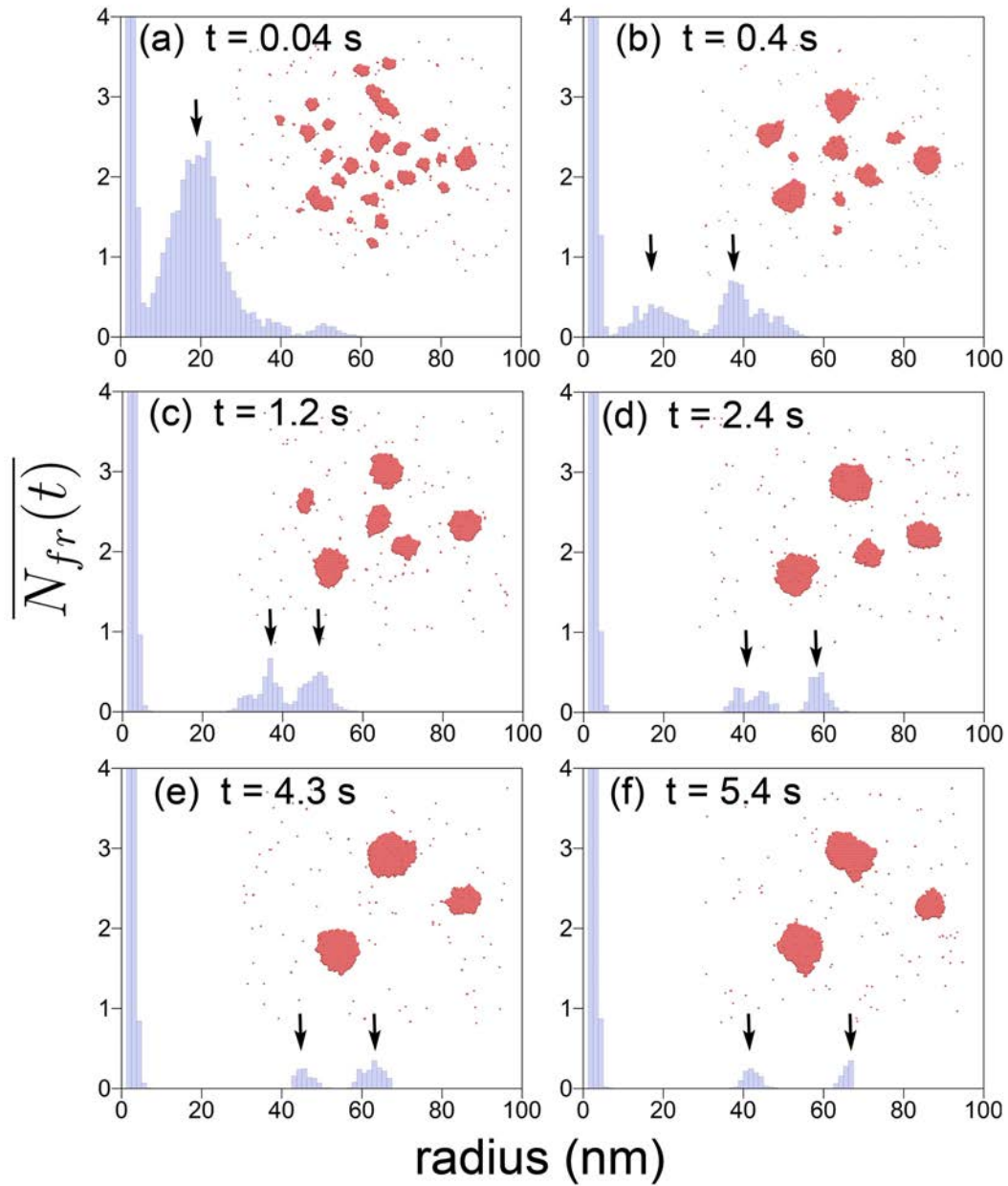


Figure 5.9: Size distributions of islands calculated at different stages of the fractal fragmentation (see Fig. 5.5) for $E_b = 2 kT$, $\Delta\epsilon = 0.4 kT$ and $\Delta\mu = 2 kT$. The corresponding simulation time is given in the insets to the plots.

the evolution of the island size distribution simulated at $E_b = 2 k_B T$ and $\Delta\epsilon = 0.4 k_B T$. After fast fragmentation of the fractal into a subset of noncompact islands which occurs on the time scale greater than 0.04 s, the distribution of islands sizes has a Gaussian-like shape with the maximum centered at 20 nm. In the course of the fractal fragmentation process the magnitude and the position of the maximum of the distribution change, because the morphology of the system changes due to the evaporation of single particles from the islands and the nucleation of single particles. Figure 5.9 illustrates that small islands nucleate into larger droplets resulting in a shift of the maximum of the distribution towards larger island sizes. Interesting that the fragmentation/nucleation dynamics leads in this case of study to the formation of two maxima which correspond to the presence in the system of the droplets of different radii.

Figure 5.9 shows the evolution of the fractal fragmentation process. The initial fragmentation of the fractal is very rapid. It involves the rearrangement of single particles in the fractal which form the defects at the fractal periphery. The evolution of the shape of the large droplets slows down with the growth of their size due to the decrease of the droplets mobility (see Figs. 5.9b-c). At the stage when only a few large-size droplets remain their dynamics is governed to large extent by the interchange of peripheral particles from these droplets (see Figs. 5.9d-f). The large droplets diffuse slowly over a surface and may eventually merge. The characteristic time scale for diffusion of an entire large droplet is significantly larger than the characteristic diffusion time of single constituent particle, and therefore practically can not be resolved within the simulation time limit. However, note that this motion can also be simulated with a larger time step. The appropriate value of the time step can be estimated using Eq. (4.8).

Figure 5.10 shows the slower evolution of the island size distribution as compared to Fig. 5.9. Slowing down of the process is caused by the increase of the binding energy E_b between particles within the fractal. Figure 5.10 shows that as in Fig. 5.9 a Gaussian-like distribution of a large number of droplets arises immediately after the fractal fast fragmentation. The maximum of this distribution slowly drifts towards the larger droplet sizes as the smaller islands nucleate (see Fig. 5.10b). Remarkably, that at the later stages ($t = 4$ s, Fig. 5.10d) two maxima arise in the distribution. It is worth noting that this feature of the droplet size distribution was also observed in experiment [114].

Another useful quantity for the characterization of surface structures is the ratio

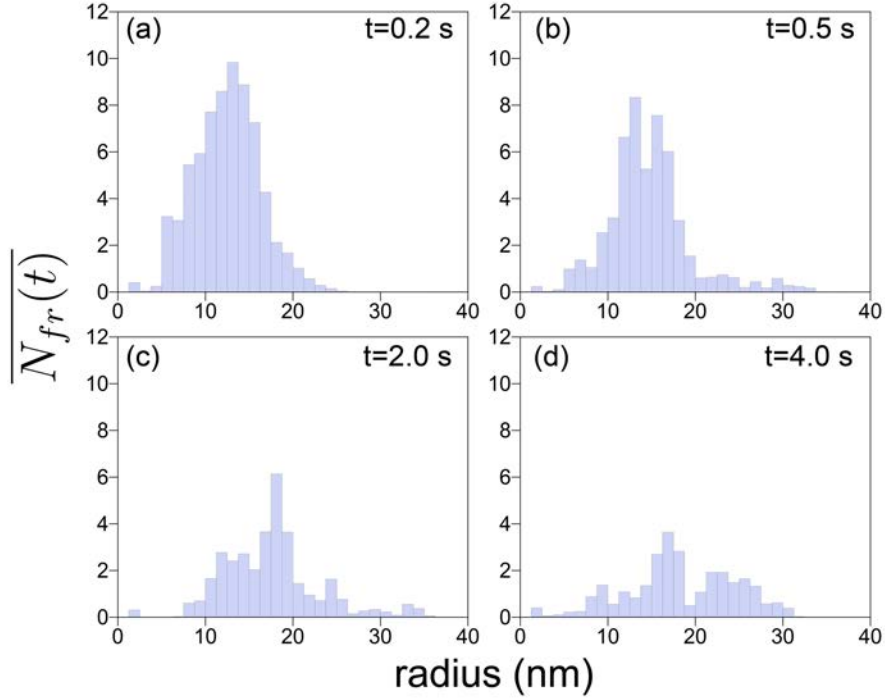


Figure 5.10: Similar to Fig. 5.9, size distributions of islands calculated at different stages of the fractal fragmentation (see Fig. 5.5) for $E_b = 4 k_B T$, $\Delta\epsilon = 0.4 k_B T$ and $\Delta\mu = 2 k_B T$. The corresponding simulation time is given in the insets to the plots.

between the area and the perimeter of the structure (S/P ratio) [9]. This ratio characterizes the island topology. Thus, the S/P ratio for a linear chain of N spherical particles is equal to

$$\frac{S}{P} = \frac{d_0}{4}, \quad (5.14)$$

where d_0 is the diameter of a particle. Note that the S/P ratio for a linear chain is always a constant. The S/P ratio for a compact droplet of the radius, R_d , is equal to

$$\frac{S}{P} = \frac{R_d}{2}. \quad (5.15)$$

It can be easily expressed via the number of particles N in the droplet:

$$\frac{S}{P} = \frac{d_0}{4} \sqrt{N}. \quad (5.16)$$

In this case the S/P ratio increases as \sqrt{N} with the growth of the system size. The

S/P ratio for a fractal consisting of N particles should be larger than in Eq. (5.14) and smaller than in Eq. (5.16). Let us now analyze the time evolution of the average $\langle S/P \rangle$ ratio of the system during the fractal fragmentation. The $\langle S/P \rangle$ ratio for a system of N islands is defined as

$$\langle S/P \rangle = \frac{1}{N_{fr}} \sum_{i=1}^{N_{fr}} \frac{S_i}{P_i}, \quad (5.17)$$

where S_i and P_i is the area and the perimeter of i -th island, and N_{fr} is the number of islands in the system. The $\langle S/P \rangle$ ratio is a useful characteristic for the structures morphology, often used in experiment [9].

The dependence of the $\langle S/P \rangle$ ratio on time calculated for different sets of the model parameters is shown in Fig. 5.6e and Fig. 5.6f. Curve 1 in Fig. 5.6e shows time evolution of the $\langle S/P \rangle$ ratio during the fractal relaxation in the case of the relatively small binding energy between the particles being equal to $1 k_B T$. The $\langle S/P \rangle$ ratio in this case rapidly decreases until it reaches the minimum value 0.78 nm, i.e. the S/P ratio which is slightly smaller than the value for a dimer of particles with $d_0 = 2.5$ nm. Figure 5.6 shows that the $\langle S/P \rangle$ dependencies to large extend follow the dependencies calculated for $\langle R_{max} \rangle$.

The performed analysis provides a lot of useful information on the dynamical evolution of the system during fragmentation. However, its direct comparison with experimental measurements is rather difficult because the calculated distributions vary with time, but the experimental measurements are usually performed for stationary (or quasi-stationary) systems. Nevertheless the comparison with experiment is possible if the average life-time T_l of the studied configuration is greater than the characteristic measurement time T_m :

$$T_l \gtrsim T_m. \quad (5.18)$$

Here, T_l is defined as the characteristic time-period at which an observable characteristic, e.g., the number of fragments in the system, changes within the statistical uncertainty, and T_m is the minimal time-period required to perform an experimental measurement.

An important characteristic of the system's stability, is the total number of fragments N_{fr} in the system. At the equilibrium N_{fr} fluctuates around the average constant value. Note, that N_{fr} may have similar behavior in a so-called kinetically

trapped state, or a quasi-equilibrium state which is separated from the equilibrium state by an energy barrier. The energy barrier between the kinetically trapped state and the equilibrium state may be significantly larger than the thermal vibration energy, therefore the trapped system may spend a noticeable lifetime in the kinetically trapped state. This life-time can be sufficient for experimental measurements and for holding Eq. (5.18). This means that the quasi-equilibrium value of N_{fr} may come out different for different initial distributions of particles on a surface, demonstrating that different evolution paths may lead the system to different final quasi-equilibrium states. Below we analyze two examples supporting this hypothesis.

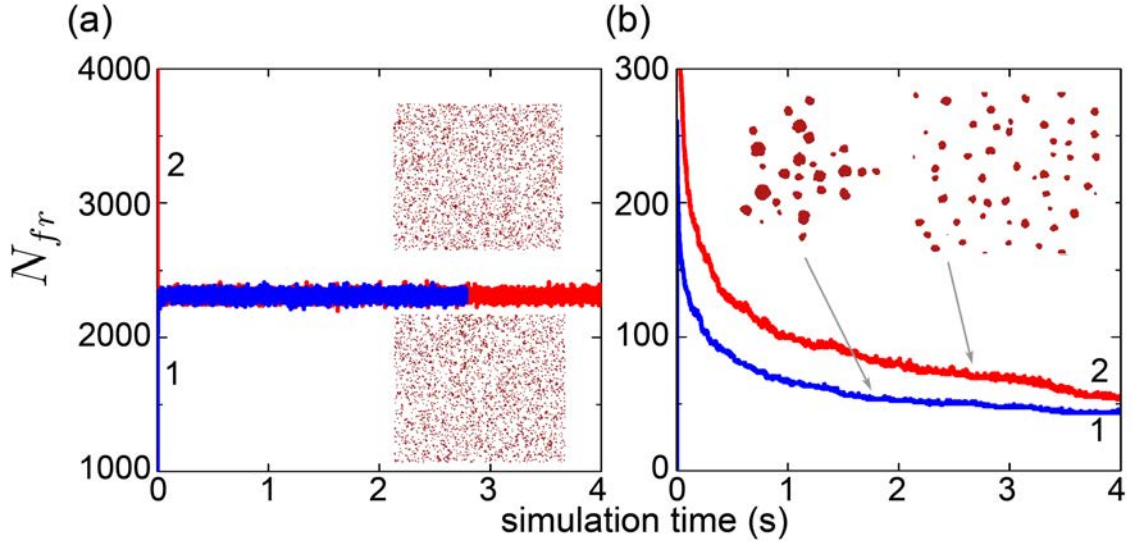


Figure 5.11: Time evolution of the number of fragments/nucleation islands on a surface, N_{fr} , during the fractal fragmentation process (line 1) and during the nucleation process of randomly distributed particles (line 2). The calculations have been performed for a $650 \times 750 \text{ nm}^2$ square substrate with periodic boundary conditions. Plots (a) and (b) have been calculated at different values of the model parameters: (a) $E_b = 1 \text{ kT}$, $\Delta\epsilon = 0.2 \text{ kT}$, $\Delta\mu = 2 \text{ kT}$; (b) $E_b = 4 \text{ kT}$, $\Delta\epsilon = 0.4 \text{ kT}$, $\Delta\mu = 2 \text{ kT}$. The insets show the morphology of the system at the end of the simulation.

Figure 5.11 depicts the time evolution of the number of fragments/nucleation islands, N_{fr} , calculated (line 1) for the fractal having the initial shape as plotted in Fig. 5.4a, and (line 2) during the nucleation process of randomly distributed particles. The total number of constituent particles in both cases is equal to 5182.

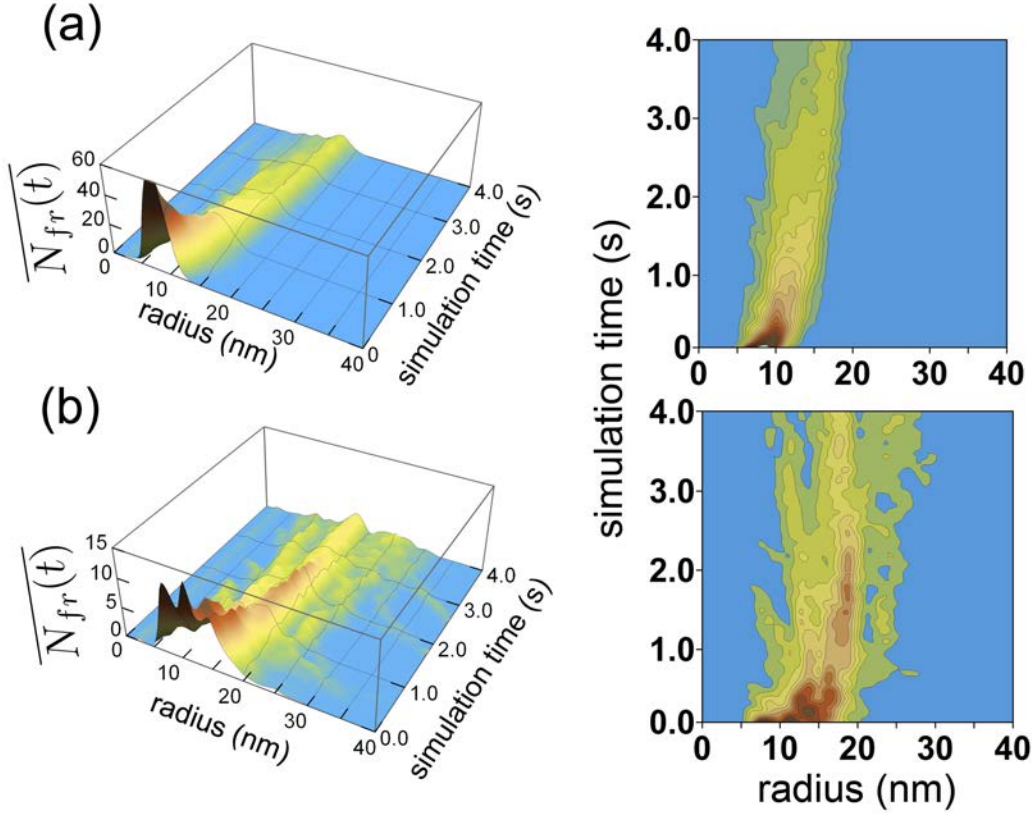


Figure 5.12: Time evolution of the island size distributions calculated for the nucleation process of randomly distributed particles (plot a) and for the fractal fragmentation process (plot b). The distributions have been calculated for the same values of the model parameters as in Fig. 5.11b. The initial fractal shape has been chosen the same as in Fig. 5.4a.

The size of the substrate used in the simulation is identical in both cases, equal to $650 \times 750 \text{ nm}^2$. Figure 5.11 shows that the inter-particle interaction influences significantly the system dynamics. Thus, in the case of the weak bonding between particles (i.e. $E_b = 1 k_B T$, $\Delta\epsilon = 0.2 k_B T$), see Fig. 5.11a line 1, the fractal fragments into ~ 2320 islands, i.e. most of the particles in the system are bound in a form of dimers. Remarkably, that at these model parameters particles randomly distributed over a surface nucleate to approximately the same quasi-equilibrium value N_{fr} (line 2 in Fig. 5.11a). The insets in Fig. 5.11a illustrate the distribution of particles at the instant $t = 4 \text{ s}$ in the case of nucleation and at $t = 2.8 \text{ s}$ for the fragmentation. Figure 5.11a shows that the system can evolve from the very different initial states to the same final state.

The fragments number evolution with time depend on the inter-particle inter-

action as seen from Fig. 5.11b, obtained at larger E_b , $E_b = 4 k_B T$, $\Delta\epsilon = 0.4 k_B T$. The quasi-equilibrium value of N_{fr} in this case depends on the initial distribution of particles on a surface. The inset to Fig. 5.11b shows that both systems have evolved in a group of droplets, whereby the size of the droplets created from the initial fractal distribution of particles is larger than the size of the droplets created via the nucleation.

Figure 5.11 shows that for the chosen model parameters the number of fragments in the system becomes constant or changes slowly with time at sufficiently large t value. The resulting static or quasi-static distributions of particles can be compared with experimental observations. In the cases when the initial distribution of particles on a surface influences the final morphology of the system means the system occupies one of the kinetically trapped state. Although the quasi-equilibrium kinetically trapped states do not have the lowest free energy, they may live for sufficiently long time to perform experimental measurements of the system characteristics. The asymptotic behavior of the fragments distribution with time is well seen in Fig. 5.12. Figure 5.12 shows the time evolution of the island size distributions calculated for the processes depicted in Fig. 5.11b. The island size distribution characterizing the period 0 – 2 s experiences significant variation, while the distribution during 2 – 4 s is almost static, with only a minor change.

5.3 Fragmentation of silver cluster nanofractals: theory predictions versus experimental observations

In this section, S/P ratio distributions calculated after the fractal fragmentation and the corresponding distributions of island sizes are compared with the results of experimental measurements for silver fractal fragments created via annealing, and by adding of oxide impurities to silver clusters [9].

Figure 5.13 shows the island size distributions and the corresponding S/P ratio distributions calculated for the fractal fragmentation on the $650 \times 750 \text{ nm}^2$ with periodic boundary conditions. The distributions plotted in Figs. 5.13a-b have been obtained with the model parameters $E_b = 3 k_B T$, $\Delta\epsilon = 0.6 k_B T$, $\Delta\mu = 10 k_B T$ at $t = 4 \text{ s}$, i.e. well after the fractal fragmentation when the system evolves in the almost stationary equilibrium or quasi-equilibrium state. In this case diffusion of

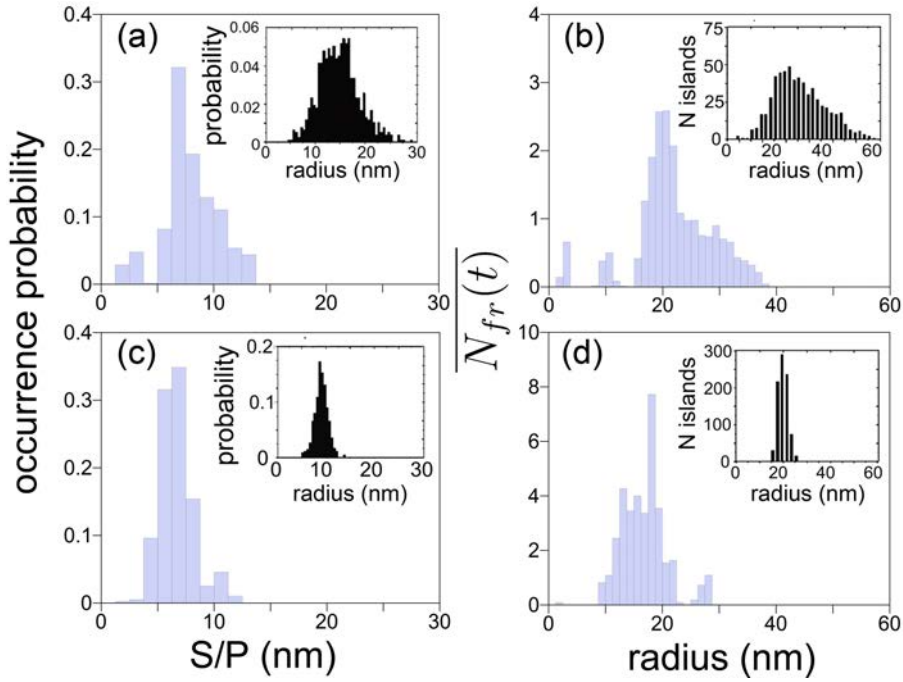


Figure 5.13: S/P ratio distributions calculated after the fractal fragmentation with different sets of the model parameters and the corresponding distributions of island sizes. Distributions (a) and (b) are calculated with $E_b = 3 k_B T$, $\Delta\epsilon = 0.6 E_b$, $\Delta\mu = 10 k_B T$; (c) and (d) with $E_b = 4 k_B T$, $\Delta\epsilon = 0.4 E_b$, $\Delta\mu = 2 k_B T$. Insets show the results of experimental measurements for silver fractal fragments created via annealing (a) and (b), and by adding of oxide impurities to silver clusters (c) and (d) [9].

particles along the fractal periphery is the dominating process. The increased rate of particle peripheral diffusion leads to the faster island rearrangement, and the formation of islands of different size, as seen in Fig. 5.13b. The insets in Fig. 5.13a-b show the results of experimental measurements obtained for silver fractals fragmentation via annealing at 600 K. The experimentally measured distribution of the silver cluster island sizes is rather broad, with the most probable radius of silver islands ~ 25 nm. A close value of 20 nm follows from the theoretical analysis. The discrepancy may arise due to the thinner branches of the fractal used in the simulations as compared to the ones analyzed in experiment.

Figures 5.13c-d show the island size distribution and the corresponding S/P ratios distributions calculated with $E_b = 4 k_B T$, $\Delta\epsilon = 0.4 k_B T$, $\Delta\mu = 2 k_B T$. The results of numerical calculation are compared with the experimental data shown in the insets to Figs. 5.13c-d on silver fractals grown with the oxidized silver nanopar-

ticles [9]. In the experiment the most abundant radius of the silver cluster islands is 18 nm, being in good agreement with the results of our calculations as seen from Fig. 5.13d.

Note that the width and the position of the maximum in the calculated distributions shown in Fig. 5.13 are rather close to the experimentally observed ones while the absolute value of the experimental and theoretical distributions differ quite significantly. This happens because we analyze the dynamics of a single fractal, while the experimental measurements deal with many fractals on a surface.

Chapter 6

Summary and conclusions

This work is devoted to the theoretical study of the formation and post-growth evolution of nanostructured materials fabricated by atomic clusters deposition on a surface. For this study there was developed a method, which is based on the kinetic Monte Carlo approach, and took into account internal diffusion processes of an assembly of nanoparticles on a surface. With this approach it was demonstrated, that the detachment of particles from the preformed island and their diffusion within the island and over the surface determine the evolution scenarios of the pattern morphology in course of the formation and post-growth relaxation.

The thesis begins with the theoretical analysis of the behavior of a single atomic cluster on a surface. Stability, energy, and geometry of an atomic cluster on a solid surface are studied with the method, which is based on the liquid drop model that accounts for the interaction between the cluster and the solid, and takes into account corrections related to deformation of the cluster on the solid surface. In chapter 3 it was shown, that the results of calculations performed within the framework of the liquid drop model stand in a good agreement with the results of numerical simulation based on a dynamic search for the most stable isomers in the course of cluster growth. The results of calculations demonstrate the role of the deformation as a factor determining the shape and stability of a cluster on the surface. The proposed liquid drop model can be generalized to arbitrary cluster system with various interactions between particles.

Mobility of a single nanoparticle, in context of the work - atomic cluster, plays a key role in dynamics of an assembly of nanoparticles on a surface. In chapter 3 the results of the modeling of a cluster diffusion on a surface with the methods of classical molecular dynamics are present. Influence of the various essential param-

eters on diffusion of a cluster on a surface was investigated for concrete system: silver nanoparticle on graphite surface. In particular, such parameters as the cluster size, the binding energy between silver and carbon atoms and the temperature, were considered.

In the present work, a Monte-Carlo based approach was developed to describe the dynamics of an assembly of nanoparticles on a surface. This method accounts for the free particle diffusion on a surface, aggregation into islands and detachment from these islands. The main idea of the method is discussed in the chapter 4. The suggested method is general and can be used in studies of the formation and relaxation processes of different nanoobjects deposited on a surface. The developed model includes three parameters, which are determined by interatomic interactions in the system and could in principle be theoretically calculated for each particular case on the basis of the full atomistic approach for the dynamics of a single nanoparticle on a surface. The model parameters can also be obtained from experiment and are specific for different types of substrates and deposited materials. Developed method was implemented in *MBN Explorer* computer package. In appendix B, one possible implementation of developed model and corresponding logical tests, which are used to validate the correctness of the implemented algorithms, are discussed in details.

In chapter 5, the results of application kinetic model to study formation and fragmentation of nanofractals by nanoparticle deposited on a surface are discussed. The process of the pattern formation on a surface was modeled for several different scenarios. Based on the analysis of the results of simulations, criteria, which can be used to distinguish between different patterns on a surface, for example: between fractals or compact islands, were suggested. In this criteria, the morphology of a pattern on a surface is determined by the particle deposition rate, which is defined by the deposition flux, and the particle diffusion and rearrangement rates, which are depended on the interparticle interactions. The suggested criteria can be used to predict the final morphology of the growing structure.

In the thesis a systematical theoretical analysis of the post-growth processes occurring in nanofractals on a surface is presented. For this analysis it was used kinetic model for an assembly of nanoparticles on a surface. The simulations with the developed method demonstrate, that the shape and number of the nanoislands created on a surface in course of post-growth relaxation depend on the rate of a particle diffusion along a fractal periphery and a particle detachment rate. In chapter 5, analysis of the dynamics of a nanofractal on a surface at various values of the model

parameters within a wide range of values is presented. It reveals the main fragmentation scenarios of the system. The predictions of the developed method were compared with the results of experimental observation silver fractals fragmentation on a graphite surface. The suggested model is capable to reproduce the distributions of island sizes calculated after a fractal fragmentation for different scenarios of fragmentation. The good agreement of the results of calculations obtained using the developed method with the results of experimental measurements demonstrates that it can be used for the modeling and analysis of dynamics of the nanostructured materials on a surface.

The thesis presents a significant advance in the understanding of paths of the formation and fragmentation of deposited nanosystems. It opens a broad spectrum of questions for further investigations. Thus, it is interesting to explore the link of the model parameters with the structural properties (both electronic and geometrical) of the deposited particles and substrates as well as their thermal, mechanical, electromagnetic, etc. properties. Thus, for instance introduced model parameters can be determined from the molecular dynamics simulations of different diffusion processes occurring on a surface.

In the performed analysis the deposited particles are assumed to be stiff, i.e. without any internal degrees of freedom. However, the particle diffusion over a surface may change quite significantly when the particle experiences deformation or changes its phase state. Accounting for the detail internal structure and dynamics of particles in the context of their diffusion is one of the next obvious steps towards the better understanding of the very complex process discussed in this work.

In the present work nanoparticle dynamics in 2D is considered. Another obvious important extension of the model is to investigate the role of the third dimension in the process of fractal formation and fragmentation. This is especially interesting to do, because there are many examples of three dimensional fractal systems in biology [115,116], where the dendritic shapes are rather common. Understanding of the growth evolution and fragmentation of such systems is very important and may have applications in medicine.

Appendix A

Parameters of the interatomic interactions

This appendix contains parameters for some interatomic interactions. Some parameters listed here were used in calculations, which are discussed in this thesis. Parameters, which were not used in this work also listed in the appendix to demonstrate, that the same potentials can be applied for different type of materials.

A.1 Pairwise potentials

The simple pairwise potentials limited in their applications. However, noble gases can be represented well with the Lennard-Jones potential since their atoms are only attracted to each other by the van der Waals force. In present work, the argon cluster structures was modeled via the Lennard-Jones potential. The parameters ϵ and r_{min} corresponding to the van der Waals interactions between noble gas atoms can be found, e.g., in Ref. [85] and some of them are compiled in Tab. A.1.

Table A.1: *Parameters of the Lennard-Jones potential for different atomic pairs.*

atomic pair	ϵ (meV)	r_{min} (Å)	Ref.	atomic pair	ϵ (meV)	r_{min} (Å)	Ref.
<i>Ar - Ar</i>	12.3	3.80	[85]	<i>Ar - C</i>	4.98	3.84	[88]
<i>Kr - Kr</i>	14.4	3.9	[85]	<i>Ni - C</i>	23.04	2.85	[117]
<i>Ne - Ar</i>	6.0	3.4	[85]	<i>Pt - C</i>	40.92	2.93	[117]

The interaction between the atomic cluster and graphite surface can be modeled with the Lennard-Jones potential, in case if they interact via the weak van der Waals force. In Tab. A.1 parameters ϵ and r_{min} corresponding to the van der Waals interactions between different atomic pairs are presented, the references, which are noted in the table, correspond to original works, where parameters were defined or used.

The Morse potential is a simple model pair potential that has parameters β and n which determine the width of the potential well and allows a wide variety of materials to be modeled. Morse potential is used to model interaction between metal cluster and graphite surface. In Tab. A.2 parameters of Morse potential for the different atomic pairs are shown.

Table A.2: Parameters of the Morse potential for different atomic pairs.

atomic pair	ϵ (eV)	r_0 (Å)	β (Å ⁻¹)	n	Ref.
<i>Ag</i> – <i>C</i>	0.29	2.35	2.66	3.46	[90]
<i>Ni</i> – <i>C</i>	2.43	1.74	1.87	2	[99]

A.2 Many-body potentials

Interaction between metal atoms are usually modeled via the many-body Sutton-Chen potential. In Tab. A.3 parameters for several metallic atoms are listed.

Table A.3: Parameters of the Sutton-Chen potential for different metals

atom	n	m	ϵ (eV)	c	a (Å)	Ref.
Ni	9	6	0.015707	39.432	3.52	[50]
Ag ^(bulk)	12	6	0.002542	144.410	4.09	[50]
Ag ^(finite)	12	6	0.000188	144.360	4.04	[51]
Pt	10	8	0.019833	34.408	3.92	[50]

Interaction between carbon atoms can be subdivided in two parts: short-range and long-range interactions. The short-range interactions are usually modeled via Brenner or Tersoff potentials. Table A.4 lists two sets of parameters introduced in Ref. [53]. The long-range interactions arising between carbon atoms consist of

Table A.4: *Two sets of parameters for the short-range carbon-carbon interaction modeled via Brenner potential. The parameters were taken from Refs. [53].*

parameter	value	parameter	value
D_e (eV)	6.325 (6.000)	a_0	0.01130400 (0.00020813)
β (\AA^{-1})	1.5 (2.1)	d_0	2.5 (3.5)
R_0 (\AA)	1.315 (1.390)	c_0	19 (330)
R_1 (\AA)	1.7 (1.7)	S	1.29 (1.22)
R_2 (\AA)	2.0 (2.0)	δ	0.80469 (0.5000)

Coulomb interactions (if the carbon atoms have partial charges) and van der Waals interactions. The later are usually described via Lennard-Jones and are dependent on the chemical surrounding of the interacting atoms.

Appendix B

Implementation of the kinetic model in MBN Explorer

Implementation of the kinetic model in `MBN Explorer` is based on the modified version of the conventional kMC method. Consider a molecular system constituting of a number of particles. For each particle in the system the number of possible diffusion directions to be defined. Thereby, a particle can either diffuse freely, or diffuse along the periphery of the already pre-formed structure as illustrated in Fig. 4.1. A diffusion direction for a particle is chosen randomly in such a manner that all possible diffusion directions are equally probable. For the given diffusion direction the probability for particle diffusion is then calculated from the predefined physical parameters input into the system, and the particle is translated with calculated probability in the direction defined earlier.

The procedures are repeated at each simulation step of the random walk dynamics algorithm. The schematic representation of the algorithm is illustrated in Fig. 4.2 and discussed in greater details in section 4.2.

To simplify the calculations, the random walk motion of particles is simulated on a lattice (grid). A lattice in the simulation represents an artificial subdivision of the entire simulation space into individual unit cells which can accommodate particles in the system. A particle on the lattice can occupy only a single unit cell and can move from the occupied cell only to the non-occupied neighboring cell (see Fig. 4.1). The number of possible diffusion directions of a particle depends on the packing of the lattice and on the number of occupied neighbor cells. `MBN Explorer` includes the cubic and the hexagonal types of the lattice packing which are described in sections B.1 and B.2 in greater details. The packing of particles on the lattice with

the hexagonal packing of the unit cells in 2D is illustrated in Fig. 4.1.

The random walk task in **MBN Explorer** allows to model structure formation by randomly adding particles into the system. The probability of adding a new particle into the system is manipulated by the keywords: **Appearance_Probability** and **Particle_Add_Step**. The keyword **Appearance_Probability** determines the maximal number of particles which can be added into the system at every step of the simulation. The integer part of the specified value is equal to the number of particles which is added at one step of the simulation. The fractional part of the specified value defines the probability to add an additional particle. The keyword **Particle_Add_Step** defines the intervals (in simulation steps) between the steps at which new particles are added into the system. Every new particle added to the system is placed to a randomly chosen non-occupied lattice cell.

The random walk dynamics algorithm is implemented in **MBN Explorer** for several extensions, which allow to simulate problems of varied degrees of complexity. Thus, the parameter **Surface** introduces a surface into the system and instructs the program to add new particles in the vicinity of this surface. New particles are added into a cell on the surface. If the cell where a particle is added appears to be empty, the particle is allowed to move on the surface, otherwise, if the cell appears occupied, the particle is shifted on the next level in the simulation lattice, thereby increasing the thickness of the emerging structure on a surface. The algorithm which is currently implemented in **MBN Explorer** assumes the surface to be located at the lower border of the simulation box. The details of the random walk dynamics on a surface are discussed in Sec. B.3.

Another feature of **MBN Explorer** is the possibility to control the dynamics of particles belonging to the agglomerated structures in the system. The keyword **Internal_Dynamic** specified in the task file instructs the program to either allow or prohibit the particles in the agglomerated structures to be immobile. If the internal dynamics of particles in agglomerated structures is not taken into account then only those particles which do not have any neighbors are allowed to move. If the parameter **Internal_Dynamic** is set to **on**, the probability of a particle random motion inside the agglomerated structures is calculated by using the kinetic equations, which are discussed in sections B.1 and B.2 in greater details.

Finally, **MBN Explorer** allows the user to specify the initial configuration of the system in the input file before new particles are added to the system.

B.1 Modeling of nanoparticle diffusion processes on a cubic lattice

In this section, the random motion of a particle on a cubic lattice is discussed. Cubic lattice is composed of equal cubic cells. Figure B.1 illustrates schematically the lattice with the cubic packing of the unit cells. The position of a particle on the lattice is defined by the coordinates of the cell which stores the particle. The coordinates of a cell in the lattice is given by a unique set of three integer indices (i, j, k) , which represent the the sequence number of the cell in the x-, y-, and z-directions, correspondingly. The numeration of the unit cells starts from the left lower corner of the simulation box. Note that in the general case the coordinates of the unit cell with the indices $(0, 0, 0)$ do not coincide with the origin of the laboratory coordinate frame. The size of the unit cell in the lattice is equal to the particle diameter and is defined by the user through the parameter **Cell_Size** in task file, see Fig. B.1a.

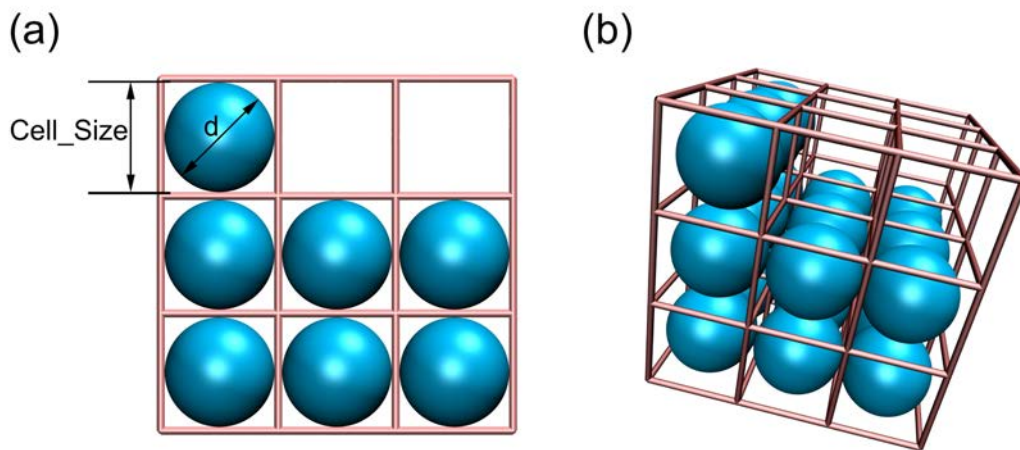


Figure B.1: Schematic representation of the cubic lattice, used for the simulation of particle motion with the cubic cell packing: (a) side view of the lattice; (b) perspective view of the lattice.

The position of a particle in space is given by the three coordinates (x, y, z) . These coordinates are related to the indices (i, j, k) of the unit cell which stores the particle through the following relations

$$x = \frac{d(2i+1)}{2} + \mathbf{Box_Center_X} - \mathbf{Box_Size_X}/2 \quad (\text{B.1})$$

$$y = \frac{d(2j+1)}{2} + \mathbf{Box_Center_Y} - \mathbf{Box_Size_Y}/2 \quad (\text{B.2})$$

$$z = \frac{d(2k+1)}{2} + \mathbf{Box_Center_Z} - \mathbf{Box_Size_Z}/2, \quad (\text{B.3})$$

where d is the particle diameter, defined by the parameter **Cell.Size**. The dimensions of the simulation box in the X, Y and Z directions are specified by the parameters **Box.Size.X**, **Box.Size.Y** and **Box.Size.Z**, respectively. **Box.Center.X**, **Box.Center.Y** and **Box.Center.Z** are the coordinates of the center of the simulation box. Equations (B.1)-(B.3) allow to obtain the indices of the cell (i, j, k) which stores a particle with the coordinates (x, y, z) as follows

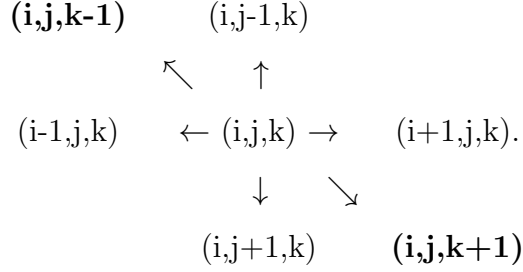
$$i = \frac{x + \mathbf{Box_Size_X}/2 - \mathbf{Box_Center_X}}{d} - \frac{1}{2} \quad (\text{B.4})$$

$$j = \frac{y + \mathbf{Box_Size_Y}/2 - \mathbf{Box_Center_Y}}{d} - \frac{1}{2} \quad (\text{B.5})$$

$$k = \frac{z + \mathbf{Box_Size_Z}/2 - \mathbf{Box_Center_Z}}{d} - \frac{1}{2}. \quad (\text{B.6})$$

Equations (B.4)-(B.6) are used by MBN Explorer to attribute a certain particle to a particular cell in the simulation lattice. These equations are especially important when the program reads the user-specified input configuration of a system from the input file.

The random walk dynamics algorithm implemented in the current version of MBN Explorer does not allow a particle on the lattice to move on a distance exceeding the particle's diameter. Therefore, a particle on the cubic lattice cannot "jump" to the diagonal neighboring cells or be translated over two or more cells during one simulation step (see Fig. B.1). For each particle in the lattice, the algorithm randomly picks a direction where it can be displaced. A particle on the cubic lattice in 3D can have up to six equivalent neighbor positions, while in 2D the number of neighbor positions is restricted to four. For a free particle (i.e. which is not surrounded by any other particles) occupying a cell with the indices (i, j, k) on the cubic lattice the list of the possible neighbor positions is



If a cell which stores a particle has one (or several) neighbor cell being occupied by other particles, than those occupied cells are defined as excluded, and are not taken into account during the random motion of the particle.

The probability of a particle diffusion in a certain direction is calculated with the use of the kinetic equation which is governed by the number of broken bonds due to the particle's displacement. Let us assume, that two particles on a cubic lattice as bound if they occupy two neighbor cells. Note that the cubic lattice imposes certain conditions on the motion of a particle along the periphery of any agglomerated structure which may form in the course of the simulation (see Fig. B.1). If a particle on the border of such an agglomerated island is bound with another (or with several) particle inside of the island, it does not preserve any of its bonds with the neighbor particles after it experiences a displacement. The detachment rate of a particle is then given by

$$\Gamma_e(l) = \nu \exp \left[-\frac{lE_b}{k_B T} - \frac{\Delta\mu}{k_B T} \right], \quad (\text{B.7})$$

where l is the number of bonds broken after particle detachment from the island, E_b is the binding energy of two particles, $\Delta\mu$ is the chemical potential of a particle detachment [2, 10, 102, 103], ν is the attempt escape rate of a particle from its equilibrium position, T is the temperature of the system and k_B is the Boltzmann constant. Note that Eq. (B.7) does not account for the bonds which may be created in the system when a particle diffuses. The feature of Eq. (B.7) is easy to understand. Indeed, in our model the particle diffusion process is considered stepwise, i.e., at each step of the computation a particle is displaced with the certain probability on the distance equal to its diameter in a random direction. But prior the particle is displaced to its new location there is no information about the newly created bonds in the system. Therefore only those bonds which the particle forms with neighbors prior the displacement influence the diffusion dynamics in the system.

A free particle (i.e. a particle without any neighbors) moves in a randomly chosen direction with a unit probability, i.e. its displacement rate is equal to one.

B.2 Modeling of nanoparticle diffusion processes on a hexagonal lattice

Another type of particle packing, considered in MBN Explorer, is the hexagonal type of packing. In this case the particle random dynamics is restricted to the hexagonal lattice. The simplified schematic representation of two sequential layers of the hexagonal lattice is shown in Figs. B.2-B.3. The indexes of the individual unit cells in the lattice are indicated. Figures B.2-B.3 show that a particle on the hexagonal lattice in 3D can have up to twelve equivalent neighbor positions, while in 2D this number is reduced to six.

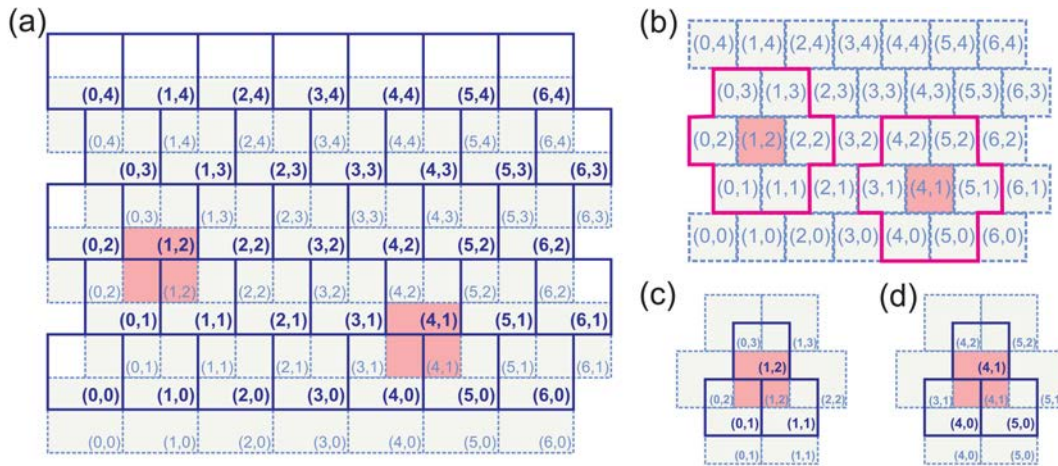


Figure B.2: The simplified schematic representation of a layer of cells in the hexagonal lattice. Plot (a) shows the general structure of the hexagonal lattice with an even z -index; (b) shows that a cell in the lattice has six equivalent neighbor cells within the same plane; (c) and (d) illustrate that a cell in the hexagonal lattice has three neighbor cells above and below itself.

The position of a particle on the hexagonal lattice is defined by the unique set of three integer indices (i, j, k) . The coordinates (x, y, z) of the particle in the laboratory coordinate frame are related to these indices. MBN Explorer numbers the unit cells sequentially, starting from the left lower corner of the simulation box. The coordinates of a particle on the hexagonal lattice are related to the coordinates of the unit cell as follows

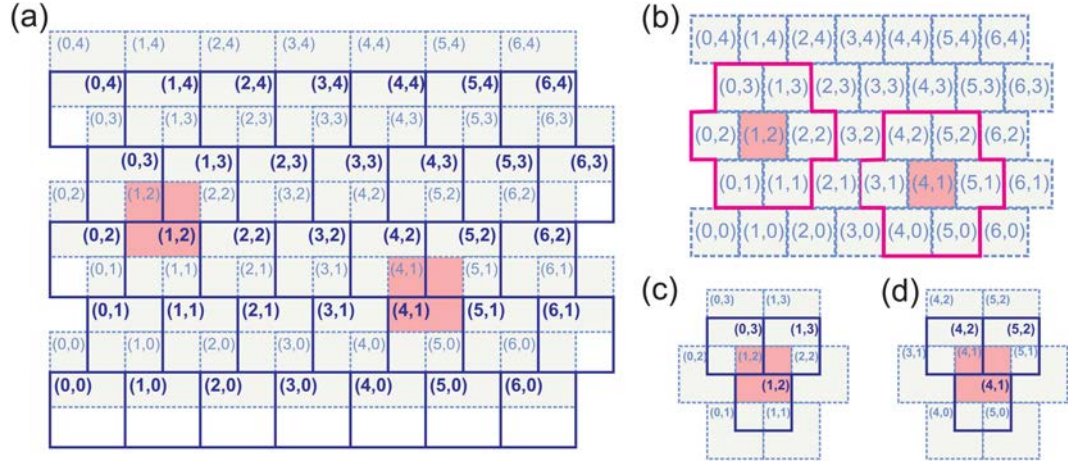


Figure B.3: Similar to Fig. B.2. The figure illustrates that the unit cells in the next layer in the hexagonal grid has the same number of neighbor cells as in the case of Fig. B.2. The figure shows the hexagonal lattice for the case of the odd z -index.

$$x = \begin{cases} d \left(i + \frac{1}{2} \right) + \text{Box_Center_X} - \frac{\text{Box_Size_X}}{2}, & j \in \text{even} \\ di + \text{Box_Center_X} - \frac{\text{Box_Size_X}}{2}, & j \in \text{odd} \end{cases} \quad (\text{B.8})$$

$$y = \begin{cases} d(jh_y + \Delta h_y) + \text{Box_Center_Y} - \frac{\text{Box_Size_Y}}{2}, & k \in \text{even} \\ djh_y + \text{Box_Center_Y} - \frac{\text{Box_Size_Y}}{2}, & k \in \text{odd} \end{cases} \quad (\text{B.9})$$

$$z = dkh_z + \text{Box_Center_Z} - \frac{\text{Box_Size_Z}}{2}. \quad (\text{B.10})$$

Here $h_z = 0.816497 d$ is the distance between two neighbor planes in the hexagonal lattice along the z -direction, $h_y = 0.866025 d$ is the distance between two rows of unit cells in the y -direction and $\Delta h_y = h_y/2$ is the shift of a row in the odd plane relative to the even plane in units of a particle diameter, see Fig. B.4.

Let us to define the list of possible neighbor positions for a particle with the indices (i, j, k) on the hexagonal lattice in the most general case of a three-dimensional lattice. The indices of the list of possible neighbor positions for the particle depend on the parity of the indices k and j . Figures B.2-B.3 show schematically the hexagonal grid for the even and odd planes respectively. Figure B.2b illustrates how the indices of the particle neighbor positions depend on the parity of the row index j , assuming the particle to be located in the plane with an even index k . Figure B.2c illustrate how the indices of the particle neighbor position change in the planes

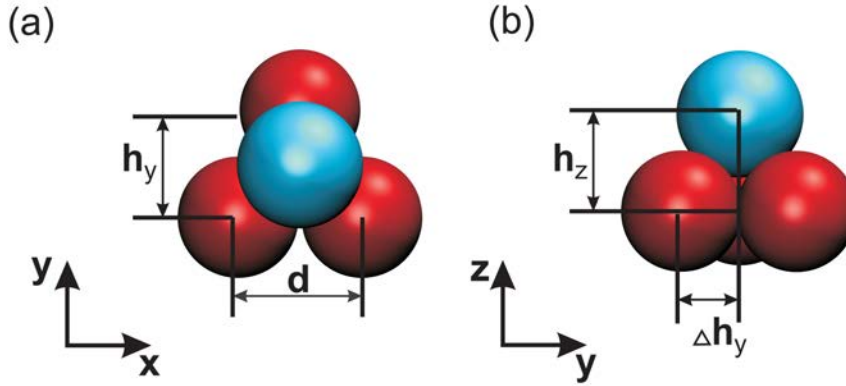


Figure B.4: The important lengths h_z , h_y and Δh_y used to define the spatial location of unit cells in the hexagonal lattice.

above and below the plane containing the particle. In this case the indices of the cells depend on the parity of the index j and the parity of the index k .

Figures B.3b-c illustrate the numbering scheme of the unit cells in the case of k being odd. Depending on the parity of the indices j and k one should distinguish between four different cases, which are summarized in the table below

$k - \text{even}$	$k - \text{even}$	$k - \text{odd}$	$k - \text{odd}$
$j - \text{even}$	$j - \text{odd}$	$j - \text{even}$	$j - \text{odd}$
$(i + 1, j, k)$	$(i + 1, j, k)$	$(i + 1, j, k)$	$(i + 1, j, k)$
$(i - 1, j, k)$	$(i - 1, j, k)$	$(i - 1, j, k)$	$(i - 1, j, k)$
$(i - 1, j + 1, k)$	$(i, j + 1, k)$	$(i - 1, j + 1, k)$	$(i + 1, j + 1, k)$
$(i, j + 1, k)$	$(i + 1, j + 1, k)$	$(i, j + 1, k)$	$(i, j + 1, k)$
$(i - 1, j - 1, k)$	$(i, j - 1, k)$	$(i - 1, j - 1, k)$	$(i, j - 1, k)$
$(i, j - 1, k)$	$(i + 1, j - 1, k)$	$(i, j - 1, k)$	$(i + 1, j - 1, k)$
$(i, j, k - 1)$	$(i, j, k - 1)$	$(i, j, k - 1)$	$(i, j + 1, k - 1)$
$(i, j - 1, k - 1)$	$(i, j - 1, k - 1)$	$(i, j, k + 1)$	$(i, j + 1, k + 1)$
$(i - 1, j - 1, k - 1)$	$(i + 1, j - 1, k - 1)$	$(i - 1, j + 1, k - 1)$	$(i + 1, j + 1, k - 1)$
$(i, j + 1, k + 1)$	$(i, j + 1, k + 1)$	$(i - 1, j + 1, k + 1)$	$(i + 1, j + 1, k + 1)$
$(i, j - 1, k + 1)$	$(i, j - 1, k + 1)$	$(i, j + 1, k - 1)$	$(i, j, k - 1)$
$(i - 1, j - 1, k + 1)$	$(i + 1, j - 1, k + 1)$	$(i, j + 1, k + 1)$	$(i, j, k + 1)$

The motion of particles on the hexagonal lattice in MBN Explorer is modeled similar

to the random walk dynamics of particles on the cubic lattice. However, in the case of the random dynamics on the hexagonal lattice, a particle can experience diffusion along the periphery of an agglomerated island, thereby maintaining some of its bonds with the neighbors. Therefore, in the case of a random walk dynamics on the hexagonal lattice one needs to distinguish between two possibilities: (i) a particle can diffuse along the periphery of an agglomerated island and maintain some of its bonds, or (ii) evaporation from an agglomerated island without keeping any bonds.

Thus, the probability of the particle evaporation (detachment) process is given by:

$$\Gamma_e(l) = \nu \exp \left[-\frac{lE_b}{k_B T} - \frac{\Delta\mu}{k_B T} \right], \quad (\text{B.11})$$

where l is the number of bonds broken after particle detachment from the island, E_b is the binding energy of two particles, $\Delta\mu$ is the chemical potential of particle detachment [2, 10, 102, 103], ν is the attempt escape rate of a particle from its equilibrium position, T is the temperature of the system and k_B is the Boltzmann constant.

The diffusion rate of a particle along the periphery of an agglomerated island reads as

$$\Gamma_d(n, m) = \nu \exp \left[-\frac{mE_b}{k_B T} - \frac{n\Delta\epsilon}{k_B T} \right], \quad (\text{B.12})$$

here m is the number of bonds that are broken due to particle motion, n is the number of maintained neighboring bonds between two particles and $\Delta\epsilon$ is the diffusion energy barrier.

B.3 Modeling of nanoparticle diffusion processes on a surface

The self-organization of nanoparticles plays an important role in the process of nanostructure formation on a surface. The understanding of the mechanisms of self-organization on the nanoscale is very important because this may provide essential tool for the control and manipulation of nanoparticle's dynamics on a surface. The random walk dynamics module in `MBN Explorer` allows the user to perform simulations of a nanostructure formation on a surface. Thus, the parameter **Surface** introduces a surface into the system and instructs the program to add new particles in the vicinity of this surface. New particles are added into a randomly chosen cell

on the surface. If the cell where a particle is to be added appears to be empty, the particle is allowed to move on the surface, otherwise, if the cell is occupied, the particle is shifted on the next level in the simulation lattice, thereby increasing the thickness of the emerging structure on a surface. The algorithm which is currently implemented in MBN Explorer assumes the surface to be located at the lower border of the simulation box (see Fig. B.5).

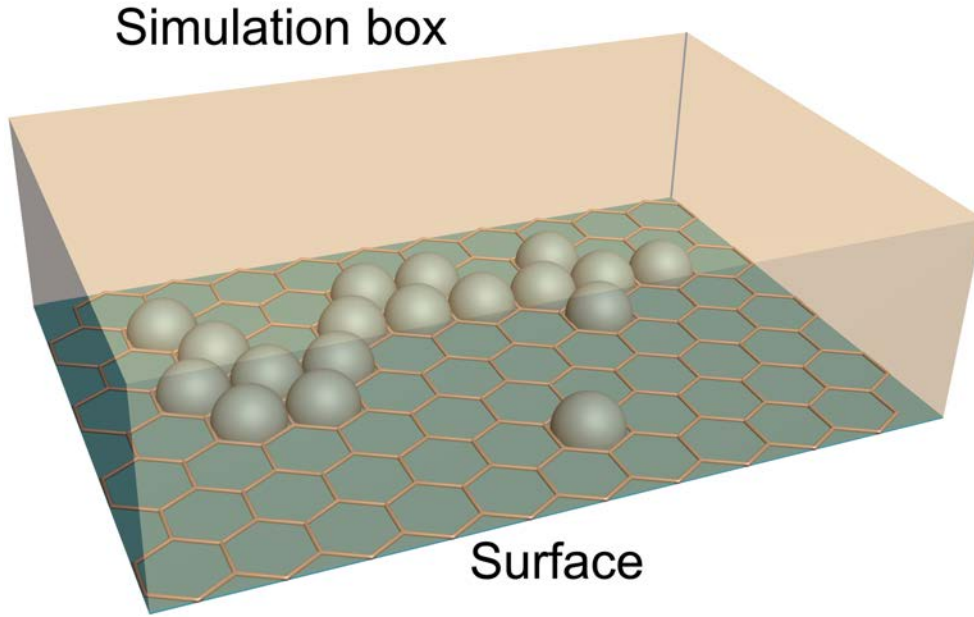


Figure B.5: Spatial organization of a fictitious surface inside the simulation box used in MBN Explorer.

A particle on the surface diffuses with the rate

$$\Gamma_{diff} = \nu \exp \left[-\frac{E_a}{k_B T} \right], \quad (\text{B.13})$$

where E_a is the activation energy, ν is the attempt escape rate, T is the temperature of the system and k_b is the Boltzmann constant.

If the particles in the system are simulated in 3D, they are allowed to leave the surface. The probability of particle evaporation from the surface in the present model depends on the binding energy between the surface and the particle and is defined as

$$\Gamma_{evap} = \nu \exp \left[-\frac{E_{sub}}{k_B T} \right], \quad (\text{B.14})$$

where E_{sub} is the binding energy between a particle and a surface. The process of particle diffusion on a surface, modeled on a lattice with the hexagonal packing of unit cells, is schematically illustrated in Fig. B.5 and Fig. 4.1. The relaxation of the agglomerated islands is driven by the diffusion of particles along the island periphery and particle detachment from the island. Both processes are schematically illustrated in Fig. 4.1. The diffusion rate of a particle along the periphery of an island can happen with or without particle's evaporation from the substrate. In the case if a particle does not leave the surface of a substrate due to the diffusion along the island's periphery the rate of particle hopping is given by

$$\Gamma_d^{surf}(m, n) = \nu \exp \left[-\frac{mE_b}{k_B T} - \frac{n\Delta\epsilon}{k_B T} - \frac{E_a}{k_B T} \right], \quad (\text{B.15})$$

where m is the number of bonds that are broken due to the particle motion, E_b is the binding energy of two particles, n is the number of maintained neighbor bonds between two particles and $\Delta\epsilon$ is the diffusion energy barrier, ν is the attempt escape rate. If a particle detaches from the substrate, but still diffuses along the periphery of the agglomerated structure the diffusion rate is defined as

$$\Gamma_d^{detach}(m, n) = \nu \exp \left[-\frac{mE_b}{k_B T} - \frac{n\Delta\epsilon}{k_B T} - \frac{E_{sub}}{k_B T} \right], \quad (\text{B.16})$$

where E_{sub} is the binding energy between a particle and the surface. The evaporation (detachment) rate of a particle from an island, without evaporating from the substrate is given by

$$\Gamma_e(l) = \nu \exp \left[-\frac{lE_b}{k_B T} - \frac{\Delta\mu}{k_B T} - \frac{E_a}{k_B T} \right], \quad (\text{B.17})$$

where l is the number of bonds broken after particle detachment from the island, $\Delta\mu$ is the chemical potential of particle detachment, ν is the attempt escape rate of a particle from its equilibrium position.

The detachment rate of a particle from an island and from the surface is defined as

$$\Gamma_{evap}(l) = \nu \exp \left[-\frac{lE_b}{k_B T} - \frac{\Delta\mu}{k_B T} - \frac{E_{sub}}{k_B T} \right], \quad (\text{B.18})$$

where E_{sub} is the binding energy between the particle and the substrate. In the algorithm implemented in MBN Explorer the interaction with the different types of surfaces can be modeled by varying the parameters E_a and E_{sub} parameters through

changing the value of the **Activation_Energy** and **Surface_Binding_Energy** keywords in the task file. Parameter E_a is related to the value of the diffusion constant D of a particle as

$$D = \frac{d_0^2 \nu_1}{2z} \exp \left[-\frac{E_a}{k_B T} \right]. \quad (\text{B.19})$$

Here d_0 is the diameter of the particle, and z is defined by the dimensionality of space [97, 98, 101]. In the case of particle diffusion on a surface $z = 2$, while in the 3D case $z = 3$.

Equations (B.13)-(B.18) are written in the most general case, and describe the dynamics of particles on a surface three dimensions. In a two-dimensional case a particle cannot detach from the surface and therefore the parameter E_{sub} in the task-file can be omitted. In the case of the simulation on a cubic lattice a particle can only evaporate from an island. Therefore, in this case, Eqs. (B.17)-(B.18) are used to calculate the rate of the particle evaporation.

B.4 Computation tests for the nanoparticle diffusion processes

The test examples of random walk dynamics are used to validate the correctness of the random walk algorithms implemented in MBN Explorer. The random walk dynamics module of MBN Explorer allows to model different types of self-organized structures such as fractals or compact islands in 2D or in 3D. The examples of random walk dynamics are focused on probing various physical properties of the system's behavior, which could be alternatively calculated analytically, because it is impossible to perform an exactly identical random walk dynamics simulations in alternative programs due to the stochastic nature of particle's trajectory.

One random walk step for the particles confined on a 2D cubic lattice

In this test 10000 identical particles are positioned on a 2D cubic lattice (see section B.1 for more information) which has the dimensions 303×303 cells. The particles are positioned so that the distance between two neighbor particles is equal to 2 empty cells in each direction. Therefore, at the first step of the random walk dynamics the motion of each particle is not affected by the interaction with other particles, i.e. the particles can be considered as moving statistically independent.

In this example after one step of the random walk dynamics each particle can shift with equal probability into positive or negative directions of the horizontal or vertical axes of the 2D lattice. The test example is terminated after the first step of the random walk dynamics and the number of particles displaced in each of the four possible directions is calculated.

Let us denote by ρ_r the fraction of particles that is moved to the right from their initial position during the first simulation step. Obviously, $\rho_r \rightarrow 0.25$ if the number of particles in the system is approaching infinity. However, for a limited but large number of particles in the system the values of ρ_r should be close to 0.25 with a certain probability. Let us assume that the distribution of ρ_r is Poisson. Then, for a given simulation result, the probability to obtain the value of ρ_r in the interval $(0.25 - 3\sigma \dots 0.25 + 3\sigma)$ is equal to 0.996, where σ is the so-called dispersion of the Poisson distribution. σ is a function of the number of particles in the system and can be calculated as:

$$\sigma = \frac{\sqrt{N\rho_r}}{N}, \quad (\text{B.20})$$

where N is the number of particles in the system (10^4 in the current test example). Substituting the number of particles N into Eq. (B.20) one obtains $\sigma = 0.005$. Therefore the 3σ -confidence interval for ρ_r is $0.235 \dots 0.265$. The completion of current test is considered to be successful if the fractions of particles moved in each of the four possible directions are within the 3σ -confidence interval.

One random walk step for the particles confined on a 3D cubic lattice

In this test example 10000 identical particles are positioned on a 3D cubic lattice (see section B.1 for more information) which has the dimensions $303 \times 303 \times 3$ cells. The particles are positioned so that the distance between two neighbor particles on the plane is equal to 2 empty cells in each direction (similar to the pervious test example). Therefore, in the course of the first step of the random walk dynamics the motion of each particle is not affected by the interaction with other particles, i.e. the particles can be considered as moving statistically independent.

After one step of the random walk dynamics each particle can shift with equal

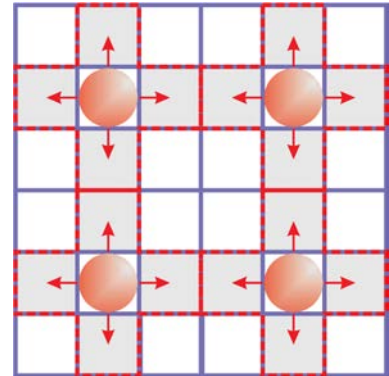


Figure B.6: Position of the particles on the cubic grid prior displacement.

probability into six directions, which correspond to the positive or negative directions of the axes of the 3D lattice. The current test example is terminated after first step of the random walk dynamics and the number of particles displaced in each of the six possible directions is calculated.

The dispersion σ of the Poisson distribution of the number of particles moved in a certain direction is evaluated using Eq. (B.20) with σ being equal to 0.004. Therefore, the 3σ -confidence interval for ρ_r is $0.154 \dots 0.179$, since $\rho_r \rightarrow 0.1667$ in the 3D case. The completion of current test example is considered to be successful if the fractions of particles moved in each of the six possible directions are within the 3σ -confidence interval.

One random walk step for the particles confined on a 2D hexagonal lattice

In this test example 10000 identical particles are positioned on a 2D hexagonal lattice (see section B.2 for more information) with has the dimensions 306×306 cells. The particles are positioned so that the distance between two neighbor particles on the plane is equal to 2 empty cells in each direction. Therefore, in the course of the first step of the random walk dynamics the motion of each particle is not affected by the interaction with other particles, i.e. the particles can be considered as statistically independent.

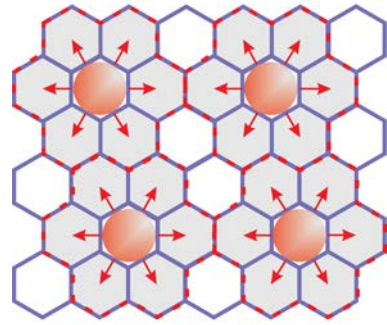


Figure B.7: *Position of the particles on the hexagonal grid prior displacement.*

After one step of the random walk dynamics each particle can shift with equal probability in one of the six possible directions, see section B.2. The current test example is terminated after first step of the random walk dynamics and the number of particles displaced in each of the six possible directions is calculated.

The dispersion σ of the Poisson distribution of the number of particles moved in a certain direction is evaluated using Eq. (B.20) and σ is equal to 0.004. Therefore, the 3σ -confidence interval for ρ_r is $0.154 \dots 0.179$. The completion of current test is considered to be successful if the fractions of particles moved in each of the six possible directions are within the 3σ -confidence interval.

One random walk step for the particles confined on a 3D hexagonal lattice

In this test example 10000 identical particles are positioned on a 3D hexagonal lattice (see section B.2 for more information) which has the dimensions $306 \times 306 \times 4$ cells. The particles are positioned so that the distance between two neighboring particles on the plane is equal to 2 empty cells. Therefore, in the course of the first step of the random walk dynamics the motion of each particle is not affected by the interaction with other particles, i.e. the particles can be considered as moving statistically independent.

After one step of the random walk dynamics each particle can shift with equal probability in one of the twelve possible directions, see section B.2. The current test example is terminated after the first step of the random walk dynamics and the number of particles displaced in each of the twelve possible directions is calculated.

The dispersion σ of the Poisson distribution of the number of particles moved in a certain direction is evaluated using Eq. (B.20) and σ in this example is equal to 0.0029. Therefore, the 3σ -confidence interval for ρ_r is $0.075 \dots 0.092$. The completion of the current test is considered to be successful if the fractions of particles moved in each of the twelve possible directions are within the foregoing 3σ -confidence interval.

Deposition of particles on the 2D cubic lattice

In this test example identical particles are sequentially, one by one, deposited on a 2D square lattice which has the dimensions 200×200 cells. After the deposition the particles are not allowed to move. The coordinates for deposited particles are determined randomly. Therefore, the deposited particles should uniformly cover the surface of the substrate. The position of the system's center of mass is calculated after the deposition of 4000 particles.

The position of the system's center of mass can be predicted with a certain accuracy to be located in the vicinity the geometrical center of the substrate. In the current test example the coordinate frame origin is located at the geometrical center of the

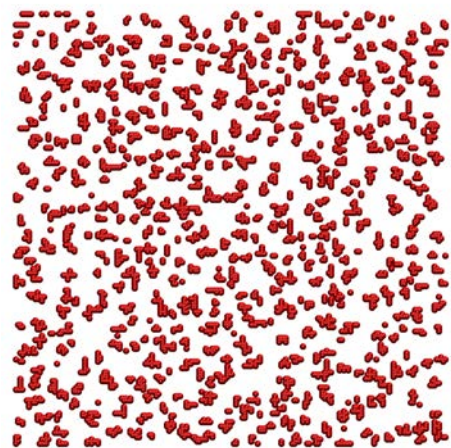


Figure B.8: Snapshot of the particles distribution on the cubic lattice.

substrate. Assuming the normal distribution of particles, the value of the dispersion of σ is calculated as follows:

$$\sigma = \sqrt{\frac{\sum_{i=0}^{N_d} (x_i - \mu)^2}{N_d}}, \quad (\text{B.21})$$

where $\mu = 0$ since the coordinate frame origin coincides with the geometrical center of the substrate, N_d is the width or the length of the substrate along the X and Y directions. $N_d = 200$ in the current test example, being the number of cells in X, and Y directions.

The so-called 3-sigma confidence interval δ for the system's center of mass position can be calculated as

$$\delta = \frac{3\sigma}{\sqrt{N}}, \quad (\text{B.22})$$

where N is the number of particles in the system (4000 in the current test example), and σ is the dispersion of the particle's distribution calculated using Eq. (B.21). Performing numerical evaluation of the expressions above one obtains the value $\delta = 2.75$. Therefore, with a probability of 99.2% the center of mass of 4000 randomly deposited particles should be located within a square of 5.5×5.5 cells around the geometrical center of the substrate. The current test is considered to be completed successfully if the system's center of mass is within the afore mentioned square around the coordinate frame origin.

One random walk step for the particles confined on a 2D hexagonal lattice with five unmovable neighbors

In the current test example 5625 identical moveable particles are positioned on a 2D hexagonal lattice (see section B.2 for more information) which has the dimensions 404×404 cells. Each moveable particle have 5 unmovable neighbors, see figure to the right.

Each particle interact with the particles located in the neighbor cells. In the present example the interaction energy (or the so-called binding energy) between two particles is equal to $1 k_B T$, where k_B and T are the Boltzmann constant and the absolute temperature, respectively. In the current test example the diffusion barrier energy is chosen to be equal to $0.2 k_B T$. Therefore, the probability of a

movable particle to change the position during one step of the random walk can be evaluated using Eq. (B.12) and is equal to 0.033.

The average number of particles that have changed their position after one step of the random walk dynamics simulation and the dispersion of this value can be calculated assuming the Poisson's statistics as follows:

$$\lambda = np \quad (\text{B.23})$$

$$\sigma = \sqrt{\lambda}, \quad (\text{B.24})$$

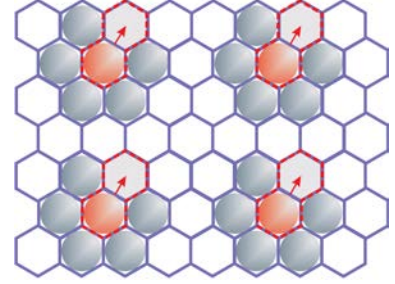


Figure B.9: A particle on the 2D hexagonal grid surrounded with five unmovable neighbor particles

where n is the total number of movable particles (5626 in the current test example) and $p = 0.033$ is the probability of a movable particle to change the position during one step of the random walk dynamics, λ is the expected value of the shifted particles and σ is the dispersion of λ .

Evaluating the expressions in the Eqs. (B.23)-(B.24) one obtains $\lambda = 185$ and $\sigma = 13.6$. Therefore the 3σ -confidence interval for the number of shifted particles (n_s) is [144...226]. The current test is considered to be accomplished successfully if the calculated value of the shifted particles is within the afore mentioned 3σ -confidence interval.

Aggregation of particles on a three-dimensional cubic lattice

This test example illustrate the aggregation of particles on the three-dimensional cubic lattice with the periodical boundary condition. New particles are added to the system with the predefined appearance probability.

A parameter which can be checked in this example is the number of particles at the end of the simulation (i.e. after 1000 simulation steps). The kinetic parameters E_b and $\Delta\mu$ are equal to $2.0 k_B T$. and $3.0 k_B T$ respectively, while the temperature equals to $T = 300 K$. In this test example new particles appear in the simulation box after every 20 simulation steps, with appearance probability equal to 2.5. Therefore the expectation number of particles N that were added into the system after 1000 simulation steps is calculated as

$$N = \left(\frac{n [p_a]}{n_{add}} + 1 \right) + \lambda \quad (\text{B.25})$$

$$\lambda = \left(\frac{n}{n_{add}} + 1 \right) (p_a - [p_a]), \quad (\text{B.26})$$

where n is the number of simulation steps, n_{add} is the periodicity of adding new particles into the system, p_a is the appearance probability of new particles in the system, $[p_a]$ is the integral part of p_a . λ in Eq. (B.25) is the expected value of the number of particles added to the system in the course of the entire simulation if the probability to add a particle on each step is equal to $p_a - [p_a]$. Evaluating the expressions in the Eqs. (B.23)-(B.24) one obtains $\sigma = 5.0$. Therefore the 3σ -confidence interval for the number of particles N is $[110 \dots 140]$. The current test is considered to be accomplished successfully if the calculated value of the number of particles at the end of simulation is within the afore mentioned 3σ interval.

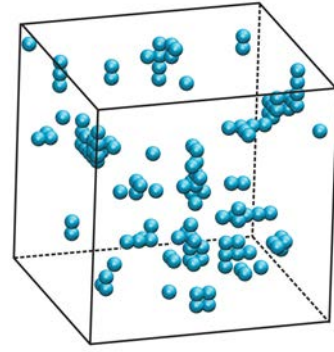


Figure B.10: Snapshot of the self-organized particles on a three-dimensional cubic lattice.

Aggregation of particles on a two-dimensional hexagonal lattice, compact islands formation

This test example illustrates the aggregation of particles on the two-dimensional hexagonal lattice with the periodical boundary condition. New particles are added to the system with the predefined particle appearance probability. At the end of the simulation compact islands are formed. The particles are moved with the rates which are calculated with the kinetic equations see section B.2. In this test example the kinetic parameters E_b , $\Delta\mu$ and $\Delta\mu$ are equal to $3.0 k_B T$, $0.1 k_B T$ and $10.0 k_B T$ respectively, while the temperature equals to $T = 300 K$.

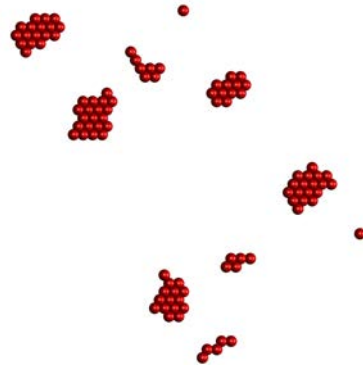


Figure B.11: Snapshot of the random walk dynamics simulation on the 2D hexagonal grid.

Aggregation of particles on a two-dimensional hexagonal lattice, fractal islands formation

This test example illustrates the aggregation of particles on the two-dimensional hexagonal lattice with the periodical boundary condition. New particles are added to the system with the predefined particle appearance probability. At the end of the simulation fractal islands are formed. The particles are moved with the rates which is calculated with the kinetic equations see section B.2. In this test example the kinetic parameters E_b , $\Delta\mu$ and $\Delta\mu$ are equal to $30 k_B T$, $15 k_B T$ and $100 k_B T$ respectively, while the temperature equals to $T = 300 K$.

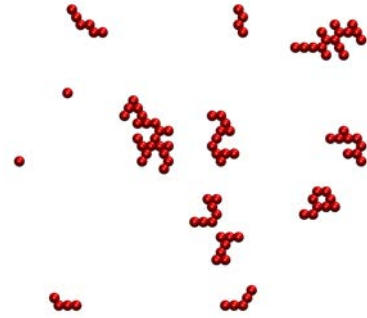


Figure B.12: Snapshot of the random walk dynamics simulation on the 2D hexagonal grid.

Acknowledgments

This dissertation would not have been possible without the guidance and the help of people who in one way or another supported me and extended their valuable assistance also for the preparation of this thesis.

First and foremost I am heartily thankful to my supervisor, Prof. Dr. Andrey V. Solov'yov, whose encouragement, guidance and support from the initial to the final stage enabled me to develop understanding of the subject. Working with him and in his group has been an enriching experience.

I thank the members of the MBN group for the advice and support: Dr. Alexander Yakubovich, Dr. Stephanie Lo, Dr. Emanuele Scifoni, Dr. Adilah Hussien, Dr. Andrei Korol, Dr. Ilia Solov'yov, Dr. Andriy Kostyuk, Pavel Nikolaev and Dr. Ekaterina Paramonova. My special gratitude goes to Dr. Ilia A. Solov'yov and Dr. Andrey Lyalin, in close collaboration with whom we did a substantial part of the present work.

While working on my dissertation, I profited a lot from the many opportunities to present and discuss my work-in-progress in various meetings at the Frankfurt Institute for Advanced Studies. I foremost thank Prof. Dr. h. c. mult. Walter Greiner for the uncounted enlightening talks we had during this time. The possibility to perform complex computer simulations at the Frankfurt Center for Scientific Computing is gratefully acknowledged.

I would also like to thank Mr. Hans-Christian Jankowiak and Mr. Alexander Dick for their help in the proofreading of this manuscript.

Most importantly, none of this would have been possible without the love and patience of my family. Especially I want to mention my parents Larisa and Valerij, my brothers Petr and Stas, my husband Alexander and my daughter Amelie. My family has been a constant source of love, concern, support and strength all these years.

Bibliography

- [1] Drexler, K. 1992. *Nanosystem*. Wiley, USA.
- [2] Bréchnignac, C., P. Houdy, and M. Lahmani, editors. 2007. *Nanomaterials and nanochemistry*. Cambridge University Press.
- [3] Meiwes-Broer, K., editor. 2000. *Metal cluster at surfaces: structure, quantum properties, physical chemistry*. Springer-Verlag, Berlin.
- [4] Rubahn, H.-G. 2004. *Basics of nanotechnology*. Weinheim, Denmark.
- [5] Solovyeva, V., K. Keller, and M. Huth. 2009. Organic charge transfer phase formation in thin films of the BEDT-TTF/TCNQ donoracceptor system. *Thin Solid Films*. 517:6671–6676.
- [6] Jensen, P. 1999. Growth of nanostructures by cluster deposition: experiments and simple model. *Rev. Mod. Phys.* 71:1695–1735.
- [7] Antzack, G. and G. Ehrlich, editors. 2010. *Surface diffusion: metals, metal atoms, and clusters*. Cambridge University Press, Cambridge.
- [8] III, W. G., D. Brenner, S. Lyshevski, and G. Iafrate, editors. 2007. *Handbook of Nanoscience: Engineering and Technology*. CRC Press.
- [9] Lando, A., N. Kébaïli, P. Cahuzac, A. Masson, and C. Bréchnignac. 2006. Coarsening and perling instabilities in silver nanofractals. *Phys. Rev. Lett.* 97:133402–(1–4).
- [10] Bréchnignac, C., P. Cahuzac, F. Carlier, C. Colliex, M. de Frutos, N. Kébaïli, J. L. Roux, A. Masson, and B. Yoon. 2003. Thermal and chemical nanofractal relaxation. *Eur. Phys. J. D.* 24:265–268.

-
- [11] Chen, Y., C. Li, H. Chen, and Y. Chen. 2006. One-dimensional nanomaterials synthesized using high-energy ball milling and annealing process. *Sc. and Tech. of Advan. Mater.* 7:839–846.
- [12] Fendler, J., editor. 1998. *Nanoparticles and nanostructured films*. Wiley-VCH, Germany.
- [13] Barabási, A.-L. and H. Stanley, editors. 1995. *Fractal concepts in surface growth*. Cambridge University Press, Cambridge.
- [14] Carlier, F., S. Benrezzak, P. Cahuzac, N. Kébaïli, A. Masson, A. K. Srivasta, C. Colliex, M. de Frutos, and C. Bréchnignac. 2006. Dynamics of polymorphic nanostructures: from growth to collapse. *Nanoletters.* 6:1875–1879.
- [15] Bardotti, L., P. Jensen, A. Hoareau, M. Treilleux, and B. Cabaud. 1995. Experimental observation of fast diffusion of large antimony clusters on graphine substrate. *Phys. Rev. Lett.* 74:4694–4697.
- [16] Scott, S. and S. Brown. 2006. Three-dimensional growth characteristics of antimony aggregates on graphite. *Eur. Phys. J. D.* 39:433–438.
- [17] Kébaïli, N., S. Benrezzak, P. Cahuzac, A. Masson, and C. Bréchnignac. 2009. Diffusion of silver nanoparticles on carbonaceous materials: cluster mobility as a probe for surface characterization. *Eur. Phys. J. D.* 52:115–118.
- [18] Schmidt, M., N. Kébaïli, A. Lando, S. Benrezzak, L. Baraton, P. Cahuzac, A. Masson, and C. Bréchnignac. 2008. Bend graphite surfaces as guides for cluster diffusion and anisotropic growth. *Phys. Rev. B.* 77:205420–(1–4).
- [19] Lando, A., N. Kébaïli, P. Cahuzac, C. Colliex, M. Couillard, A. Masson, M. Schmidt, and C. Bréchnignac. 2007. Chemically induced morphology change in cluster-based nanostructures. *Eur. Phys. J. D.* 43:151–154.
- [20] Whitesides, G. and B. Grzybowski. 2002. Self-assembly at all scales. *Science.* 295:2418–2421.
- [21] Bishop, K., C. Wilmer, S. Soh, and B. Grzybowski. 2009. Nanoscale forces and their uses in self-assembly. *Small.* 5:1600–1630.

-
- [22] Nykypanchuk, D., M. Maye, D. van der Lelie, and O. Gang. 2008. DNA-guided crystallization of colloidal nanoparticles. *Nature*. 451:549–552.
- [23] Park, S., A. Lytton-Jean, B. Lee, S. Weigand, G. Schatz, and C. A. Mirkin. 2008. DNA-programmable nanoparticle crystallization. *Nature*. 451:553–556.
- [24] Cui, Y. and C. Lieber. 2001. Functional nanoscale electronic devices assembled using silicon nanowire building blocks. *Science*. 291:851–853.
- [25] Shevchenko, E., D. Talapin, N. Kotov, S. O’Brien, and C. Murray. 2006. Structural diversity in binary nanoparticle superlattices. *Nature*. 439:55–59.
- [26] Hyde, G., S. M. Cullen, S. Jeon, S. Stewart, H. Jeon, E. Lobo, and G. Parsons. 2009. Atomic layer deposition and biocompatibility of titanium nitride nano-coatings on cellulose fiber substrates. *Biomed. Mater.* 4:025001–(1–10).
- [27] Demyashev, G., A. Taube, and E. Siores. 2002. Surface modification of titanium carbide with carbyne-containing nanocoatings. *J. Nanosc. Nanotechnol.* 2:133–137.
- [28] Bhattacharyya, S., T. Chini, D. Datta, R. Hippler, I. Shyjumon, and B. Smirnov. 2008. Processes involved in the formation of silver clusters on silicon surface. *J. Exp. Theor. Phys.* 107:1009–1021.
- [29] Böttcher, A., P. Weis, A. Bihlmeier, and M. Kappes. 2004. C₅8 on HOPG: soft-landing adsorption and thermal desorption. *Phys. Chem. Chem. Phys.* 6:5213–5217.
- [30] Conti, M., B. Meerson, and P. Sasorov. 1998. Breakdown of scale invariance in the phase ordering of fractal clusters. *Phys. Rev. Lett.* 80:4693–4696.
- [31] Sharon, E., M. Moore, W. McCormick, and H. Swinney. 2003. Coarsening of fractal viscous fingering patterns. *Phys. Rev. Lett.* 91:205504–(1–4).
- [32] Sempéré, R., D. Bourret, T. Woignier, J. Phalippou, and R. Jullien. 1993. Scaling approach to sintering of fractal matter. *Phys. Rev. Lett.* 71:3307–3310.
- [33] Li, W., X. Zheng, and W. Fei. 2009. Fractal growth of Fe-N thin film prepared by magnetron sputtering at elevated temperature. *Vacuum*. 83:949–952.

-
- [34] Jensen, P., A.-L. Barabási, H. Larralde, S. Havlin, and H. E. Stanley. 1994. Deposition, diffusion and aggregation of atoms on surfaces: a model for nanostructure growth. *Phys. Rev. B.* 50:15316–15329.
- [35] Liu, H. and P. Reinke. 2007. Gold cluster formation on c_{60} surfaces observed with scanning tunneling microscopy: Au-cluster beads and self-organized structures. *Surf. Sci.* 601:3149–3157.
- [36] Liu, H. and P. Reinke. 2006. C_{60} thin film growth on graphite: coexistence of spherical and fractal-dendritic islands. *J. Chem. Phys.* 124:164707–(1–5).
- [37] Böttcher, A., P. Weis, S.-S. Jester, D. Löffler, A. Bihlmeier, W. Klopper, and M. Kappes. 2005. Solid C_{58} films. *Phys. Chem. Chem. Phys.* 7:2816–2820.
- [38] Hwang, R., J. Schröder, C. Günther, and R. Behm. 1991. Fractal growth of two-dimensional islands: Au on Ru (0001). *Phys. Rev. Lett.* 67:3279–3282.
- [39] Hou, J., W. Xu, Y. Li, L. Yang, and Y. Wang. 1998. Metal-induced reconstruction of fullerene thin film: from dendritic to fractal growth. *J. Phys.: Cond. Mat.* 10:9609–9621.
- [40] Landau, L. and E. Lifshitz. 1981. *Quantum Mechanics*. Elsevier Butterworth-Heinemann.
- [41] Verlet, L. 1967. Computer experiments on classical fluids. *Phys. Rev.* 159:98103.
- [42] Levesque, D. and L. Verlet. 1993. Molecular-dynamics and time reversibility. *J. Stat. Phys.* 72:519–537.
- [43] Landau, L. and E. Lifshitz. 1980. *Statistical Physics*. Elsevier Butterworth-Heinemann.
- [44] Berendsen, H., J. Postma, W. van Gunsteren, A. Dinola, and J. Haak. 1984. Molecular dynamics with coupling to an external bath. *J. Chem. Phys.* 81:3684–3690.
- [45] Hoover, W. 1985. Canonical dynamics: equilibrium phase-space distributions. *Phys. Rev. A.* 31:1695–1697.

- [46] Nosé, S. 1984. A molecular dynamic method for simulations in the canonical ensemble. *Mol. Phys.* 53:255–268.
- [47] Hoover, W. 1999. *Time reversibility, computer simulation and chaos*. World Scientific, London.
- [48] Lennard-Jones, J. 1924. On the determination of molecular fields. *Proc. R. Soc. Lond. A.* 106:463–477.
- [49] Morse, P. 1929. Diatomic molecules according to the wave mechanics. II. vibrational levels. *Phys. Rev.* 34:57–64.
- [50] Sutton, A. and J. Chen. 1990. Long-range finnis-sinclair potentials. *Phil. Mag. Lett.* 64:139–146.
- [51] Yukna, J. and L. Wang. 2007. Molecular dynamics studies of the coalescence of silver cluster. *J. Phys. Chem. C.* 111:13337–13347.
- [52] Pawluk, T., L. Xiao, J. Yukna, and L. Wang. 2007. Impact of PES on textscMD results of the coalescence of M_2+M with $M = \text{Ir, Pt, Au, Ag}$. *J. Chem. Theory Comput.* 3:328–335.
- [53] Brenner, D. 1990. Empirical potential for hydrocarbons for use in simulating the chemical vapor deposition of diamond films. *Phys. Rev. B.* 42:9458–9478.
- [54] Leach, A., editor. 1996. *Molecular modeling: principles and applications*. Addison Wesley Longman Limited, Harlow.
- [55] Kébaïli, N. 2009. Fragmentation of silver fractal islands grown from cluster deposition on graphite substrate. Presentation on The Fourth International Symposium “Atomic Cluster Collisions: structure and dynamics from the nuclear to the biological scale” (ISACC 2009).
- [56] Rate, C. 2011. Free on-line dictionary of computing. www.FOLDOC.org.
- [57] Levi, A. and M. Kotrla. 1997. Theory and simulation of crystal growth. *J. Phys.: Condens. Matter.* 9:299–344.
- [58] Albano, E. 1996. The Monte Carlo simulation method: A powerful tool for the study of reaction processes. *Heter. Chem. Rev.* 3:389–418.

- [59] Voter, A. 2005. *Radiation Effects in Solids*, chapter Introduction to the kinetic Monte Carlo method. Springer, NATO Publishing Unit, Dordrecht, The Netherlands.
- [60] Meng, B. and W. Weinberg. 1996. Dynamical Monte Carlo studies of molecular beam epitaxial growth models: interfacial scaling and morphology. *Surf. Science*. 364:151–163.
- [61] Young, W. and E. Elcock. 1966. Monte Carlo studies of vacancy migration in binary ordered alloys: I. *Proc. Phys. Soc.* 89:735 – 746.
- [62] Pelaz, L., L. Marqués, M. Aboy, G. Gilmer, L. Bailón, and J. Barbolla. 2003. Monte Carlo modeling of amorphization resulting from ion implantation in Si. *Comp. Mat. Sci.* 27:1–5.
- [63] Yoon, B., V. Akulin, P. Cahuzac, F. Carlier, M. de Frutos, A. Masson, C. Mory, C. Colliex, and C. Bréchnignac. 1999. Morphology control of the supported islands grown from soft-landed clusters. *Surf. Science*. 443:76–88.
- [64] Ekardt, W., editor. 1999. *Metal clusters*. Wiley, New York.
- [65] Alonso, J., editor. 2005. *Structure and properties of atomic nanoclusters*. Imperial College Press, London.
- [66] Connerade, J.-P. and A. Solov'yov, editors. 2004. *Latest advances in atomic clusters collision: fission, fusion, electron, ion and photon impact*. Imperial College Press, World Scientific, London. ISBN 1-86094-495-7. Proceedings of Europhysics Conference International Symposium "Atomic Cluster Collisions: fission, fusion, electron, ion and photon impact" (ISACC 2003), St. Petersburg, July 18-21, 2003.
- [67] Haberland, H., editor. 1994. *Clusters of atoms and molecules, theory, experiment and clusters of atoms*. Springer Series in Chemical Physics, Berlin.
- [68] Gherghescu, R., D. Poenaru, A. Solov'yov, and W. Greiner. 2010. Hemispheroidal atomic clusters on planar surfaces. *Physica E*. 42:1555–1562.
- [69] Gherghescu, R., D. Poenaru, A. Solov'yov, and W. Greiner. 2009. Charged metallic clusters. *AIP Conf. Proc.* 1197:48–56.

- [70] Meng, X., S. Tang, and S. Vongehr. 2010. A review on diverse silver nanostructures. *J. Mater. Sci. Technol.* 26(6):487–522.
- [71] Lewis, L., P. Jensen, N. Combe, and J.-L. Barrat. 2000. Diffusion of gold nanoclusters on graphite. *Phys. Rev. B.* 61:16084–16090.
- [72] Rayleigh, J. 1879. On the capillary phenomena of jets. *Proc. of the London Math. Soc.* 10:4.
- [73] Gamov, G. 1928. Zur quantentheorie des atomkernes. *Z. Phys.* 51:204–208.
- [74] Bohr, A. and J. A. Wheeler. 1939. The mechanism of nuclear fission. *Phys. Rev.* 56:426450.
- [75] Solov'yov, I., A. Solov'yov, and W. Greiner. 2003. Fusion process of Lennard-Jones clusters: global minima and magic numbers formation. *Int. J. Mod. Phys. E.* 13:697–736.
- [76] Lyalin, A., O. Obolensky, A. Solov'yov, and W. Greiner. 2006. Fission of metal clusters. *Int. J. Mod. Phys. E.* 15:153–195.
- [77] Lyalin, A., S. Semenov, A. Solov'yov, N. Cherepkov, W. Greiner, and A. Solov'yov. 2000. Hartree-fock deformed jellium model for metallic clusters. *J. of Phys. B: Atom., Mol. and Opt. Phys.* 33:3653–3664.
- [78] Lyalin, A., S. Semenov, W. Greiner, and A. Solov'yov. 2002. Hartree-fock approach for metal-cluster fission. *Phys. Rev. A.* 65:023201–(1–5).
- [79] Wales, D. and J. Doey. 1997. Global optimization by Basin-Hopping and the lowest energy structures of Lennard-Jones clusters containing up to 110 atoms. *J. Phys. Chem. A.* 101:5111–5116.
- [80] Solov'yov, I., A. Solov'yov, W. Greiner, A. Koshelev, and A. Shutovich. 2003. Cluster growing process and a sequence of magic numbers. *Phys. Rev. Lett.* 90:053401–(1–4).
- [81] Fletcher, R., editor. 1987. *Practical Methods of Optimization.* John Wiley, New York.

- [82] Solov'yov, I., A. Solov'yov, and W. Greiner. 2006. *Chemical Physics: New Research*, chapter Cluster fusion algorithm: application to Lennard-Jones clusters. Nova Science Publishers. ISBN 1-60021-026-0, pages 89–127.
- [83] Obolensky, O., I. Solov'yov, A. Solov'yov, and W. Greiner. 2005. Fusion and fission of atomic clusters: recent advances. *Comp. Lett.* 1:313–318.
- [84] Obolensky, O., A. Lyalin, A. Solov'yov, and W. Greiner. Geometrical and statistical factors in fusion of small metal clusters.
- [85] Radzig, A. and B. Smirnov, editors. 1986. *Parameters of atoms and atomic ions*. Energoatomizdat, Moscow.
- [86] Bronshtein, I. and K. Semendyayev. 1997. *Handbook of Mathematics*. Springer, New York.
- [87] Strutinsky, V., N. Lyashchenko, and N. Popov. 1963. Symmetrical shapes of equilibrium for a liquid drop model. *Nucl. Phys.* 46:639–659.
- [88] Yamaguchi, Y. and J. Gspann. 2001. Large-scale molecular dynamics simulations of high energy cluster impact on diamond surface. *EPJ D.* 16:103–106.
- [89] Mons, M. and J. L. Calvé. 1990. Effect of the substituent on the potential energy surfaces and vibrational mode structure in the monosubstituted benzene-argon van der Waals complexes. *Chemical Physics.* 146:195–205.
- [90] Rafii-Tabar, H., H. Kamiyama, and M. Cross. 1997. Molecular dynamics simulation of adsorption of Ag particles on a graphite substrate. *Surf. Science.* 385:187–199.
- [91] Doye, J. and D. Wales. 1998. Global minima for the transition metal clusters described by Sutton-Chen potentials. *New J. Chem.*:733–744.
- [92] Deltour, P., J.-L. Barrat, and P. Jensen. 1997. Fast diffusion of a Lennard-Jones cluster on a crystalline surface. *Phys. Rev. Lett.* 78:4597–4600.
- [93] Khare, S., N. Bartelt, and T. Einstein. 1995. Diffusion of monolayer adatom and vacancy cluster: Langevin analysis and Monte Carlo simulations of their Brownian motion. *Phys. Rev. Lett.* 77:2148–2151.

-
- [94] Hamilton, J. 1991. Magic size effects for heteroepitaxial island diffusion. *Phys. Rev. Lett.* 77:885–888.
- [95] Wang, X., F. Xie, Q. Shi, and T. Zhao. 2004. Effect of atomic diagonal motion on cluster diffusion coefficient and its scaling behaviour. *Surf. Science.* 561:25–32.
- [96] Crank, J., editor. 1975. *The mathematics of diffusion.* Clarendon Press, Oxford.
- [97] Einstein, A. 1956. *Investigations on the theory of brownian movement.* Dover, New York.
- [98] Landau, L. and E. Lifshitz. 1987. *Fluid Mechanics.* Elsevier Butterworth-Heinemann.
- [99] Lyalin, A., A. Hussien, A. Solov'yov, and W. Greiner. 2009. Impurity effects on the melting of Ni clusters. *Phys. Rev. B.* 79:165403–(1–14).
- [100] Solov'yov, I., P. Nikolaev, A. Yakubovich, V. Dick, and A. Solov'yov. 2010. MBN explorer 1.0.0: A universal computer tool for simulating molecular and nanostructured materials. MBN Group @ FIAS.
- [101] Dick, V., I. Solov'yov, and A. Solov'yov. 2009. Theoretical study of fractal growth and stability on surface. *AIP Conf. Proc.* 1197:76–88.
- [102] Irisawa, T., M. Uwaha, and Y. Saito. 1995. Scaling laws in thermal relaxation of fractal aggregates. *Europhys. Lett.* 30:139–144.
- [103] Frenkel, J., editor. 1955. *Kinetic theory of liquids.* Dover.
- [104] Liu, H., Z. Lin, L. Zhigilei, and P. Reinke. 2008. Fractal structure in fullerene layers: simulation of growth process. *J. Phys. Chem. C.* 112:4687–4695.
- [105] Oura, K., V. Lifshits, A. Saranin, A. Zotov, and M. Katayama. 2003. *Surface science: an introduction.* Springer.
- [106] Job, G. and F. Herrmann. 2006. Chemical potential - a quantity in search of recognition. *Eur. J. Phys.* 27:353–371.

-
- [107] Wiberg, E. 1972. *Die chemische Affinität*. Verlag de Gruyter, Berlin, New York.
- [108] Stull, D. and H. Prophet. 1971. *JANAF Thermochemical Tables*. Natur. Bur. Stand (U.S.).
- [109] Witten Jr., T. and L. Sander. 1981. Diffusion-limited aggregation, a kinetic critical phenomenon. *Phys. Rev. Lett.* 47:1400–1403.
- [110] Dick, V., I. Solov'yov, and A. Solov'yov. 2010. Module of MBN explorer 1.0.0 software package for random walk dynamics simulations. MBN Group @ FIAS.
- [111] Hausdorff, F. 1919. Dimension und äußeres maß. *Math. Annal.* 79:157–179.
- [112] Martinez, F., M. Cabrerizo-Vilchez, and R. Hidalgo-Alvarez. 2001. An improved method to estimate the fractal dimension of physical fractals based on hausdorff definition. *Physica A.* 298:387–399.
- [113] Feder, J. 1988. *Fractals*. Plenum Press, New York.
- [114] Bréchnignac, C. 2010. Fragmentation dynamics of nanostructures. Presentation at The International Conference “Dynamics of Systems on the Nanoscale” (DySoN 2010).
- [115] Mashiah, A., O. Wolach, J. Sandbank, O. Uziel, P. Raanani, and M. Lahav. 2008. Lymphoma and leukemia cells possess fractal dimensions that correlated with their biological features. *Acta Haematol.* 119:142–150.
- [116] Baish, J. and R. Jain. 2000. Fractals and cancer. *Cancer Reasarch.* 60:3683–3688.
- [117] Ryu, J., H. Kim, D. Kim, D. Seo, and H. Lee. 2010. Immobilization of Au nanoclusters supported on graphite: Molecular dymanic simulations. *J. Phys. Chem. C.* 114:2022–20026.

Biography (Lebenslauf)

Veronika V. Dick (Semenikhina)

Frankfurt Institute for Advanced Studies

Johann Wolfgang Goethe-University

Ruth-Moufang-Str. 1

60438 Frankfurt am Main

Phone: +49 69 79847628

Fax: +49 69 79847611

Mobile: +49 151 54687440

semenikhina@fias.uni-frankfurt.de

Personal

Born on February 2, 1981

Székesfehérvár, Hungary

Married, one child



Education

1987-1998: School-1 with profound study of mathematics Sertolovo-1, Russia

1998-2002: Physical-Mechanical Department of St. Petersburg State Polytechnic University, Russia

2002-2004: Physical-Mechanical Department of St. Petersburg State Polytechnic University, Russia

2005-2007: PhD at the Frankfurt Institute for Advanced Studies

2007-2008: Child care

2008-2011: PhD at the Frankfurt Institute for Advanced Studies

Degrees and Academic Qualifications

1998 School-leaving certificate, Sertolovo-1, Russia

2002 Bachelor of Sciences in Physics, St. Petersburg State Polytechnic University, St. Petersburg, Russia

2004 Master of Sciences in Physics, St. Petersburg State Polytechnic University, St. Petersburg, Russia

Main research interests

Physics of Atoms, Molecules and Atomic Clusters

Nanoparticles deposition on a surface

Nanocoatings, biocompatible nanocoatings

GPU computing

List of Publications

Journal Publication

V.V. Semenikhina, V.K. Ivanov, C.V. Lapkin, Elastic scattering of an electron by the negative lithium ion, *Technical Physics*, **50**, No.3, 308, (2005), (Original Russian Text, published in *Zhurnal Technicheskoy Fiziki*, **75**, p. 24, (2005))

O.I. Obolensky, V.V. Semenikhina, A.V. Solov'yov, W. Greiner, Interplay of electrostatic and van der Waals forces in dimer of coronene, *International Journal of Quantum Chemistry*, **107**, p. 1335, (2007)

V.V. Semenikhina, A.G. Lyalin, A.V. Solov'yov, W. Greiner, Droplet Model of an Atomic Cluster at a Solid Surface, *Journal of Experimental and Theoretical Physics*, **106**, p. 678, (2008), (Original Russian Text, published in *Zhurnal Eksperimentalnoi i Teoreticheskoi Fiziki*, **133**, p. 781, (2008))

V.V. Dick, I.A. Solov'yov, A.V. Solov'yov, Fragmentation pathways of nanofractal structures on a surface, <http://arxiv.org/abs/1001.3992>, submitted to *Physical Review E*, (2011)

Conference Proceedings

V.V. Semenikhina, V.K. Ivanov, A.N. Ipatov, C.V. Lapkin, Elastic electron scattering on negative lithium ion, *Proc. SPIE*, **5127**, p. 41, (2003)

V.V. Semenikhina, V.K. Ivanov, C.V. Lapkin, Differential cross section of elastic electron scattering by negative lithium ion, *Proc. SPIE*, **5400**, p. 46, (2004)

V.V. Semenikhina, V.K. Ivanov, R.G. Polozkov, Elastic electron scattering by negative metallic cluster ion: Na_7^- , *Proc. SPIE*, **5831**, p. 26, (2005)

P. Berke, M.-P. Deplancke-Ogletree, A.G. Lyalin, V.V. Semenikhina, A.V. Solov'yov, Simulation of the nanoindentation procedure on pure nickel on the smallest length scale: a simple atomistic level model, in Latest Advances in Atomic Cluster Collisions, J.-P. Connerade and A. V. Solov'yov, eds., p. 205, Imperial College Press, London (2008)

V.V. Dick, I.A. Solov'yov, A.V. Solov'yov, Theoretical study of fractal growth and stability on surface, in Proc. 4th ISACC (Ann Arbor, USA, July 14-18, 2009), *AIP Conf. Proc.*, **1197**, p. 76, (2009)

I.A. Solov'yov, V.V. Dick, A.V. Solov'yov, Nanoparticles on a surface: atomistic approach for structure, dynamics and pattern formation, in Conf. Series XVIIth Symposium on Atomic, Cluster and Surface Physics 2010 (Oberurgl, Austria, January 24 - 29, 2010), p. 21, ISBN 978-3-902719-52-2, Innsbruck university press (2010)

V.V. Dick, I.A. Solov'yov, A.V. Solov'yov, Nanoparticles dynamics on a surface: fractal pattern formation and fragmentation, in Proc. of the International conference Dubna-Nano2010 (Dubna, Moscow Region, Russia, on July 5-10, 2010), *J.Phys.: Conf.Ser.*, **248**, p. 012025 (2010)

V.V. Dick, I.A. Solov'yov, A.V. Solov'yov, Theoretical study of nanofractal stability on the surface, in *Conf. Series XVIIth Symposium on Atomic, Cluster and Surface Physics 2010* (Oberurgl, Austria, January 24 - 29, 2010), p. 245, ISBN 978-3-902719-52-2, Innsbruck university press (2010)